Università degli Studi di Milano–Bicocca
Facoltà di Scienze Matematiche Fisiche e Naturali

Scuola di Dottorato di Scienze
Corso di Dottorato di Ricerca in Fisica ed Astronomia

Observability of heavy neutral Higgs bosons decaying into leptons at CMS. Contributions to the ECAL intercalibration and electron identification.

Coordinatore: Prof. Claudio Destri
Tutore: Prof. Marco Paganoni

Tesi di Dottorato di
Roberto Salerno
Matricola R00438

XIX Ciclo
Anno Accademico 2005–2006

Thèse présentée pour obtenir le grade de

DOCTEUR DE L'ECOLE POLYTECHNIQUE

Spécialité: Physique

par

Roberto Salerno

Observability of heavy neutral Higgs bosons decaying into leptons at CMS. Contributions to the ECAL intercalibration and electron identification.

Soutenue le 6 novembre 2006 devant le jury composé de:

A. Djouadi	Université Paris-Sud, Orsay	Rapporteur
U. Gasparini	Università di Padova, Padova	Rapporteur
C. Charlot	Ecole Polytechnique, Palaiseau	Directeur de thèse
M. Paganoni	Università di Milano-Bicocca, Milano	Directeur de thèse

Contents

Introduction

The field of particle physics is nearing a critical juncture: up to now the highly successful Standard Model (SM), whose predictions of various cross sections and precision observable are in excellent agreement with the data from the most advanced accelerators to date, has been sufficient to meet experimental demands. However there at least a one major glitch in this elegant picture: all particles in the Standard Model have zero mass. To rescue the theory from this absurd prediction, an entity called the Higgs field has been postulated, which breaks some of the symmetry and allows particles to have mass. This mechanism requires the existence of one or more Higgs boson, spinless particles with unknown mass. Their discovery is the prime goal of the future high energy experiments. Apart of the mass issue, there others problems with the Standard Model. A fundamental shortcoming is that all attempts to put in the fourth force, gravity, onto the SM have failed. Also, there is no particle candidate for the so-called dark matter, which according to the latest cosmological observations makes up most of the mass in the Universe.

For all these reasons, it is widely believed that there is still unexplored physics beyond the Standard Model. The most popular extension of the Standard Model that solves many of these issues, is the Minimal Supersymmetric Model (MSSM). In the MSSM, every Standard Model particle has a supersymmetric partner that differs from it by half a unit in spin. This leads to the introduction of *sleptons* and *squarks* as the superpartners of leptons and quarks, and *neutralinos* and *charginos* as superpartners of gauge and Higgs bosons. To postulate the R-parity conservation has the consequence that supersymmetric particles are only produced in pairs and that there exists a stable Lightest Supersymmetric Particle (LSP), which could act as the dark matter candidate. Contrary to the Standard Model, the Higgs sector now contains five physical Higgs bosons: two CP-even neutral scalars (h, H) one CP-odd neutral scalar (A) and a pair of charged Higgs boson ($H^{\pm}$). The unambiguous observation of these particles would clearly constitutes direct evidence of New Physics beyond the Standard Model. These particles should be within the energy range of the world's next

large particle accelerator, the Large Hadron Collider (LHC), which is being built at the European Organization for Nuclear Research (CERN) in Geneva. The first collisions are foreseen for 2007. Four experiments will take data at LHC: two general purpose ones (ATLAS and CMS), an experiment dedicated to heavy ions physics (ALICE) and a fourth one for the study of b-physics (LHCb).
For the MSSM Higgs searches at LHC a number of important signatures into SM particles are identified assuming that sparticles are too heavy to participate in the decay processes. The possibility that, on the contrary, sparticles could be light enough so that the Higgs decays to sparticles could be kinematically allowed has been recently investigated. Higgs bosons decaying into sparticles might therefore open possibilities to explore regions of the parameter space otherwise inaccessible via SM-like decays into ordinary particles. This is the case in particular in the difficult low and intermediate tanβ region of the MSSM parameter space. One of the most promising channels is the A/H decay into a pair of next-to-lightest neutralinos (χ_2^0) followed by the leptonic decay $\chi_2^0 \rightarrow l^+l^-\chi_1^0$ (with $l = e, \mu$). This process results in a clean four lepton plus missing transverse energy ($\not\!\!E_T$) final state signature:

$$A/H \rightarrow \chi_2^0\chi_2^0 \rightarrow 4l^{\pm} + \not\!\!E_T \ (l = e, \mu).$$

In this thesis the potentially of the CMS experiment is thoroughly investigated. The CMS has designed the largest ever built crystal electromagnetic calorimeter (ECAL), with the aim to reach an excellent intrinsic energy resolution. In order to fully profit of its performance a very accurately is needed. In particular a channel-to-channel relative calibration is necessary, referred to as intercalibration, requiring a detailed understanding of the single crystal energy response. Before the installation in CMS, the ECAL channels will be intercalibrated using electron beams in a test beam, cosmic rays and laboratory measurements, to have an initial set of coefficients at startup. Moreover, since the radiation damage affects the transparency of the crystals, the response of each channel will be constantly monitored with a monitoring system based on the injection of laser light. Part of this thesis is dedicated to the study of the ECAL intercalibration procedure.
Moreover, the analysis of the physics channel $A/H \rightarrow \chi_2^0\chi_2^0 \rightarrow 4l^{\pm} + \not\!\!E_T$ ($l = e, \mu$) includes low p_T isolated electrons to be measured and identified in challenging kinematics and background conditions. At low p_T in particular it is mandatory to have refined electron reconstruction methods to preserve the signal efficiency and reject the "fake" electron contamination from QCD jets. In this thesis a new strategy for the selection, isolation and identification of primary electrons

exploiting different electron measurement patterns is studied.

This thesis is organized in the following way. First, in chapter 1, the Minimal Supersymmetric Standard Model is introduced and a phenomenological overview of the MSSM Higgs sector is presented. A general overview of both LHC and the CMS detector, with a special emphasis to the electromagnetic calorimeter, is given in chapter 2. Chapter 3 and 4 are dedicated respectively to the study of the ECAL intercalibration and to the detailed analysis of the electron selection and identification in CMS. Finally, in chapter 5, the discovery reach of the neutral Higgs boson decaying into leptons is evaluated. The results contained in chapters 3, 4 and 5 represent my personal and original contributions to the CMS collaboration activities.

Chapter 1

The Higgs bosons in the Minimal Supersymmetric Model

In this chapter the Higgs sector in the Minimal Supersymmetric Model (MSSM) is introduced.
The principles of the supersymmetry and how it solves importants defects of the Standard Model are firstly described in Section 1.1. The MSSM is introduced in Section 1.2, with the emphasis put on its phenomenology. The MSSM Higgs boson sector is described in Section 1.3. Finally, the supersymmetry and the MSSM Higgs bosons searches and limits from Tevatron and LEP experiments are discussed in Section 1.4.

1.1 Principles of supersymmetry

The field of particle physics is nearing a critical juncture: up to now the highly successful Standard Model (SM) [1], whose predictions of various cross sections and precision observable are in excellent agreement with the data from the most advanced accelerators to date, has been sufficient to meet experimental demands [2].
Hovewer the SM encounters several theoretical problems, which cannot be solved without the introduction of New Physics.

- The couplings of the three gauge interactions do not unify at some energy scale [3], so that SM cannot easily be included in a Grand Unified Theory (GUT).

- The hierarchy problem [4], i.e. the difference in mass scales between the mass scale at which the electroweak forces are unified (EW scale) and the mass scale where the quantum gravity becomes important (Plank scale). More technically, the question is why the Higgs boson is so much lighter than the Planck mass.

- Many astrophysical observations point towards the existence of non-relativistic, neutral non-baryonic dark matter [5]. Since neutrinos are not massive enough to explain this observation, a new candidate for this Cold Dark Matter (CDM) is needed.

- The gravitational interaction is not included in the Standard Model, so the theory is incomplete. A worse problem is that a unification of spin-1 gauge fields and spin-2 gravitational field within a unique algebra has been proven to be theoretically impossible, with very few exceptions to this theorem [6].

Supersymmetry (SUSY) is one of the best motivated candidate for the physics beyond the SM. It is a symmetry which connects fermions (matter particles) and bosons (force carriers) with each others. The SUSY operator Q generates these transformations:

$$Q|boson\rangle = |fermion\rangle \qquad Q|fermion\rangle = |boson\rangle \tag{1.1}$$

In the following it will be recalled how SUSY solves the drawbacks of the Standard Model listed before.

Unification of the gauge couplings

Since SUSY doubles the particle content of the Standard Model, the slope of the evolution of the gauge couplings will be alterated. A perfect unification of the gauge couplings can be obtained if the supersymmetric particles have masses of the order of 1 TeV/c^2. This is shown in Figure 1.1. In this plot, the supersymmetric particles are assumed to be effectively contributing to the running of the couplings constants only for energies above the typical SUSY mass scale, which causes the change in the slope of the coupling constants near 1 TeV. Imposing the unification, a fit yields the value for the break point M_{SUSY} and the unification point M_{GUT} [7]:

$$M_{SUSY} = 10^{3.4\pm0.9\pm0.4}\ \text{GeV/c}^2\ , \tag{1.2}$$

$$M_{GUT} = 10^{15.8\pm1.9\pm1.0}\ \text{GeV/c}^2\ . \tag{1.3}$$

The first error originates from the uncertainty in the coupling constants, the second one from the uncertainty in the mass splitting between the supersymmetric particles. The errors on M_{SUSY} show that the unification is not very sensitive to the exact value of the SUSY masses as a range of $100\ \mathrm{GeV/c^2} \leq M_{SUSY} \leq 10\ \mathrm{TeV/c^2}$ can be accommodated.

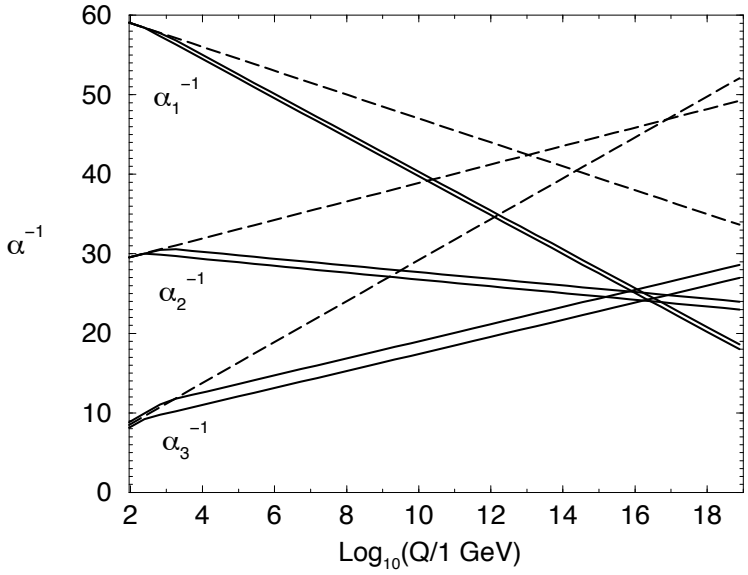

Figure 1.1: The renormalization group evolution of the inverse coupling constants $\alpha_i^{-1},\ i = 1,2,3$ of the three StandardModel groups U(1), SU(2) and SU(3) without supersymmetry, (dashed lines) and with supersymmetry, (solid lines). For the supersymmetric case the uncertainties are also shown. The calculations include two loops corrections [8].

The supersymmetic solution of the hierarchy problem

SUSY proposes a natural solution to the hierarchy problem, provided the masses of the superpartners are not too large. In a supersymmetric theory each of the Standard Model quark and lepton doublets resides in a chiral supermultiplet so it is accompanied by two complex scalars with couplings $|\lambda_B|^2 = |\lambda_F|^2$. Since bosonic and fermionic loops have opposite signs the quadratic divergences cancel and the residual one-loop correction of the Higgs mass squared is of the form:

$$\Delta m_H^2|_{tot} \simeq \frac{|\lambda_F|^2}{4\pi^2}\Big(\frac{3}{2}m_F^2 - m_B^2\Big)\ln(\lambda_{UV}/m_F)\ . \tag{1.4}$$

This means that the bare Higgs mass[1] must be of the order of m_H^2 and hence naturally small if the supersymmetric partner boson (B) and fermion (F) have similar masses:

$$|m_F^2 - m_B^2| \lesssim 1 \text{ TeV/c}^2 \tag{1.5}$$

This motivates the search for at relatively low energy [4].

Cold Dark Matter

All attempts to explain the nonrelativistic, neutral, nonbaryonic dark matter in the universe using Standard Model particles have failed. In the R-parity conserving SUSY[2] the Lightest Supersymmetric Particle (LSP) is always stable. This LSP is a good candidate for the cold matter in the Universe. There are strong constrains on the nature of such candidate: it must be electrically and color neutral, since otherwise it should have bound with the normal matter forming anomalously heavy isotopes that would have been detected.
The present lifetime of the Universe is about 10^{10} years, which implies an upper limit on the expansion rate and on the total relic abundance. The latest constraints on the dark matter from the WMAP experiment [9] lead to the band (at the 95% confidence level):

$$\Omega_m h^2 = 0.127^{+0.007}_{-0.013} \tag{1.6}$$

where Ω_m is the dark mass density in units of the critical density, and h is today's Hubble constant in units of 100 km/(s·Mpc) whose value is $h = 0.73^{+0.04}_{-0.03}$. There are a number of plausible supersymmetric dark matter candidates, but the most favored one is the neutralino (a supersymmetric particle that will be described in detail later). The attractive feature of the neutralino LSP is that has a relic density in accordance with (1.6) over a large domains of the SUSY parameter space [10].

Towards a theory of gravity

One of the main goal of the particle physics is to describe all the forces of the Nature, the three Standard Model interactions and the gravity, in a single theory. There is serious problem with this: it is impossible to unify spin-1 gauge fields and spin-2 graviton fields within a unique algebra. Considering a fundamental supersymmetric relation one realizes if the transformation is chosen to be local, i.e. in function of a space-time point, that an anticommutator of

[1] The physical Higgs mass squared is given by the bare Higgs mass squared plus the corrections from loop diagrams: $m_H^2 = (m_H^2)_0 + \Delta m_H^2$.

[2] The R parity is a symmetry which will be presented in the following section.

two general SUSY transformations is a local coordinate transformation [11]. A theory that is invariant under a general coordinate transformation is a General Relativity. Thus, making supersymmetry local, one obtains a theory of gravity called supergravity.

1.2 The Minimal Supersymmetric Standard Model

The Minimal Supersymmetric Standard Model (MSSM) is the most widely studied SUSY model. It owes is popularity mostly its simplicity, being essentially a straight-forward supersymmetrization of the SM. The MSSM requires a doubling of the SM degrees of freedom (d.o.f.). It contains three generations of chiral quark and lepton superfields, the vector superfields necessary to gauge the $SU(3)_C \times SU(2)_L \times U(1)_Y$ group of the Standard Model and two chiral $SU(2)$ doublet Higgs superfields. A summary of the Standard Model particles and their superpartners is given in the Tables 5.1, 5.2, and 5.3, together with their transformation properties under the Standard Model group.
Mixing of particle states appears in many parts of the supersymmetry spectrum. The phenomenologically most important mixing happen between the superpartners of the gauge and Higgs boson: after the electroweak symmetry breaking of $SU(2)_L \times U(1)_Y$ to $U(1)_{EM}$, the neutral $\widetilde{W}^0$ the bino $\widetilde{B}^0$, and the neutral higgsinos $\widetilde{H}_u^0$, $\widetilde{H}_d^0$ and the higgsinos $\widetilde{H}_u^+$, $\widetilde{H}_d^-$ have the same quantum numbers and therefore mix. The mass eigenstates of this system, which are the physically observable particles, are called *neutralinos* and note as χ_1^0, χ_2^0, χ_3^0 and χ_4^0. By convention the χ_1^0 is chosen to be the lightest of the four states. Similarly, the charged winos $\widetilde{W}^\pm$ and the higgsinos $\widetilde{H}_u^+$, $\widetilde{H}_d^-$ will mix to form four states $\chi_1^\pm$ and $\chi_2^\pm$ called *charginos*, again numbered from light to heavy.
Apart from the gauginos/higgsino mixing, also the two scalar partners of each heavy quark or lepton mix together, e.g. $\widetilde{t}_L$ and $\widetilde{t}_R$ mix and form the eigenstates $\widetilde{t}_1$ and $\widetilde{t}_2$.
In a supersymmetric theory is introduced a new discrete quantum number

$$R = (-1)^{3B+2S+L}, \tag{1.7}$$

where B is the baryon number, S is the spin and L is the lepton number. This quantity is called the R-Parity [12] and it distinguishes SM particle ($R = 1$) and the SUSY particle ($R = -1$).
If one assumes that R-Parity conservation is a fundamental property, this has therefore the following phenomenological consequences:

- sparticles are always produced in pairs, e.g. $pp \to \widetilde{g}\widetilde{q}$,

- heavier sparticles decay to lighter ones, eventually decaying into a state which contains an odd number of LSPs, e.g. $\widetilde{g} \to q\widetilde{q} \to qq^{'}\chi_1^0$.
- the Lighest Supersymmetric Particle (LSP) is stable because it has no legal decay modes.

The best candidate for a LSP, which could act as the dark matter candidate, is the lightest neutralino.

Names		spin 0	spin 1/2	$SU(3), SU(2)_L, U(1)_Y$
squarks, quarks	Q	$(\widetilde{u}_L \widetilde{d}_L)$	$(u_L d_L)$	$(\mathbf{3}, \mathbf{2}, \frac{1}{6})$
(×3 families)	u	$\widetilde{u}_R$	u_R	$(\mathbf{3}, \mathbf{1}, \frac{2}{3})$
	d	$\widetilde{d}_R$	d_R	$(\mathbf{3}, \mathbf{1}, -\frac{1}{3})$
sleptons, leptons	L	$(\widetilde{\nu}_L \widetilde{e}_L)$	$(\nu_L e_L)$	$(\mathbf{1}, \mathbf{2}, -\frac{1}{2})$
(×3 families)	e	$\widetilde{e}_R$	e_R	$(\mathbf{1}, \mathbf{1}, -1)$

Table 1.1: Fermions and their sfermion partners in the Minimal Supersymmetric Standard Model.

Names	spin 1/2	spin 1	$SU(3), SU(2)_L, U(1)_Y$
gluino, gluon	$\widetilde{g}$	g	$(\mathbf{8}, \mathbf{1}, 0)$
winos, W bosons	$\widetilde{W}^{\pm}\widetilde{W}^0$	$W^{\pm}W^0$	$(\mathbf{1}, \mathbf{3}, 0)$
bino, B boson	$\widetilde{B}^0$	B^0	$(\mathbf{1}, \mathbf{1}, 0)$

Table 1.2: Gauge bosons and their gaugino partners in the Minimal Supersymmetric Standard Model.

Names		spin 0	spin 1/2	$SU(3), SU(2)_L, U(1)_Y$
Higgs, higgsinos	H_u	$(H_u^+ H_u^0)$	$(\widetilde{H}_u^+ \widetilde{H}_u^0)$	$(\mathbf{1}, \mathbf{2}, \frac{1}{2})$
	H_d	$(H_d^0 H_d^-)$	$(\widetilde{H}_d^0 \widetilde{H}_d^-)$	$(\mathbf{1}, \mathbf{2}, -\frac{1}{2})$

Table 1.3: Higgs bosons and their Higgsino partners in the Minimal Supersymmetric Standard Model.

1.2.1 The neutralino/chargino phenomenology

In view of the following chapters, it is usefull to look closer at the mass spectrum and mixing of the neutralinos and charginos in the MSSM. In the gauge-

eigenstate basis $\psi^0 = (\widetilde{B}^0, \widetilde{W}^0, \widetilde{H}_d^0, \widetilde{H}_u^0)$, the neutralino mass term in the MSSM Lagrangian are

$$\mathscr{L} \subset -\frac{1}{2}(\psi^0)^T \mathbf{M}_{\chi^0} \psi^0 + c.c. \tag{1.8}$$

with

$$\mathbf{M}_{\chi^0} = \begin{pmatrix} M_1 & 0 & -c_\beta s_W m_Z & s_\beta s_W m_Z \\ 0 & M_2 & c_\beta c_W m_Z & -s_\beta c_W m_Z \\ -c_\beta s_W m_Z & c_\beta c_W m_Z & 0 & -\mu \\ -s_\beta s_W m_Z & -s_\beta c_W m_Z & -\mu & 0 \end{pmatrix}, \tag{1.9}$$

using the abbreviations $s_\beta = \sin\beta$,$c_\beta = \cos\beta$,$s_W = \sin\theta_W$ and $c_W = \cos\theta_W$ (θ_W is the Weinberg angle). The entries M_1 and M_2 in the matrix are the wino and the bino masses, while μ is the higgsino mass parameter. In general the parameters M_1, M_2 and μ have arbitrary and complex phases. The physical masses of the neutralinos are the absolute values of the eigenvalues of $\mathbf{M}_{\chi^0}$. The mass eigenstates can be given in closed form in terms of the parameters M_1, M_2, μ and $\tan\beta$. From the form of the matrix (1.9) one can note that if $m_Z \ll M_1, M_2, |\mu|$ the masses of χ_1^0 and χ_2^0 will be dominated by M_1 and M_2 respectively, while the masses of χ_3^0 and χ_4^0 will be of the order $|\mu|$.

In the broad class of minimal supergravity or gauge-mediated models satisfying gaugino unification conditions, M_1 and M_2 will have the same complex phase. In that case, a redefinition of the phases of $\widetilde{B}$ and $\widetilde{W}$ allows to make M_1 and M_2 both real and positive. The phase μ is then really a physical parameter which cannot be rotated away. However, if μ is not real, there can be disastrous CP-violating effects in low-energy physics, including no-zero electric dipole moments for both the electron and the neutron. Therefore, it is usually to assume that μ is real, its sign is still undetermined.

Often, one assumes that at the GUT scale the gaugino masses M_1, M_2 and M_3 are the same. Like in the case of gauge couplings, their low energy values can be derived using renormalization equations.

The chargino spectrum can be analyzed in a similar way. In the gauge-eigenstates basis $\psi^\pm = (\widetilde{W}^+, \widetilde{H}_u^+, \widetilde{W}^-, \widetilde{H}_d^-)$, the chargino mass terms in the Lagrangian are

$$\mathscr{L} \subset -\frac{1}{2}(\psi^\pm)^T \mathbf{M}_{\chi^\pm} \psi^\pm + c.c. \tag{1.10}$$

where, in 2×2 block form,

$$\mathbf{M}_{\chi^\pm} = \begin{pmatrix} \mathbf{0} & \mathbf{X}^T \\ \mathbf{X} & \mathbf{0} \end{pmatrix}; \qquad \mathbf{X} = \begin{pmatrix} M_2 & \sqrt{2} s_\beta m_W \\ \sqrt{2} c_\beta m_W & \mu \end{pmatrix}. \tag{1.11}$$

The mass eigenstates are related to the gauge eigenstates by two unitary 2×2 matrices. There are different mixing matrices for the positively charged states

and for the negatively charged states. Because these are only 2×2 matrices, it is not hard to solve for the masses explicitly:

$$m^2_{\chi_1^\pm}, m^2_{\chi_2^\pm} = \frac{1}{2}\Big[(|M_2|^2 + |\mu|^2 + 2m_W^2) \mp \sqrt{(|M_2|^2 + |\mu|^2 + 2m_W^2)^2 - 4|\mu M_2 - m_W^2 \text{sin}2\beta|^2}\Big]. \tag{1.12}$$

From the expression it is clear that if $m_W \ll M_2$, the mass of the $\chi_1^\pm$ is dominated by M_2 and the mass of $\chi_2^\pm$ is of order $|\mu|$ [13].

1.2.2 The slepton/squark phenomenology

Each flavor of charged lepton or quark has both left and right-handed components $f_{L,R}$. These components have separate scalar superpartners $\widetilde{f}_{L,R}$. The $\widetilde{f}_L$ and $\widetilde{f}_R$ have different weak isospin ($T = \frac{1}{2}$ and $T = 0$ respectively), but may mix as soon as the electroweak gauge symmetry is broken. Thus, the mass eigenstates of the squarks and the sleptons in the MSSM should be obtained from the diagonalizing mass matrices. The 2×2 mixing matrix $\mathbf{m}^2_{\widetilde{f}}$ takes the following general form:

$$\mathbf{m}^2_{\widetilde{f}} = \begin{pmatrix} m^2_{\widetilde{f}_{LL}} & m^2_{\widetilde{f}_{LR}} \\ m^2_{\widetilde{f}_{LR}} & m^2_{\widetilde{f}_{RR}} \end{pmatrix} . \tag{1.13}$$

The diagonal terms may be written in the form

$$m^2_{\widetilde{f}_{LL,RR}} = m_f^2 + m^2_{\widetilde{f}_{L,R}} + m^{D^2}_{\widetilde{f}_{L,R}} , \tag{1.14}$$

where $m_{\widetilde{f}}$ is the mass of the corresponding fermion, $m^2_{\widetilde{f}_{L,R}}$ is the soft supersymmetry breaking mass and $m^{D^2}_{\widetilde{f}_{L,R}}$ is a contribution due to the quadratic terms in the effective supersymmetric potential:

$$m^{D^2}_{\widetilde{f}_{L,R}} = m_Z^2 \cos 2\beta \, (I_3 + \text{sen}^2\theta_W \, Q_{em}) \tag{1.15}$$

where the term $\propto I_3$ is non-zero only for Finally, the off-diagonal mixing term takes the general for $\widetilde{f}_L$.

$$m^2_{\widetilde{f}_{LR}} = m_f\Big(A_f - \mu \begin{matrix} \tan\beta \\ \cot\beta \end{matrix}\Big) \qquad \text{for} \qquad f = \begin{matrix} e, \mu, \tau, d, s, b \\ u, c, t \end{matrix} \tag{1.16}$$

where the A_f are the coefficients of the Yukawa coupling matrix.
Assuming that the diagonal terms in (1.13) do not differ to much for $\widetilde{f}_L$ and $\widetilde{f}_R$, one can calculate that the mass splitting between the two mass eigenstates is approximately equal to twice the off-diagonal mixing term (1.16). This means that the sfermions mass spitting is proportional to the mass of the corresponding

fermion. For the first two generations of fermions, the mixing is therefore likely to be small and the mass eigenstates almost coincide with the gauge eigenstates. On the other hand, the mixing is large for the stop squarks, and it may also be important for the sbottom and the stau if tanβ is large [14].

1.2.3 SUSY breaking

Since no SUSY particle with the same mass as its SM partner has been discovered, SUSY must be spontaneously broken, i.e. the ultimate model should have a Lagrangian density which is invariant under supersymmetry, but a vacuum state which is not. It is assumed that spontaneous supersymmetry breaking takes place via interaction with some other fields which belong to the so called "hidden sector". The hidden sector interacts with the visible sector (containing the usual MSSM fields) by exchange of some messenger fields which mediate the SUSY breaking. This is adding terms to the Lagrangian which violate supersymmetry but become unimportant at high energies (so called "soft breaking terms" [15]). In the analogy with the electroweak symmetry breaking, spontaneous breaking of SUSY leads to a Goldstone particle which is a fermion in this case, called goldstino.
Different scenarios for SUSY breaking mechanism have been proposed. Phenomenologically viable models can thus be classified in terms of how SUSY breaking takes place and how it is transmitted to our observable sector. The two most popular models will be briefly discussed.

Gravity mediated supersymmetry breaking (SUGRA)

In this case the hidden and the visible sector interact each other via a gravitational interaction, supersymmetry must be a local symmetry, supergravity. In supergravity, the spin-2 graviton, has a superpartner, the spin-3/2 gravitino. Once supergravity is spontaneously broken, the gravitino absorbs the goldstino and becomes massive (the so called superhiggs mechanism). The gravitino mass is traditionally called $m_{3/2}$ and the soft terms should be roughly of the order

$$m_{3/2} \sim m_{soft} \sim \frac{\langle F \rangle}{m_P} \tag{1.17}$$

where $\langle F \rangle$ is the Vacuum Expectation Value (VEV) of the SUSY scalar potential and m_{soft} is the mass of the soft terms added to the Langrangian densiy; m_{soft} must vanish in the limit $\langle F \rangle \to 0$ where supersymmetry is unbroken, and in the limit $m_P \to \infty$ (corresponding to $G_{Newton} \to 0$). For m_{soft} of the order of a few hundred GeV, one would therefore expect that the scale associated

with the origin of the supersymmetry breaking should be roughly $\sqrt{\langle F \rangle} \sim 10^{10}$ or 10^{11} GeV. The gravitino is thus heavy, of the same order as m_{soft}, and its interactions are of gravitational strength, so extremely weak. It plays no role in the phenomenology.
To ensure tractable predictions the minimal Supergravity model (mSUGRA) is used, where the supergravity symmetry breaking is invoked and all the scalar and fermion masses are the same at the GUT scale. In mSUGRA scenario only four parameters and one sign, in addition to the SM parameters, need to be specified: the universal scalar m_0 and gaugino $m_{1/2}$ masses, the SUSY breaking universal trilinear coupling A_0, the ratio of the vacuum expectation values of the Higgs fields $\tan\beta$ and the sign of the higgsino mass parameter sign(μ).

Gauge mediated supersymmetry breaking (GMSB)

Another favored possibility is that the interactions which mediate the supersymmetry breaking are the electroweak and QCD gauge iteractions. In this gauge-mediated supersymmetry breaking scenario, the MSSM soft terms arise from loop diagrams involving some messengers particles. The messengers couple to a supersymmetry-breaking VEV $\langle F \rangle$, and also have $SU(3)_C \times SU(2)_L \times U(1)_Y$ interactions which provide a link to the MSSM. Using dimensional analysis, one can estimate for the MSSM soft terms

$$m_{soft} \sim \frac{\alpha_a}{4\pi} \frac{\langle F \rangle}{m_{mess}} \tag{1.18}$$

where the $\alpha_a/4\pi$ is a loop factor for the Feynman diagrams involving gauge interactions and m_{mess} is a characteristic scale of the masses of the messenger fields. So if m_{mess} and $\sqrt{\langle F \rangle}$ are roughly comparable, then the scale of supersymmetry breaking can be as low as about $\sqrt{\langle F \rangle} \sim 10^4$ or 10^5 GeV to give a value for m_{soft} of the right order of magnitude. According to (1.17) the gravitino mass is very small, of the order $m_{3/2} \sim 1$ eV. Thus, in the GSMB scenario, the gravitino is the LSP, to which all sparticles will ultimately decay.

Other supersymmetry breaking mechanisms have been proposed, such as anomaly mediated breaking, gaugino mediated breaking and superstring breaking. A discussion of these mechanisms is beyond the scope of this these. More details can be found in [16].

1.3 The MSSM Higgs sector

1.3.1 The tree level

As already mentioned in the previous section the supersymmetric structure of the theory requires (at least) two Higgs doublets to generate mass for both up-type and down-type quarks (and charged leptons). The two-doublet Higgs sector [17] contains eight scalar degrees of freedom: one complex Y = 1 doublet, $H_d = (H_d^0, H_d^-)$ and one complex Y = +1 doublet, $H_u = (H_u^0, H_u^+)$. The notation reflects the form of the MSSM Higgs sector coupling to fermions: $H_d(H_u)$ couples exclusively to down-type(up-type) fermion pairs. When the Higgs potential is minimized, the neutral components of the Higgs fields acquire vacuum expectation values:

$$\langle H_d \rangle = \frac{1}{\sqrt{2}} \begin{pmatrix} v_d \\ 0 \end{pmatrix}, \qquad \langle H_u \rangle = \frac{1}{\sqrt{2}} \begin{pmatrix} 0 \\ v_u \end{pmatrix} \tag{1.19}$$

where the normalization is chosen such that $v^2 = v_d^2 + v_u^2 = 4m_W^2/g^2$ =(246 GeV/c^2)^2. Spontaneous electroweak symmetry breaking results in three Goldstone bosons, which are absorbed and become the longitudinal components of the $W^\pm$ and Z. The remaining five physical Higgs particles consist of a charged Higgs pair

$$H^\pm = H_d^\pm \sin\beta + H_u^\pm \cos\beta \,, \tag{1.20}$$

one CP-odd scalar

$$A = \sqrt{2}\Big(\mathrm{Im}H_d^0 \sin\beta + \mathrm{Im}H_u^0 \cos\beta\Big) \,, \tag{1.21}$$

and two CP-even scalars

$$h = -\Big(\sqrt{2}\mathrm{Re}H_d^0 - v_d\Big)\sin\alpha + \Big(\sqrt{2}\mathrm{Re}H_u^0 - v_u\Big)\cos\alpha \,, \tag{1.22}$$

$$H = \Big(\sqrt{2}\mathrm{Re}H_d^0 - v_d\Big)\cos\alpha + \Big(\sqrt{2}\mathrm{Re}H_u^0 - v_u\Big)\sin\alpha \,, \tag{1.23}$$

with $m_h \leq m_H$. The angle α arises when the CP-even Higgs squared-mass matrix (in the $H_u^0 - H_d^0$ basis) is diagonalized to obtain the physical CP-even Higgs states.

The supersymmetric structure of the theory imposes constraints on the Higgs sector of the model. For example, the Higgs self-interactions are not independent parameters, they can be expressed in terms of the electroweak gauge coupling constants. As a result, all Higgs sector parameters at tree-level are determined by two free parameters: the ratio of the two neutral Higgs field vacuum expectation values,

$$\tan\beta \equiv \frac{v_u}{v_d} \,, \tag{1.24}$$

and one Higgs mass, conveniently chosen to be m_A.
In particular

$$m_{H^\pm}^2 \,=\, m_A^2 + m_W^2 \tag{1.25}$$

and the squared masses of the two CP-even Higgs bosons are

$$m_{H,h}^2 \,=\, \frac{1}{2}\Big(m_A^2 + m_Z^2 \pm \sqrt{(m_A^2+m_Z^2)^2 - 4m_Z^2 m_A^2 \cos^2 2\beta}\Big) \ . \tag{1.26}$$

An important consequence of eq. (1.26) is that, at tree level, there is an upper bound to the mass of the light CP-even Higgs boson. One finds that

$$m_h \leq m_Z |\cos 2\beta| \leq m_Z \ . \tag{1.27}$$

This is in marked contrast to the Standard Model, in which the theory does not constrain the value of m_h at tree-level. The origin of this difference is easy to ascertain. In the Standard Model, $m_{h_{SM}}^2 = \frac{1}{2}\lambda v^2$ is proportional to the Higgs self-coupling λ which is a free parameter. On the other hand, all Higgs self-coupling parameters of the MSSM are related to the squares of the electroweak gauge couplings.
Note that the Higgs mass inequality, eq. (1.27), is saturated in the limit of large m_A. In the limit of $m_A \gg m_Z$, the expressions for the Higgs masses and mixing angle simplify and one finds

$$\begin{aligned} m_h^2 &\simeq m_Z^2 \cos^2 2\beta \ , & (1.28)\\ m_H^2 &\simeq m_A^2 + m_Z^2 \sin^2 2\beta \ , & (1.29)\\ m_{H^\pm}^2 &= m_A^2 + m_W^2 \ , & (1.30)\\ \cos^2(\beta-\alpha) &\simeq \frac{m_Z^4 \sin^2 4\beta}{4m_A^4} \ . & (1.31) \end{aligned}$$

Two consequences are immediately apparent. First, $m_A \simeq m_H \simeq m_{H^\pm}$, up to the corrections of $\mathcal{O}(m_Z^2/m_A)$. Second, $\cos(\alpha-\beta) = 0$ up to the corrections of $\mathcal{O}(m_Z^2/m_A^2)$. This limit is known as the decoupling limit [18] because when m_A is large, there exists an effective low-energy theory below the scale of m_A in which the effective Higgs sector consists only of one CP-even Higgs boson, h. As we shall demonstrate below, the tree-level couplings of h are precisely those of the Standard Model Higgs boson when $\cos(\alpha-\beta) = 0$.
The phenomenology of the Higgs sector depends in detail on the various couplings of the Higgs bosons to gauge bosons, Higgs bosons and fermions. The couplings of the two CP-even Higgs bosons to W and Z pairs are given in terms of the angles α and β by

$$g_{hVV} \,=\, g_V m_V \sin(\beta-\alpha) \ , \qquad g_{HVV} \,=\, g_V m_V \cos(\beta-\alpha) \ , \tag{1.32}$$

where $g_V \equiv 2m_v/v$ for $V = Z$ or W. There are no tree-level couplings of A or $H^\pm$ to VV. The couplings of V to two neutral Higgs bosons (which must have opposite CP-quantum numbers) are given by $g_{\phi AZ}(p_\phi - p_A)$, where $\phi = h$ or H and the momenta p_ϕ and p_A point into the vertex, and

$$g_{hAZ} = \frac{g_Z \cos(\beta-\alpha)}{2\cos\theta_W} , \qquad g_{HAZ} = \frac{-g_Z \sin(\beta-\alpha)}{2\cos\theta_W} . \tag{1.33}$$

In the MSSM, the tree-level Higgs couplings to fermions obey the following property: H_d^0 couples exclusively to down-type fermion pairs and H_u^0 couples exclusively to up-type fermion pairs. Fermion masses are generated when the neutral Higgs components acquire vacuum expectation values. In particular, the couplings of the neutral Higgs bosons to $f\bar{f}$ relative to the Standard Model value, $gm_f/2m_W$, are given by

$$h b\bar{b} \ \ (\text{or } h\tau^+\tau^-) \ : \ -\frac{\sin\alpha}{\cos\beta} , \tag{1.34}$$

$$h t\bar{t} \ : \ \frac{\cos\alpha}{\sin\beta} , \tag{1.35}$$

$$H b\bar{b} \ \ (\text{or } H\tau^+\tau^-) \ : \ \frac{\cos\alpha}{\cos\beta} , \tag{1.36}$$

$$H t\bar{t} \ : \ \frac{\sin\alpha}{\sin\beta} , \tag{1.37}$$

$$A b\bar{b} \ \ (\text{or } A\tau^+\tau^-) \ : \ \gamma_5 \tan\beta , \tag{1.38}$$

$$A t\bar{t} \ : \ \gamma_5 \cot\beta , \tag{1.39}$$

(the γ_5 indicates a pseudoscalar coupling), and the charged Higgs boson couplings to fermion pairs, with all particles pointing into the vertex, are given by

$$g_{H^- t\bar{b}} = \frac{g}{\sqrt{2}m_W}\left[m_t \cot\beta \frac{1}{2}(1+\gamma_5) + m_b \tan\beta \frac{1}{2}(1-\gamma_5)\right] , \tag{1.40}$$

$$g_{H^-\tau^+\nu} = \frac{g}{\sqrt{2}m_W}\left[m_\tau \tan\beta \frac{1}{2}(1-\gamma_5)\right] . \tag{1.41}$$

In the limit of large $\tan\beta$ some of the Higgs couplings to down-type fermions can be significantly enhanced. It's useful to consider two large $\tan\beta$ regions.

- If $m_A \gg m_Z$, then the decoupling limit is reached, in which $|\cos(\beta-\alpha)| \ll 1$ and $m_H = m_A$. It follows that the $Hb\bar{b}$ and $Ab\bar{b}$ couplings have the same strength and they are significantly enhanced (by a factor of $\tan\beta$) relative to the $h_{SM}b\bar{b}$ coupling, whereas the HVV coupling is negligibly small. In contrast, the values of the hVV and $hb\bar{b}$ couplings are equal to the corresponding couplings of the Standard Model Higgs boson. In this case, it is conventional to refer to h as SM-like Higgs boson.

- If $m_A < m_Z$ and $\tan\beta \gg 1$, then $|\cos(\beta-\alpha)| \sim 1$ and $m_h = m_A$. In this case, the $hb\bar{b}$ and $Ab\bar{b}$ couplings have equal strength and are significantly enhanced (by a factor of $\tan\beta$) relative to the $h_{SM}b\bar{b}$ coupling, while the hVV is is negligibly small. It follows that the HVV coupling is equal in strength to the $h_{SM}VV$ coupling. In this case, it is conventional to refer to H as a SM-like Higgs boson.

There is a significant region of MSSM Higgs sector parameter space in which the decoupling limit applies, because $\cos(\beta-\alpha)$ approaches zero quite rapidly once m_A is larger than about 200 GeV/c^2. As a result, over a significant region of the MSSM parameter space, the search for the lightest CP-even Higgs boson of the MSSM is equivalent to the search for the Standard Model Higgs boson. This result remains valid, in many theories involving non-minimal Higgs sectors, in which there is a significant portion of the parameter space where the decoupling limit holds.

1.3.2 MSSM Higgs production

The production of the MSSM neutral Higgs bosons at a hadron collider proceeds essentially via the same processes as for the SM Higgs particle (see Figure 1.2), that is:

$$\text{associated } h/H \text{ production with } W/Z: \quad q\bar{q} \to V + h/H \tag{1.42}$$

$$\text{vector boson fusion for } h/H \text{ production:} \quad qq \to V^*V^* \to qq + h/H \tag{1.43}$$

$$\text{gluon-gluon fusion:} \quad gg \to h/H/A \tag{1.44}$$

$$\text{associated production with heavy quarks:} \quad gg, q\bar{q} \to Q\bar{Q} + h/H/A \tag{1.45}$$

The pseudoscalar Higgs boson A cannot be produced in association with gauge bosons or in the weak boson fusion processes at the tree-level, since direct A couplings to gauge bosons are forbidden in the MSSM by CP-invariance (see Section 1.3). Because of the different couplings of the Higgs particles to fermions and gauge bosons, the pattern for the production rates is significantly different from the SM case. Another major difference between the SM and MSSM cases is the presence of the additional SUSY particle spectrum. The sparticles, if they are relatively light, can substantially contribute to the processes which are mediated by loops such as the gluon-gluon mechanism, and to the radiative corrections in some other cases.

As in the case of Higgs branching ratios, the predicted cross-sections are sensitive to the MSSM Higgs parameters. Cross-sections for neutral MSSM Higgs production are shown in Figure 1.3, again, two representative values of $\tan\beta$ are

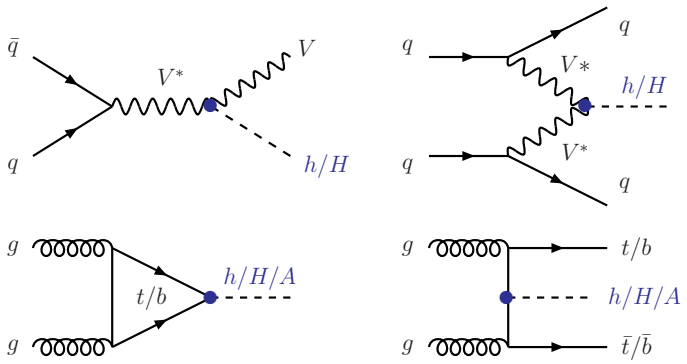

Figure 1.2: The dominant MSSM neutral Higgs production mechanisms in hadronic collisions.

considered: a low value of $\tan\beta = 3$ and a high value of $\tan\beta = 30$.
The dominant Higgs production mechanism over much of the MSSM parameter space is the gluon-gluon fusion, Higgs boson radiation off bottom quarks becomes important for large $\tan\beta$ in the MSSM, as the Higgs coupling to down type fermions is enhanced.
The dominant charged Higgs production process is the associated production with heavy quarks, $gg/q\bar{q} \to t\bar{b}H^-$ (and the charge conjugate final state). As to notice that if $m_{H^\pm} < m_t - m_b$, then $H^\pm$ is also produced in the decay of the top quark via $t \to b + H^+$ (and the charge conjugate final state). The second important production process is charged Higgs pair production in a Drell-Yan $q\bar{q}$ annihilation, which is mediated by s-channel photon and Z-boson exchange. Charged Higgs pairs can also be produced from gg initial states by the loop-mediated process. Finally, charged Higgs bosons can be produced in association with a W boson via $b\bar{b}$ annihilation and gg fusion.

1.3.3 MSSM Higgs decay modes

SM decay modes

Contrary to the SM case, where they are fully determined once the Higgs boson mass is fixed, the decay rates of the MSSM Higgs bosons depend to a large extent on their couplings to fermions and gauge bosons as well as their self couplings. In the region of parameter space where $m_A \gg m_Z$ and the masses of supersymmetric particles are large, the decoupling limit applies and the properties of h are indistinguishable from the SM Higgs boson. If supersymmetric particles are light, then the decoupling limit does not strictly apply even in the limit of $m_A \gg m_Z$. In particular, the h branching ratios are modified, if the decays of

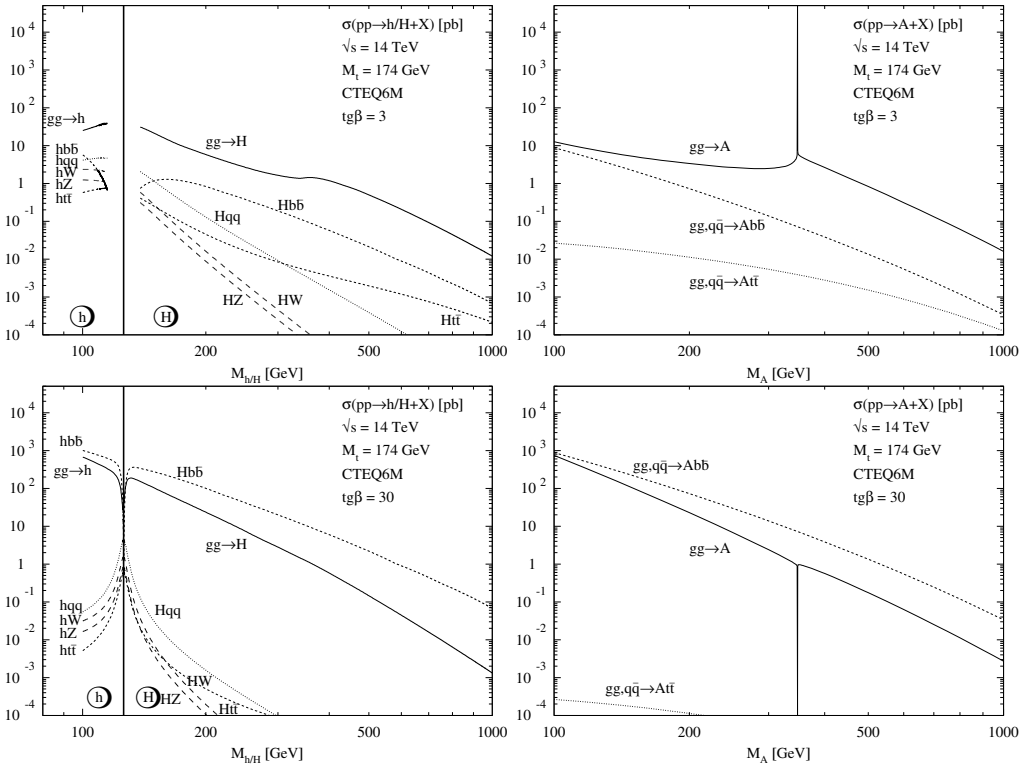

Figure 1.3: Neutral MSSM Higgs production cross sections at $\sqrt{s} = 14$ TeV for gluon-gluon fusion, vector boson fusion, associated production with W/Z and associated production with heavy quarks The four panels show the cross section in pb versus the Higgs mass. Left top: h, H production for tanβ=3. Right top: A production for tan$\beta = 3$. Left bottom: h, H production for tanβ = 30. Right bottom: A production for tan$\beta = 30$.

h into supersymmetric particles are kinematically allowed. In addition, if light superpartners exist that can couple to photons and/or gluons, then the one-loop gg and $\gamma\gamma$ decay rates would also deviate from the corresponding Standard Model Higgs decay rates due to the extra contribution of the light superpartners appearing in the loops. In both cases, the heavier Higgs states, H, A and $H^{\pm}$, are roughly mass degenerate, and their decay branching ratios depend crucially on tanβ as shown below.

In order to present the Higgs branching ratios, a set of MSSM parameters have to be choosen. The values of tanβ are fixed (for two representative choices) and of m_A is varied from its experimental lower bound of 90 GeV/c^2 up to 1 TeV/c^2. In addition, the gluino and MSSM squark mass parameters have been chosen to be $M_{SUSY} \equiv m_{\tilde{g}} = m_{\tilde{q}} = 1$ TeV/c^2, the squark mixing parameter $(A_f + \mu \text{cot}\beta) = 2.4 M_{SUSY}$, and the gaugino mass matrix parameters,

$\mu = M_2 \simeq 2M_1 = 1$ TeV/c^2. The motivation for choosing the gaugino mass parameters large is to avoid possible supersymmetric decay modes for the Higgs bosons for Higgs masses below 1 TeV/c^2.

The branching ratios for h and H as a function of their masses are shown in Figure 1.4. As m_A varies from 90 GeV/c^2 to 1 TeV/c^2, with the MSSM parameters as specified above, 135 GeV/c^2 $< m_H <$ 1 TeV/c^2 when tan$\beta = 3$ and 126 GeV/c^2 $< m_H <$ 1 TeV/c^2 when tan$\beta = 30$.

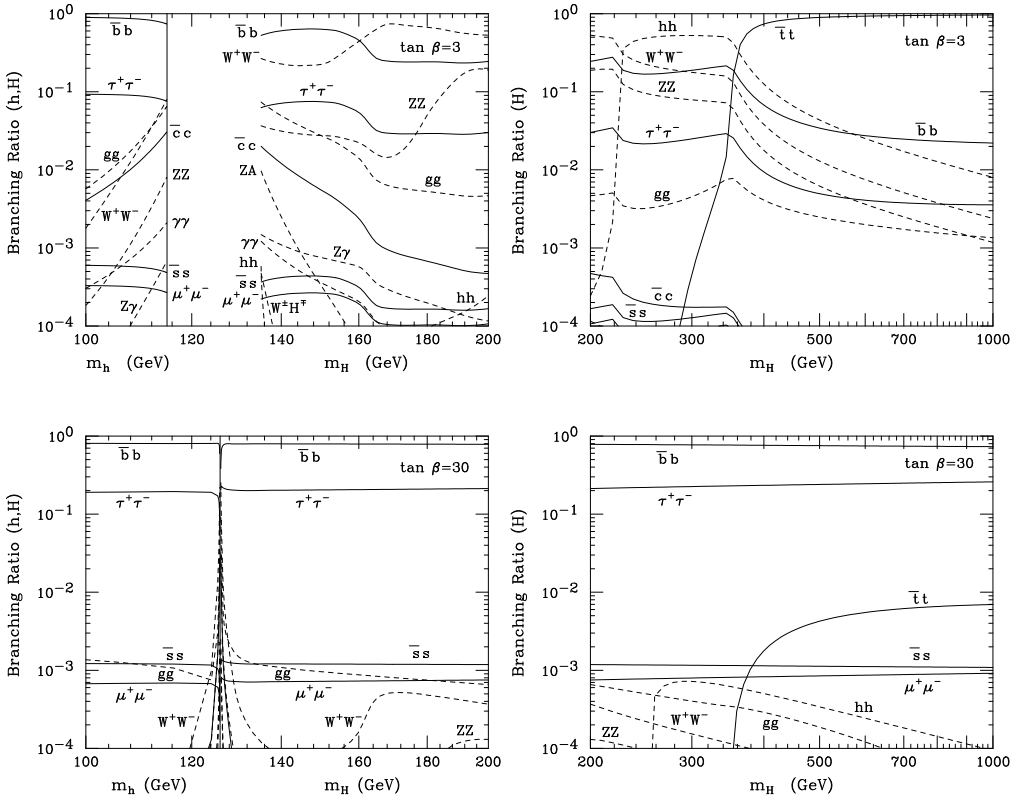

Figure 1.4: Branching ratios of the MSSM Higgs bosons h and H, with tanβ = 3 and 30, respectively. Final states labeled above include the possibility of one off-shell final state particle below the corresponding two-particle decay threshold. The above plots were made under the assumption that the average top and bottom squark masses are 1 TeV/c^2 and top-squark mixing is maximal. In this case, $m_h^{max} \simeq 115$ GeV/c^2 (125.9 GeV/c^2) for tan$\beta = 3$ (30), corresponding to the limit of large m_A, is indicated by the vertical line in the two left-side plots. The range of m_H shown corresponds to varying m_A between 90 GeV/c^2 and 1 TeV/c^2, while $m_h > 100$ GeV/c^2 corresponds to $m_A > 139$ GeV/c^2 (104 GeV/c^2) for tan$\beta = 3$ (30). Other supersymmetric parameters have been chosen such that there are no supersymmetric particle decay modes in the Higgs mass ranges shown above.

The branching ratios for A and $H^{\pm}$ as a function of their masses are shown in Figure 1.5.

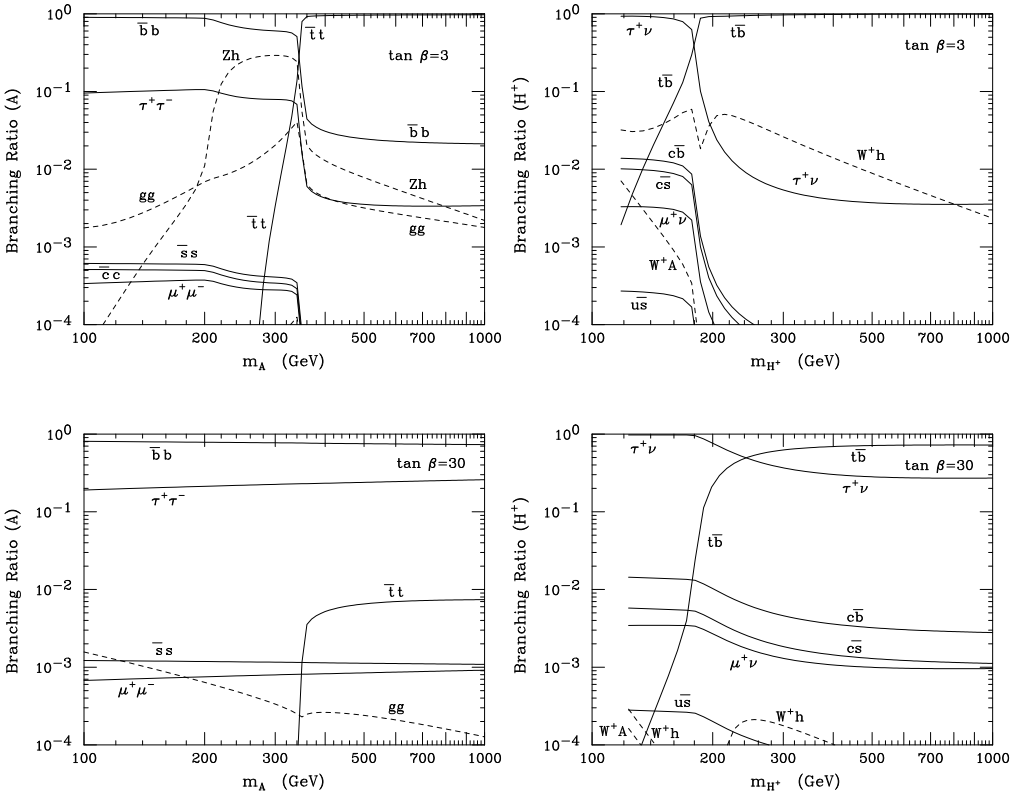

Figure 1.5: Branching ratios of the MSSM Higgs bosons A and $H^{\pm}$, with tanβ = 3 and 30, respectively. Final states labeled above include the possibility of one off-shell final state particle below the corresponding two-particle decay threshold. The above plots were made under the assumption that the average top and bottom squark masses are 1 TeV/c^2 and top-squark mixing is maximal. The range of $m_{H^{\pm}}$ shown corresponds to varying mA between 90 GeV/c^2 and 1 TeV/c^2. Other supersymmetric parameters have been chosen such that there are no supersymmetric particle decay modes in the Higgs mass ranges shown above.

SUSY decay modes

In addition to the decay modes of the MSSM Higgs bosons into fermion and gauge boson final states, there exist Higgs decay channels that involve scalars of the extended Higgs sector and supersymmetric final states. The unambiguous observation of these modes (as well as any decay mode of a charged scalar) would clearly constitute direct evidence of New Physics beyond the Standard Model.

Higgs decays into charginos, neutralinos and third-generation squarks and sleptons can become important, once they are kinematically allowed.
The Higgs bosons mainly couple to mixtures of higgsino and gaugino components. Therefore, in the limits $|\mu| \gg M_{1,2}, m_Z$ or $|\mu| \ll M_{1,2}$, i.e. in the gaugino or higgsino regions for the lightest ino states, the decays of the neutral Higgs bosons into pairs of identical neutralinos and charginos, $H_k \to \chi_i\chi_i$, will be strongly suppressed. In these limiting situations, the mixed decay channels $H/A \to \chi^0_{1,2}\chi^0_{3,4}, \chi^\pm_1\chi^\mp_2$ and $H^+ \to \chi^+_1\chi^0_{3,4}, \chi^+_2\chi^0_{1,2}$ will be the dominant ones for the heavy Higgs particles. In the mixed region, $|\mu| \sim M_2$, all decay channels occur at comparable rates when they are kinematically allowed. An exception to these rules occurs, however, for the neutral Higgs boson decays into neutralinos when the couplings accidentally vanish for certain values of tanβ and m_A.
The decay widths of the heavy neutral CP-even and the charged Higgs bosons into first and second generation squarks and sleptons (the pseudoscalar A boson cannot decay at tree-level into these states since the $A\widetilde{f}_i\widetilde{f}_i$ coupling is zero by virtue of CP-invariance and the $A\widetilde{f}_1\widetilde{f}_2$ coupling is proportional to $m_f \sim 0$) are proportional to $G_F m_W^4/m_H$ in the asymptotic regime $m_H \gg m_{\widetilde{f}}$. These decays are suppressed by the heavy Higgs mass and therefore unlikely to compete with the dominant decay modes into top and/or bottom quarks (and to charginos and neutralinos) for which the decay widths grow as m_H.
The situation is completely different for the decays into third generation sfermions and in particular into top squarks. Indeed, due to the large value of m_t the couplings of the Higgs bosons are strongly enhanced. The partial widths up to mixing angle factors are proportional to $G_F m_t^4/(m_H \tan 2\beta)$ and to $G_F m_t^2(\mu + A_t \tan\beta)^2/m_H$ where A_t is the stop trilinear coupling. For small tanβ values and not too heavy Higgs bosons, or for intermediate values of tanβ and for μ and A_t values of the order of ~ 1 TeV/c^2, the partial decay widths into top squarks can be very large and can compete with, and even dominate over, the decay channels into top quark (and into charginos/neutralinos).
The branching ratios for the decays of the heavier Higgs bosons A, H and $H^\pm$ into third generation sleptons and squarks, as well as into the competing chargino and neutralino final states, as a function of the Higgs masses are shown in Figure 1.6. The individual decays have been summed up. The chosen a scenario has tan$\beta = 10$ and the sfermions are rather light: the sfermion masses are $m_{\widetilde{Q}_i} = 2m_{\widetilde{l}_i} = 300$ GeV/c^2 with trilinear couplings $A_f = -2m_{\widetilde{f}}$, while the parameters in the ino sector are $M_2 = \mu = \frac{1}{2}M_1 = 2M_3 = 300$ GeV/c^2.

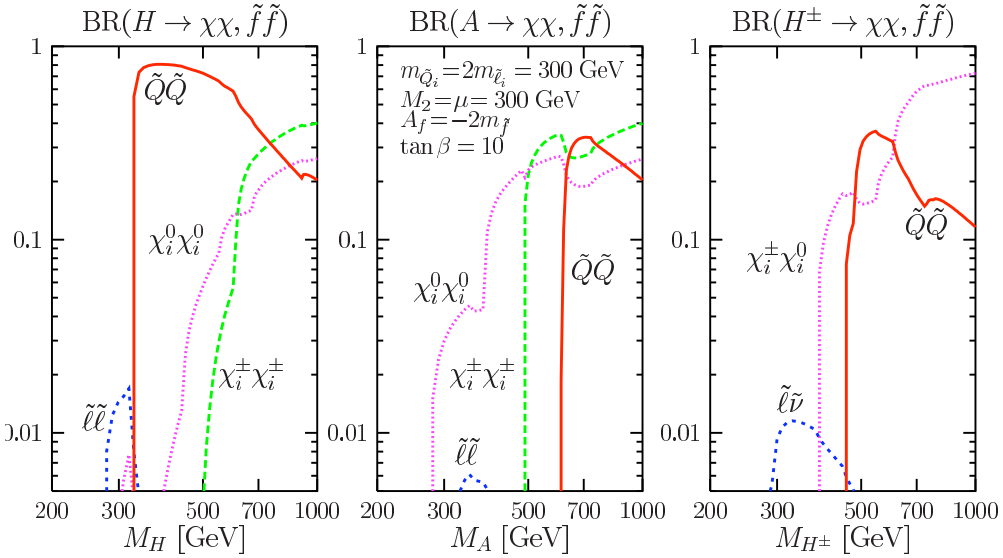

Figure 1.6: Branching ratios for the decays of the A, H, $H^\pm$ bosons into third generation sleptons and squarks and into charginos and neutralinos as a function of their masses. tanβ = 10 has been chosen and others SUSY parameters are as listed in the figure.

1.4 MSSM Higgs searches

1.4.1 Existing constrains on SUSY

The large electron-positron collider (LEP) at CERN ran at energies ranging from the Z peak up to $\sqrt{s}$ = 209 GeV/c^2. Running at the Z pole, the LEP experiments excluded many supersymmetric particles up to about half the Z mass. These limits come mainly from the comparison of the measured Z widths to SM expectations, and are relatively insensitive to the details of SUSY particle decays. The various SUSY particles considered at LEP typically decay directly to SM particles and LSPs, and therefore signatures consist of some combination of jets, leptons, possibly photons, and missing energy. Consequently the search criteria are geared toward a few distinct topologies. The main constrain is on the chargino masses which have been excluded up to 103 GeV/c^2 [19]. LEP has also provided lower limit on slepton masses, of which the strongest is $m_{\tilde{e}} \gtrsim 99$ GeV/c^2 [19].

While the LEP experiments can investigate a wide range of scenarios and cover corners of theoretical parameter space, they did not match the mass reach of the Tevatron experiments (CDF and DØ). The main source of signals for supersymmetry are squarks and gluinos. Pairs of squarks or gluinos are produced in s, t

and u-channel processes. These particles decay directly or via cascades involving at the end at least two χ_1^0s. The number of observed hadronic jets depends on whether the gluino or the squark is the heaviest, with the latter occurring in mSUGRA models. The searches [20] rely on large missing transverse energy ($\not\!\!E_T$) caused by the escaping neutralinos. Jets with high transverse energy are also required as evidence of a hard interaction; care is taken to distinguish genuine $\not\!\!E_T$ from fluctuations in the jet energy measurement. The bounds traditionally are derived for the $(m_{\tilde{g}}, m_{\tilde{q}})$ plane. The most recent analysis by the CDF Collaboration places significantly stronger bounds than previous analyses [21].

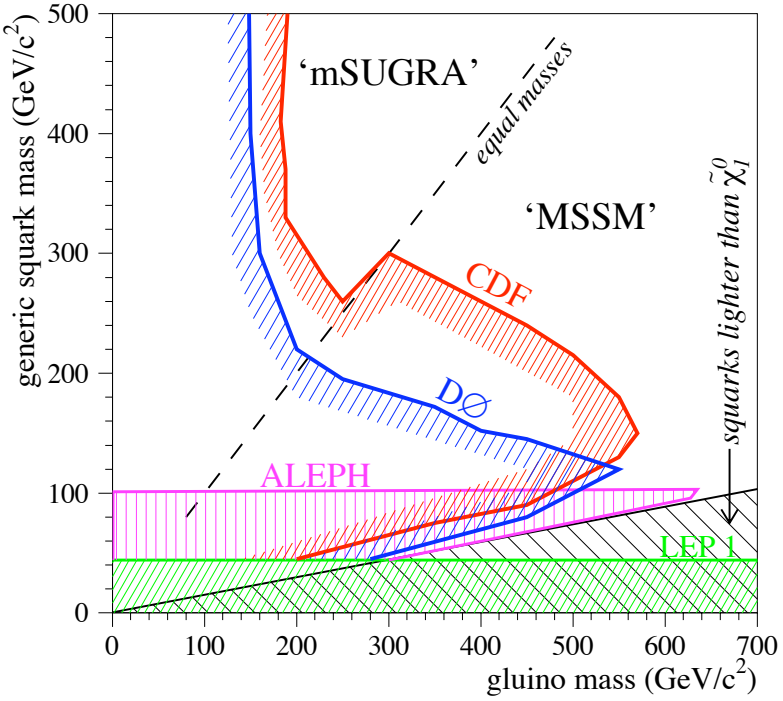

Figure 1.7: Regions in the $(m_{\tilde{g}}, m_{\tilde{q}})$ plane excluded by searches for jets and missing energy at CDF, DØ, and LEP.

If squarks are heavier than gluinos, then $m_{\tilde{g}} > 195$ GeV/c^2. If they all have the same mass, then that mass is at least 300 GeV/c^2. If the squarks are much lighter than the gluino, the bound on the gluino mass is generally high, much higher than 300 GeV/c^2. A small region in which the neutralino-squark mass difference is small, is covered by the LEP experiments (see Figure 1.7).

1.4.2 MSSM Higgs limits

The search of the neutral Higgs bosons in the associated production processes $e^+e^- \rightarrow hA$ and HA, allowed the LEP collaborations to set the limits to a 95% confidence level (CL) on the h and A boson masses [22] The measurements yield lower bounds of 91.0 and 91.9 GeV/c^2 for the h and A bosons. Figure 1.8 shows the excluded regions in four bidimensional projections. As can be seen a significant portion of the parameter space is excluded, values $0.9 < \tan\beta < 1.5$ are ruled out at the 95% CL.
Searches for the MSSM Higgs bosons performed at the Tevatron have obtained bounds not yet competitive with the LEP constrains [23].

1.4.3 MSSM Higgs searches at LHC

The most promising channel to investigate the heavy Higgs sector of a SUSY theory at the future collider is the $A/H \rightarrow \tau\tau$ channel. The $A/H \rightarrow \mu\mu$ channel, although with a small branching ratio, offers the interesting possibility of allowing for a precise reconstruction of the Higgs boson mass. These channels have been shown to cover large parts of the intermediate and high $\tan\beta$ region of the MSSM parameter space for an integrated luminosity of 30 fb^{-1} [24]. The lighter scalar MSSM Higgs boson is accessible through the inclusive $h \rightarrow \gamma\gamma$ ($m_A > 200$ GeV/c^2) and $h \rightarrow bb$ ($m_A > 200$ GeV/c^2) decay channels [25]. The heavy charged Higgs bosons can be searched for at large $\tan\beta$ with the $H^\pm \rightarrow \tau\nu_\tau$ decay channel in the associated production and in the direct production, and with the $H^\pm \rightarrow tb$ decay channel in the associated production. The $H^\pm \rightarrow \tau\nu_\tau$ decay channel in the associated production yields the highest sensitivity. The light charged Higgs bosons are accessible for $m_{H^\pm} < 140$ GeV/c^2 through tt production [26].
Figure 1.9 show the 5σ discovery contours for A/H (left) and h (right) MSSM Higgs bosons detection in various channels in the $m_A - tan\beta$ plane, assuming an integrated luminosity of $\mathcal{L} = 30$ fb^{-1} at LHC for the CMS detector [27]. In these studies, the heavy Higgs bosons decay into SM particles as it is assumed that sparticles are too heavy to participate in the decay processes.
The possibility that, on the contrary, sparticles could be light enough so that the Higgs decays to sparticles could be kinematically allowed has been recently investigated [28]. Higgs bosons decaying into sparticles might therefore open possibilities to explore regions of the parameter space otherwise inaccessible via SM-like decays into ordinary particles [29]. This is the case in particular in the difficult low and intermediate $\tan\beta$ region of the MSSM parameter space. One of the most promising channels is the A/H decay into a pair of next-to-lightest

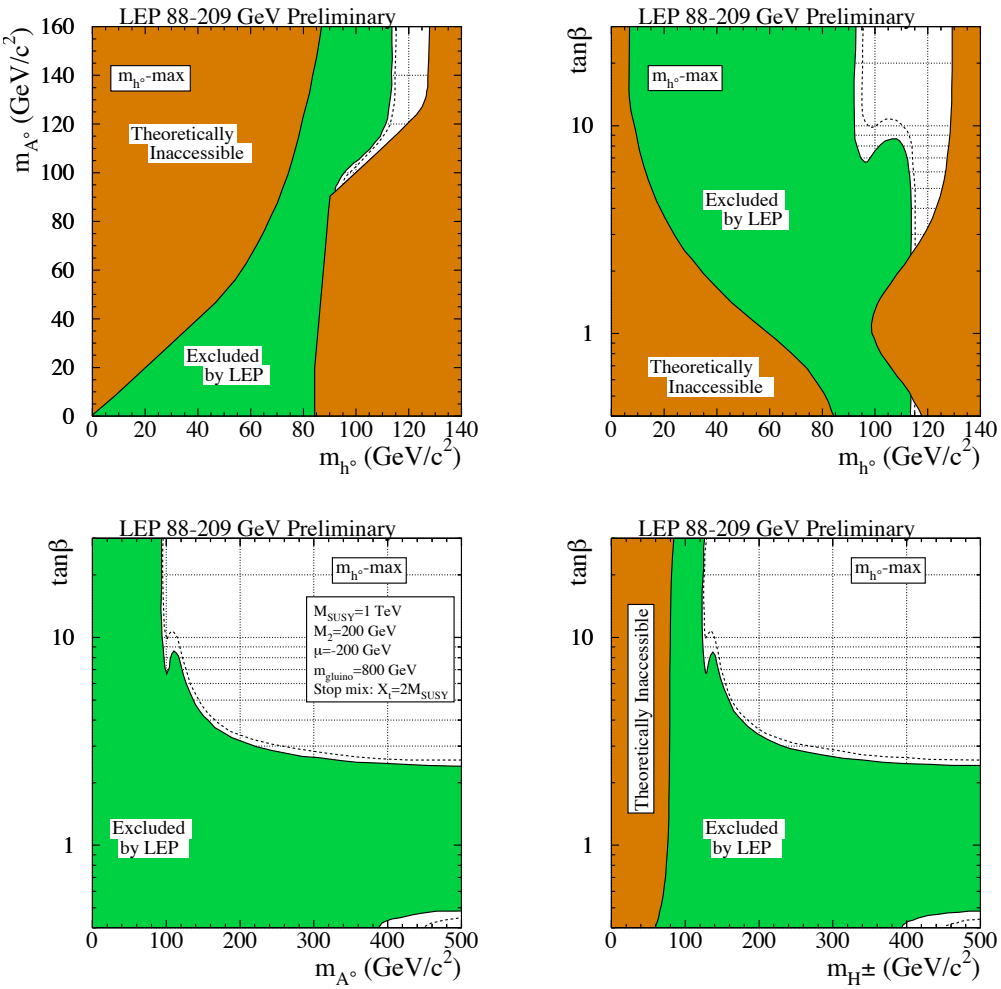

Figure 1.8: The MSSM Higgs exclusion plots. The excluded (diagonally hatched) and theoretically disallowed (cross hatched) regions are shown as a functions of the MSSM parameters in the four projection: (top left) the (m_h, m_A) plane, (top right) the $(m_h$,tan$\beta)$ plane, (bottom left) the $(m_A$,tan$\beta)$ plane, (bottom right) the $(m_{H^\pm}$,tan$\beta)$ plane. The dashed lines indicate the boundaries of the regions expected to be excluded at the 95% CL if only SM backgrounds processes are present. A top mass of 175 GeV/c^2 is assumed.

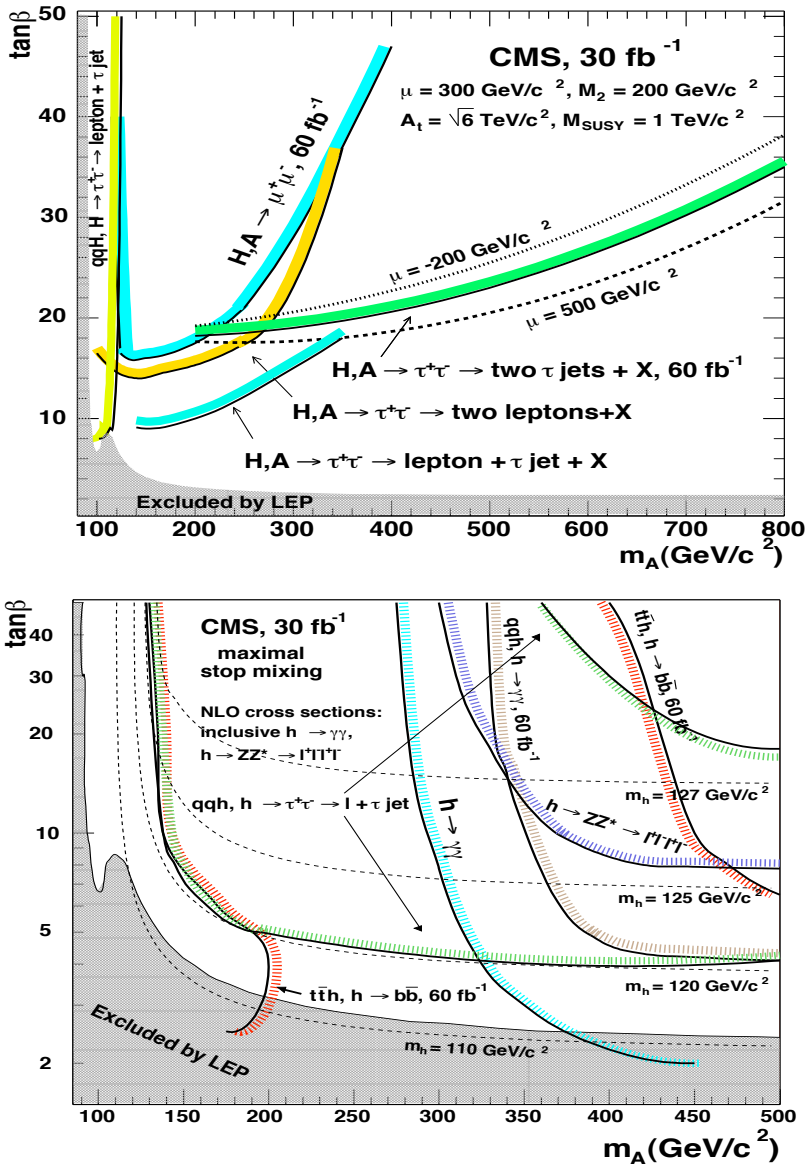

Figure 1.9: 5σ discovery contours for A/H (top) and h (bottom) MSSM Higgs bosons detection in various channels in the $m_A - tan\beta$ plane, assuming an integrated luminosity of $\mathcal{L} = 30$ fb^{-1} and using the CMS detector.

neutralinos, χ_2^0, followed by the leptonic decay $\chi_2^0 \to l^+l^-\chi_1^0$ (with $l = e, \mu$). This process results in a clean four lepton plus missing transverse energy ($\not{E}_T$) final state signature:

$$A/H \to \chi_2^0\chi_2^0 \to 4l^\pm + \not{E}_T \ (l = e, \mu).$$

This channel will therefore be investigated in detailed in this thesis.

1.5 Summary

In this chapter a phenomenological overview of the MSSM Higgs sector which is the main subject of this work.
The principles of the supersymmetry (SUSY) have been briefly reviewed and it has been shown how SUSY provides a satisfactory solution to most of the defects of the Standard Model.
The particle content of the Minimal Supersymmetric Model (MSSM) has been discussed. In the MSSM, every Standard Model particle has a supersymmetric partner that differs from it by half a unit in spin. This leads the introduction of *sleptons* and *squarks* as the superpartners of leptons and quarks, and *neutralinos* and charginos as superpartners of gauge and Higgs bosons. The introduction of the R-parity, a discrete symmetry, has a consequence that supersymmetric particles are only produced in pairs and that there exists a stable Lightest Supersymmetric Particle (LSP). The phenomenologically important aspects of neutralino, chargino, squark and slepton are discussed. Since in a fully supersymmetric theory the masses of the superpartners should be equal to the masses of their Standard Model counterparts, which is clearly not the case, supersymmetry must necessarily be a broken symmetry.
The Higgs sector of the MSSM has been described. Contrary to the Standard Model, the Higgs sector now contains five physical Higgs bosons: two CP-even neutral scalars, h and H, one CP-odd neutral scalar, A, and a pair of charged Higgs boson, $H^\pm$. At tree level, their masses and couplings are determined by only two parameters, m_A and $\tan\beta$.
The MSSM Higgs bosons decay modes are discussed. The decay rate depends to a large extent on their couplings to fermions and gauge bosons as well as their self couplings. In addition to the decay modes in SM particles, there exist Higgs decay channels that involve scalars of the extended Higgs sector and supersymmetric final states. The unambiguous observation of these modes would clearly constitute direct evidence of New Physics beyond the Standard Model.
The Higgs production mechanisms at hadron collider are reviewed. As in the case of the decay modes, the cross sections depend on the couplings to fermions

and gauge bosons. Because of the different couplings of the Higgs particles to fermions and gauge bosons, the pattern for the production rates is significantly different from the SM case, in addition in the presence of sparticles relatively light, they can substantially contribute to the processes.
The experimental constraints on the MSSM parameter space, provided by direct searches at the colliders are presented together with the existing MSSM Higgs limits. The MSSM Higgs searches LHC are finally shown. The decay modes of the heavy neutral Higgs bosons into sparticles can provide clean signature in the difficult low $\tan\beta$ region.

Chapter 2

The CMS experiment at the Large Hadron Collider

The Large Hadron Collider is the new particle accelerator under construction at CERN which will collide protons at the centre of mass energy $\sqrt{s} = 14$ TeV with a design luminosity of $10^{34}\text{cm}^{-2}\text{s}^{-1}$.
An overview of the machine and of the requirements for the LHC experiments is given in Section 2.1. The general description of the CMS detector is presented in Section 2.2 A more detailed description of the CMS electromagnetic calorimeter is given in Section 2.3

2.1 The LHC proton-proton collider

The Large Hadron Collider [30], LHC, is a proton-proton collider which is under construction at CERN in the already existing LEP tunnel.
The choice was to construct an high energy and high luminosity[1] collider in order to reach a large range of physics opportunities, from the precise measurement of the properties of known objects to the exploration of high energy frontiers.
The LHC will produce collisions at centre-of-mass energy of $\sqrt{s} = 14$ TeV end at a design luminosity of $10^{34}\text{cm}^{-2}\text{s}^{-1}$. The machine comprises 1232 dipole magnets, with radio frequency cavities providing a "kick" that results in an increase in the proton energy of 0.5 MeV/turn. The collider luminosity is given by:

$$\mathcal{L} = \frac{N^2 k f \gamma}{4\pi\epsilon_n \beta^\star} F \tag{2.1}$$

[1]The luminosity, $\mathcal{L}$, is the factor of proportionality between the event rate, R, and the interaction cross section, σ_{int}.

where N is the number of particles in each of the k circulating bunches, f the revolution frequency, $\beta^\star$ the value of the betatron function at the crossing point and ϵ_n the emittance corresponding to one σ contour of the beam (nominal value 3.75 μm), normalized by dividing a Lorentz factor γ and F is the reduction factor due to the crossing angle.
Thus, to achieve high luminosity, the LHC is made of a high number of populating bunches, 2,808 bunches filled with an average of 1.1×10^{11} protons, which collide at an high frequency, 40 MHz. In the first three years of operation, the LHC will run at a reduced luminosity of $10^{33}\text{cm}^2\text{s}^{-1}$. The two luminosity regimes are commonly called *high luminosity* ($10^{34}\text{cm}^2\text{s}^{-1}$) and *low luminosity* ($10^{33}\text{cm}^2\text{s}^{-1}$), respectively.
The LHC will also be able to accelerate and collide beams of heavy ions such as Pb at 2.76 A TeV to study the deconfined state of QCD matter, the quark-gluon plasma.
The main machine parameters are listed in Table 2.1.

		pp	$Pb-Pb$	
Energy per nucleon	E	7	2.76	TeV
Dipole field at 7 TeV	B	8.33	8.33	T
Design Luminosity	$\mathcal{L}$	10^{34}	10^{27}	$\text{cm}^{-2}\ \text{s}^{-1}$
Bunch separation		25	100	ns
No. of bunches	k_B	2808	592	
No. particles per bunch	N_p	1.15×10^{11}	7.0×10^7	
β-value at IP	β^*	0.55	0.5	m
RMS beam radius at IP	σ^*	16.7	15.9	μm
Luminosity lifetime	τ_L	15	6	hr
Number of collisions/crossing	n_c	≈ 20	–	

Table 2.1: The machine parameters relevant for the LHC detectors.

In Figure 2.1 the cross sections for the main processes in proton-proton collisions are shown as a function of the centre of mass energy.
The expected total pp cross section is $\sigma_{tot} \approx 100$ mb and the inelastic cross section is $\sigma_{in} = 60$ mb. The inelastic interactions are divided into two classes. The first one consists of head on interactions at small distance between two partons coming from the two colliding protons. These interactions are characterized by high transferred momentum and lead to the creation of massive particles at large angle with respect to the beam line. Unfortunately these events are rare. The majority of the interactions consists of *minimum bias events*, large distance between the two interacting partons, with a small transferred momentum and a

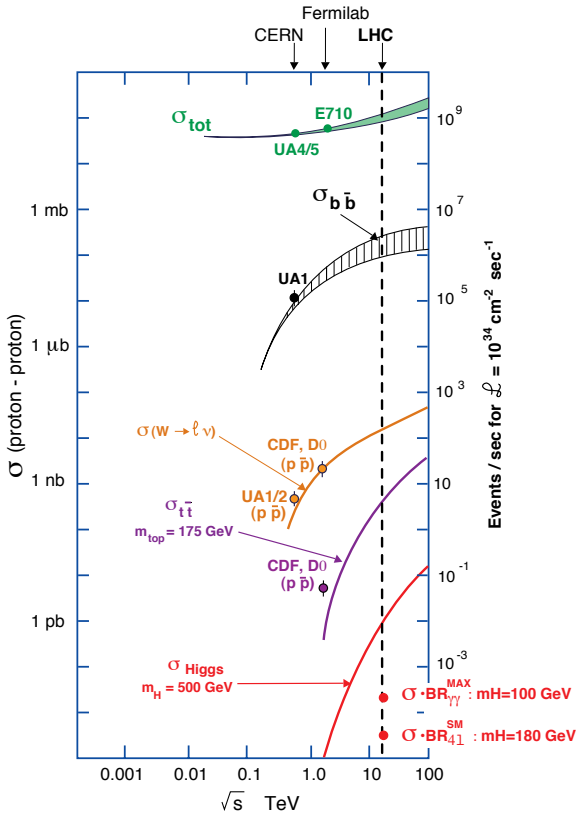

Figure 2.1: Cross sections for different processes in a proton-proton collision as a function of the centre of mass energy.

low transverse momentum in the final state.

With the LHC nominal parameters, about 20 minimum bias events are expected on average per bunch crossing at high luminosity, giving a significant pile-up to each triggered interaction. Furthermore the detectors have to face the problem of large QCD backgrounds with cross sections orders of magnitude larger than those for interesting events. Such a difficult environment imposes important constraints on the detectors design. A fast response (of the order of 25-50 ns) and a fine granularity are needed to separate the large number of particles and to minimize the pile-up effects. The high events rate ($\sim 10^{9}$ events/s) makes a fast and efficient trigger and data acquisition system necessary. Finally, due to the high flux of particles, a good radiation resistance for all the detector components is required, especially in the forward regions.

Four detectors will be installed at the LHC. ATLAS [32] and CMS [33], both general purpose detectors, will be installed in the two high luminosity interaction points. LHCb [35], devoted to B-physics studies and ALICE [34], dedicated

to the study of heavy ions collisions, will operate instead at a reduced luminosity. In the following a brief description of the CMS detector, used for the work described in this thesis, is given.

2.2 The CMS detector

CMS (Compact Muon Solenoid) is a general purpose detector that will be installed at the interaction point number 5 along the LHC tunnel.
An important aspect driving the detector design and layout is the choice of the magnetic field configuration for the muons momentum measurement. Large bending power is needed to measure precisely the momentum of charged particles. This leads to the choice of superconducting technology for the magnets.
The overall layout of CMS is shown in Figure 2.2. At the heart of CMS sits a 13-m-long, 5.9 m inner diameter, 4 T superconducting solenoid. Such high magnetic field was chosen in order to achieve good momentum resolution within a compact spectrometer. The return field is large enough to saturate 1.5 m of iron, allowing 4 muon "stations" to be integrated to ensure robustness and full geometric coverage. The core of the magnet coil is also large enough to accommodate the inner tracker, the calorimetries with the exception of the very-forward part.
The natural coordinate frame to describe the detector is a right handed cartesian system with the x axis pointing toward the centre of the LHC ring, the z axis directed along the beam axis and the y axis directed upward. Given the cylindrical symmetry of CMS, a convenient coordinate system is given by the triplet (r, ϕ, η), being r the distance from the z axis, ϕ the azimuthal coordinate with respect to the x axis and η the pseudorapidity, which is defined as $\eta = \ln(\tan(\theta/2))$, where θ is the polar angle with respect to the z axis.
The overall dimensions of the CMS detector are a length of 21.6 m, a diameter of 14.6 m and a total weight of 12 500 tons.
The construction, installation and commissioning of CMS is progressing well, though not without difficulties, towards the goal of being ready for collisions in the second half of 2007.
A brief description of each subdetector follows in the next sections.

2.2.1 The inner tracking system

The CMS inner tracking [36] is the sub-detector closest to the interaction point, located in the 4 T magnetic field of the superconductive solenoid.
The tracker must be able to operate without degrading its performances in the

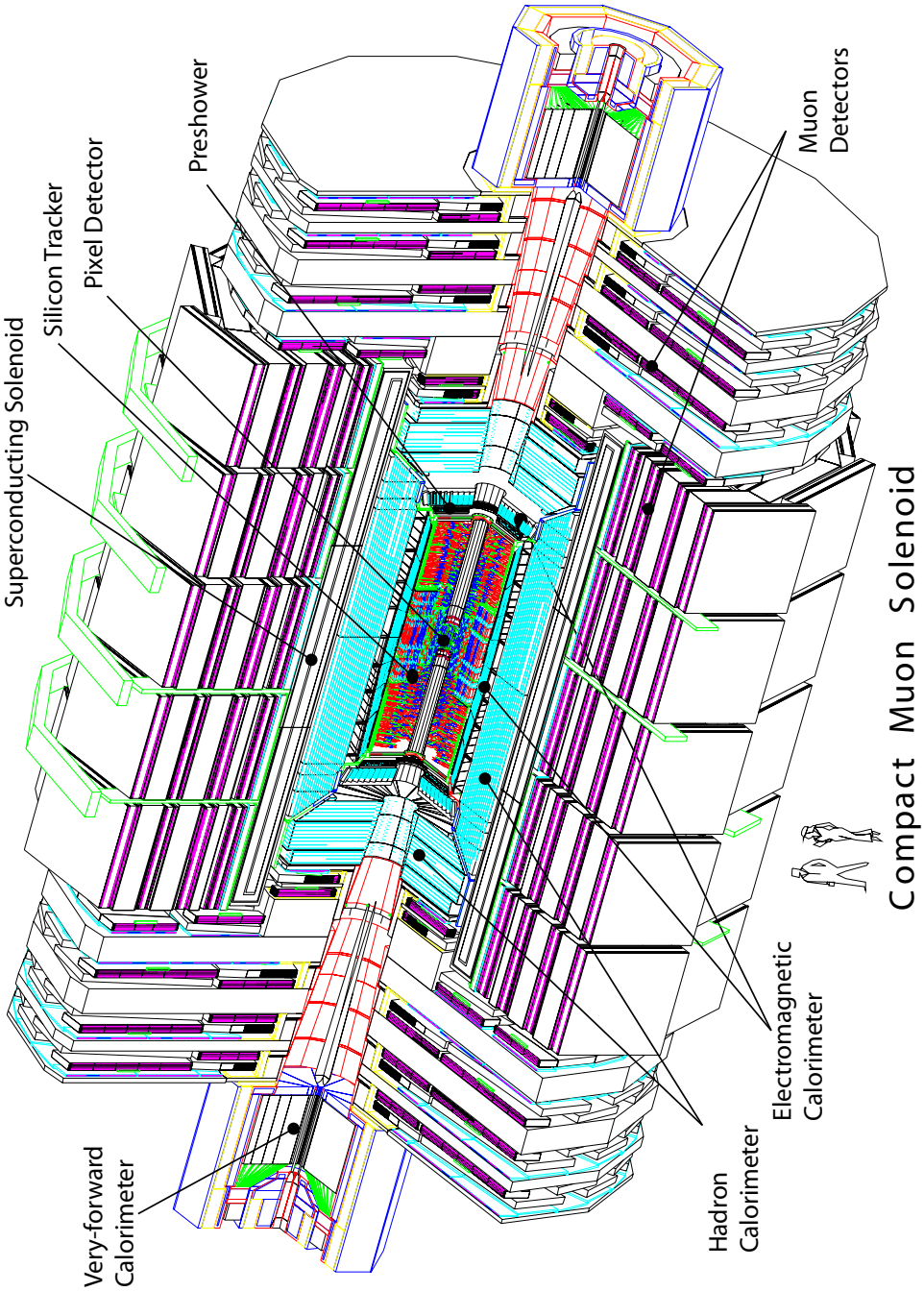

Figure 2.2: An exploded view of the CMS detector.

hard radiation environment of LHC and it has to comply with severe material budget constraints, in order to not degrade the excellent energy resolution of the electromagnetic calorimeter.
The layout of the CMS tracker is shown in Figure 2.3. The outer radius of the CMS tracker extends to nearly 110 cm and to $|z| = 270$ cm.

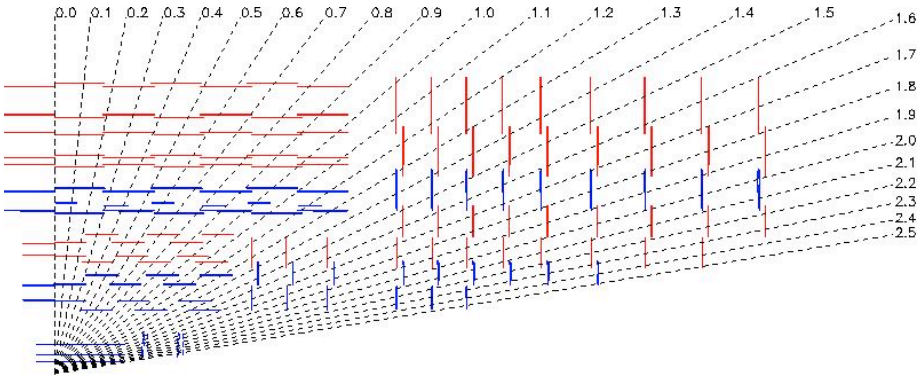

Figure 2.3: The tracker layout (1/4 of the z view).

The inner tracking system is constructed using the silicon technology for the whole detector. The tracker is decomposed in three subsystem according to the particle fluence and it comprises 66 million pixels and 9.6 million silicon strips.

- The region closest to the interaction vertex, where the particle flux is the highest ($r \approx 10$ cm), pixel detectors are located. The pixel size is $\approx 100 \times 150$ μm^2, giving a typical occupancy of about 10^{-4} per pixel per LHC crossing.

- The intermediate region ($20 < r < 55$ cm) where the particle flux is low enough to enable the use of silicon microstrip detectors with a minimum cell size of 10 cm $\times$ 80 μm, leading to an occupancy of $\approx$ 2–3% per LHC crossing..

- The outermost region ($r > 55$ cm) where the particle flux has dropped sufficiently to allow the use of larger-pitch silicon microstrips with a maximum cell size of 25 cm $\times$ 180 μm, while keeping the occupancy down to $\approx$ 1% per LHC crossing.

The tracker has two basic properties to solve the pattern recognition problem: low cell occupancy and large hit redundancy.
The low occupancy is obtained by working with high granularity detectors, mainly the ones closer to the interaction point because they have to cope with higher particle fluxes, and fast primary charge collection.

The redundancy is guaranteed by the overall design which allows for many measured points per track. For the muons and the pions an average of 12-14 points (hits) per track are guaranteed to permit a high tracking efficiency and a low rate (10^{-3} or less) of fake tracks.
The performances of the tracker are illustrated in Figure 2.4, which shows the transverse momentum and impact parameter resolutions in the r-ϕ and z planes for single muons with a p_T of 1, 10 and 100 GeV/c, as a function of pseudorapidity.

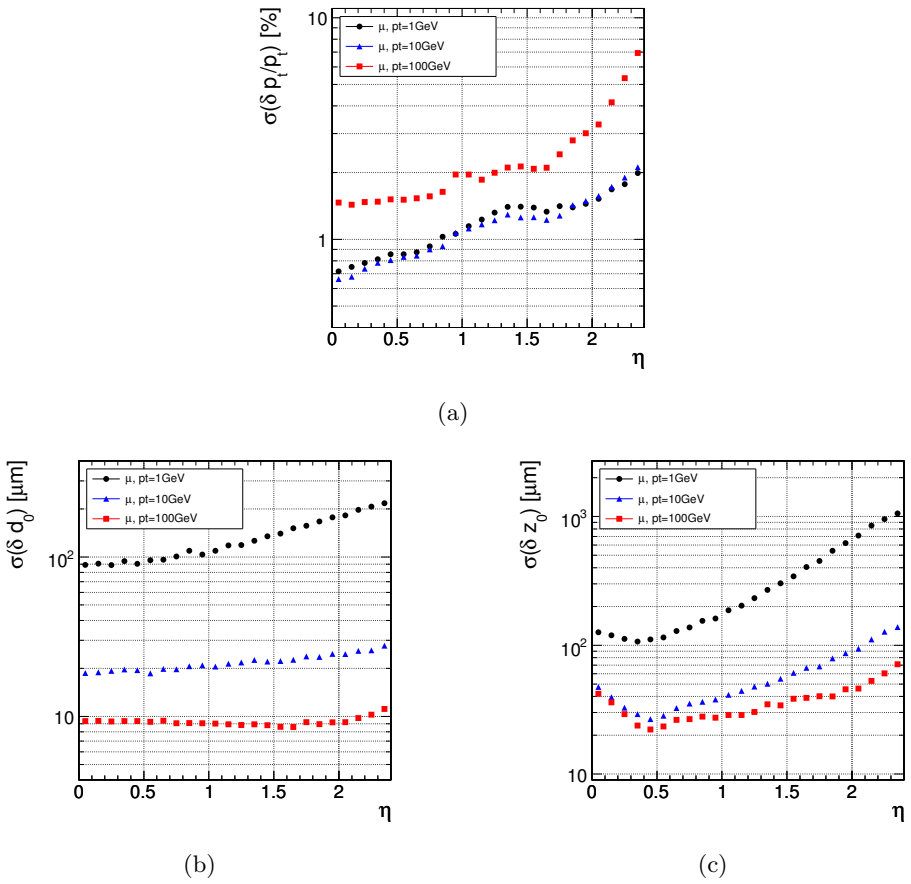

Figure 2.4: Resolution of several track parameters for single muons with transverse momenta of 1, 10 and 100 GeV/c: (a) transverse momentum, (b) transverse impact parameter, and (c) longitudinal impact parameter.

Global track reconstruction efficiency as a function of pseudorapidity for single muons and pions is shown in Figure 2.5. For hadrons, the global track reconstruction efficiency is obviously lower than for muons because hadrons interact with the material present in the tracker. In the case of the electron track reconstruction, the efficiency is influenced by the additional presence of the bremsstrahlung

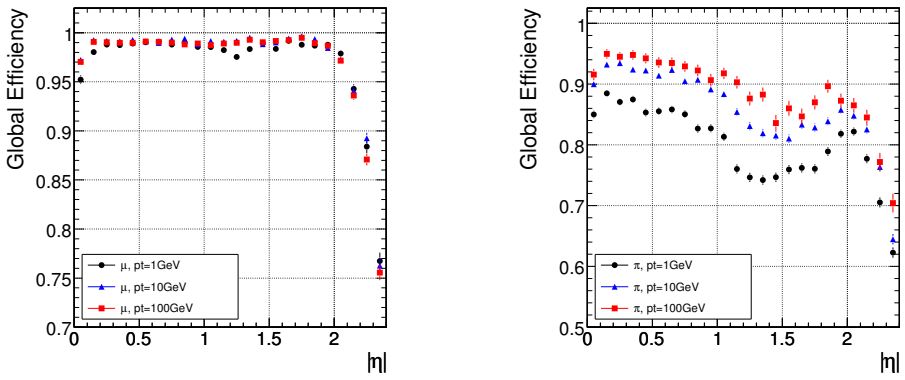

(a) (b)

Figure 2.5: Global track reconstruction efficiency for muons (a) and pions (b) of transverse momenta of 1, 10 and 100 GeV/c.

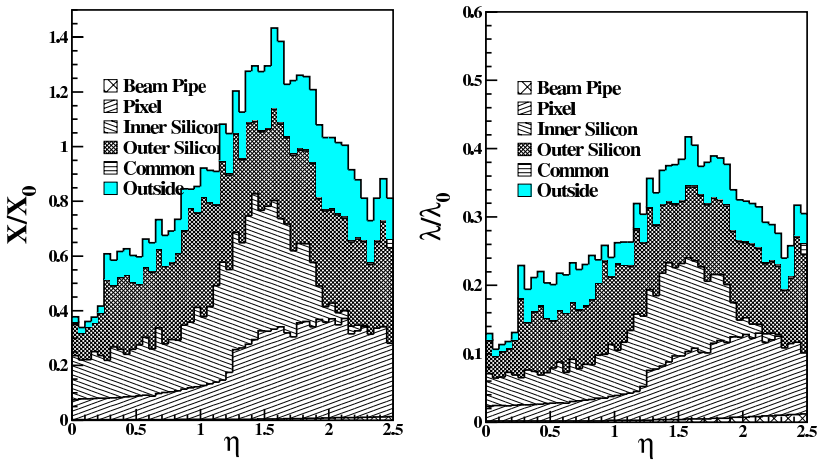

Figure 2.6: Material budget in units of radiation length (left) and in units of interaction length (right) as a function of η for the different subunits. The peak around $\eta = 1.5$ corresponds to the cables and services of the tracker.

radiation (see Chapter 4).
The material inside the active volume of the tracker increases from $\approx 0.4\ X_0$ at $\eta = 0$ to around $1\ X_0$ at $|\eta| \approx 1.6$, before decreasing to $\approx 0.6\ X_0$ at $|\eta| = 2.5$ (see Figure 2.6).

2.2.2 The electromagnetic calorimeter

A high performance electromagnetic calorimeter (ECAL) [37] is a tool for any general purpose LHC experiment, in order to have precise measurements on electrons and photons.

The CMS collaboration has chosen an homogeneous calorimeter composed with finely segmented crystals of lead tungstate ($PbWO_4$), a radiation resistant and chemically inert scintillator suited to work in the LHC high dose rate environment.
A detailed description of the electromagnetic calorimeter is given in Section 2.3.

2.2.3 The hadron calorimeter

The design of the hadron calorimeter (HCAL) [38] is strongly influenced by the choice of magnet parameters since most of the CMS calorimetry is located inside the magnet coil and surrounds the ECAL system. An important requirement of the HCAL is to minimize the non-Gaussian tails in the energy resolution and to provide good containment and hermeticity for the missing transverse energy and jet energy measurements.
The HCAL is divided into an Hadron Barrel (HB) and two Hadron Endcaps (HE) inside the magnet coil. This is complemented by an additional layer of scintillators, referred to as the Hadron Outer (HO) detector, located after the coil. To improve the hermeticity an Hadron Forward (HF) calorimeter is placed outside the magnet yoke, ±11 m away along the beam direction from the nominal interaction point (see Figure 2.7).

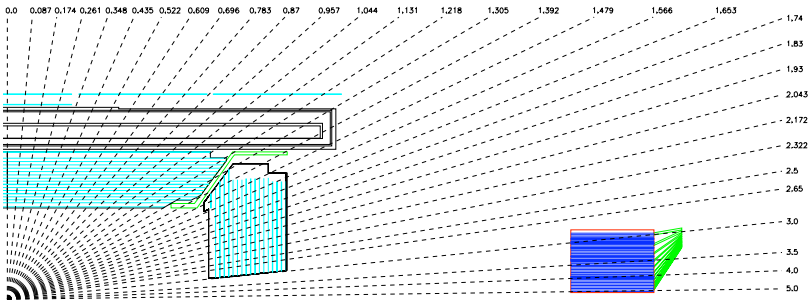

Figure 2.7: The HCAL layout (1/4 of the z view). The hadron calorimeter is subdivided into Hadron Barrel (HB) and Hadron Endcap (HE), placed inside the magnetic coil, the Hadron Outer (HO) detector and the Hadron Forward (HF) calorimeter.

Brass has been chosen as absorber material as it has a reasonably short interaction length, is easy to machine and is non-magnetic. In addition, brass has a fairly low Z, so it doesn't degrade the muon momentum measurement.
Maximizing the amount of interaction lengths before the magnet requires keeping to a minimum the amount of space devoted to the active medium. The tile/fibre technology makes for an ideal choice. It consists of 3.7 mm thick active layers of plastic scintillators read out with embedded wavelength-shifting (WLS)

fibres. The photodetection readout is based on multi-channel hybrid photodiodes (HPDs).

Readout cells in HCAL are arranged in towers pattern in η, ϕ space, projective to the nominal interaction point. The cells in the barrel region have segmentation of $\Delta\eta \times \Delta\phi = 0.087 \times 0.087$ becoming progressively larger in the endcap and forward regions. The overall assembly enables the HCAL to be built with essentially no uninstrumented cracks or dead areas in ϕ. The gap between the barrel and the endcap HCAL, through which the services of the ECAL and the inner tracker pass, is inclined at 53° and points away from the centre of the detector. The thickness in interaction lengths varies from $7 - 11\ \lambda_I$ depending of η.

For gauging the performances of the HCAL, it is usual to look at the jet energy resolution and the missing transverse energy resolution.

The granularity of the sampling in the three parts of the HCAL has been chosen such that the jet energy resolution, as a function of E_T, is similar in all three parts. This is illustrated in Figure 2.8.

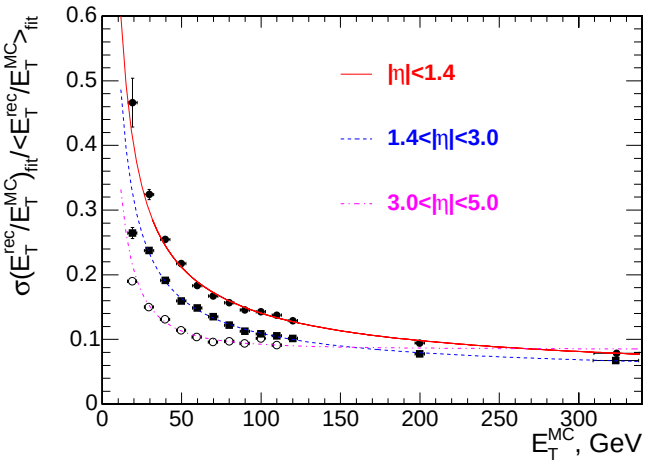

Figure 2.8: The jet transverse energy resolution as a function of the simulated jet transverse energy for barrel jets ($|\eta| < 1.4$), endcap jets ($1.4 < |\eta| < 3.0$) and very forward jets ($3.0 < |\eta| < 5.0$). The jets are reconstructed with the iterative cone $R = 0.5$ algorithm.

The resolution of the missing transverse energy ($\not\!\!E_T$) in QCD dijet events with pile-up is given by

$$\sigma(\not\!\!E_T) \approx 1.0\sqrt{\Sigma E_T} \tag{2.2}$$

without any corrections the average $\not\!\!E_T$ is given by

$$\langle \not\!\!E_T \rangle \approx 1.25\sqrt{\Sigma E_T}\ . \tag{2.3}$$

2.2.4 The muon system

A huge muon detection system [39] is placed outside the magnet coil. Three types of gaseous detectors, integrated in the iron return yoke of the magnet, are used. The choice of the detector technologies has been driven by the very large surface to be covered and by the different radiation environments. In the barrel region ($|\eta| < 1.2$), where the neutron induced background is small, the muon rate is low and the residual magnetic field in the chambers is low, drift tube (DT) chambers are used. In the two endcaps, where the muon rate as well as the neutron induced background rate is high, and the magnetic field is also high, cathode strip chambers (CSC) are deployed and cover the region up to $|\eta| < 2.4$. In addition to these, resistive plate chambers (RPC) are used in both the barrel and the endcap regions for triggering and time measurements. The layout of one quarter of the CMS muon system for initial low luminosity running is shown in Figure 2.9.

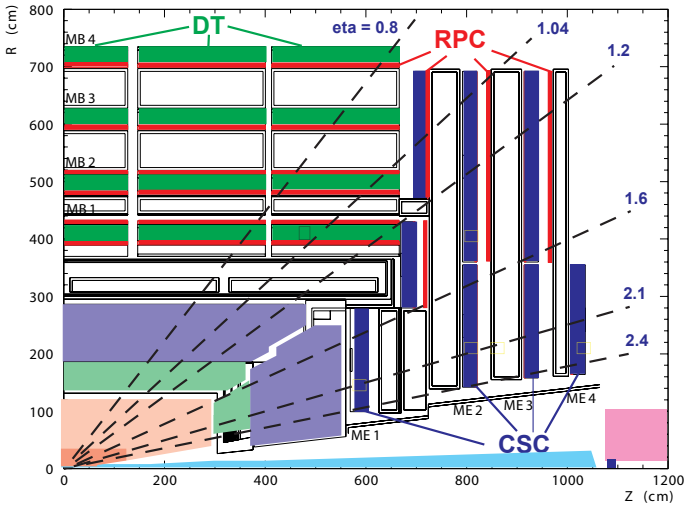

Figure 2.9: Layout of one quarter of the CMS muon systemfor initial low-luminosity running. The RPC system is limited to $|\eta| < 1.6$ in the endcap, and for the CSC system only the inner ring of the ME4 chambers have been deployed.

An innovative aspect of the muon system is the possibility of the combined DT/CSC detectors to operate standalone as trigger. It guarantees solidity and redundancy to muon trigger measurements.
Centrally produced muons are measured three times: in the inner tracker, after the coil, and in the return flux. Measurement of the momentum of muons using only the muon system is essentially determined by the muon bending angle at the exit of the 4 T coil, taking the interaction point (which will be known to

$\approx 20\mu$m) as the origin of the muon.
The resolution of this measurement (labelled "muon system only" in Figure 2.10) is dominated by multiple scattering in the material before the first muon station up to p_T values of 200 GeV/c, where the chamber spatial resolution starts to dominate. For low-momentum muons, the best momentum resolution (by an order of magnitude) is given by the resolution obtained in the silicon tracker ("inner tracker only" in Figure 2.10). However, the muon trajectory is extrapolated inward in order to combine it with the inner tracking system. This fact can be used to improve the muon momentum resolution at high momentum when combining the inner tracker and muon detector measurements ("full system" in Figure 2.10).

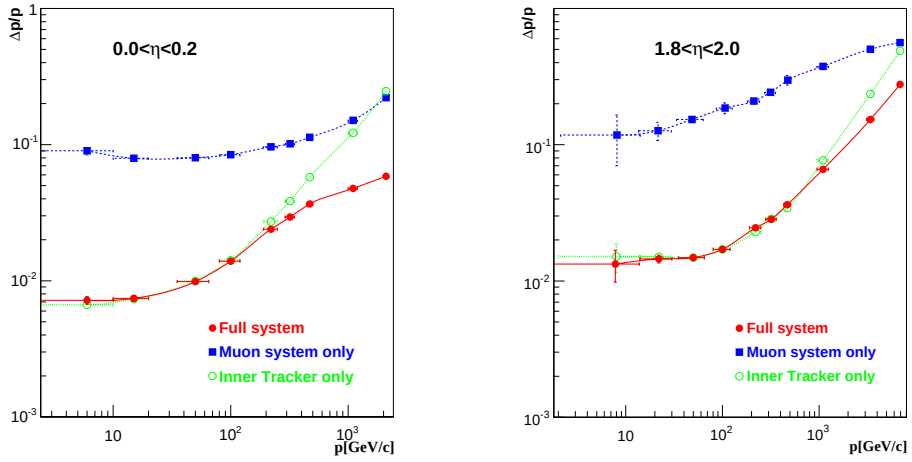

(a) (b)

Figure 2.10: The muon momentum resolution versus p using the muon system only, the inner tracker only, or both ("full system"). a) $|\eta| < 0.2$. b) $1.8 < |\eta| < 2.0$.

2.2.5 The magnet

The required performances of the muon system, and hence the bending power, is defined by the narrow states decaying into muons and by the unambiguous determination of the sign for muons with a momentum of $\approx$ 1 TeV/c. This requires a momentum resolution of $\Delta p/p \approx 10\%$ at $p = 1$ TeV/c. The presence of the field improves the momentum measurement of charged particles thanks to the use of the curvature radius and at the same time reduces the effect of the pile-up by preventing the low energy particles to reach the calorimeters.
CMS chose a large superconducting solenoid, the parameters of which are given

in Table 2.2 [40]. A large bending power can be obtained for a modestly-sized solenoid, albeit a high-field superconducting one, as the bending starts at the primary vertex. A favourable length/radius ratio is necessary to ensure good momentum resolution in the forward region as well.

Field	4 T
Inner Bore	5.9 m
Length	12.9 m
Number of Turns	2168
Current	19.5 kA
Stored energy	2.7 GJ

Table 2.2: Parameters of the CMS superconducting solenoid.

2.2.6 The trigger and the data acquisition

The LHC bunch crossing rate of 40 MHz leads to 10^9 interactions/s at the design luminosity. Data from order of magnitude of 10^2 crossings/s can be written to mass storage, hence, the trigger system has to achieve a rejection factor of nearly 10^6.
The CMS trigger and data acquisition system [41][42] consists of 4 parts: the detector electronics, the readout network, the Level-1 trigger processors (calorimeter, muon and combination of both) and an online event filter system (processor farm) that executes the software for the High-Level Triggers (HLT)

The Level-1 trigger

The Level-1 trigger is implemented on custom-built programmable hardware. The total time allocated for the transit and for reaching a decision to keep or discard data from a particular bunch crossing is 3.2 μs. During this time, the detector data must be held in buffers while trigger data is collected from the front-end electronics and decisions reached that discard a large fraction of events while retaining the small fraction of the interactions of interest (nearly 1 crossing in 1000).
The Level-1 triggers involve the calorimetry and muon systems, as well as some combination of information between these systems. The Level-1 decision is based on the presence of "trigger primitive" objects such as photons/electrons, muons, and jets above set E_T or p_T thresholds. It also uses global sums of E_T and $\not{E}_T$. Reduced-granularity and reduced-resolution data are used to form trigger

objects. At startup the Level-1 rate will be limited to 50 kHz (the design value is 100 kHz). Taking a safety margin of a factor of 3 into account for simulation uncertainties, as well as beam and detector conditions not included in the simulation programs, leads to an estimated rate of 16 kHz. The design value of 100 kHz is defined by the average time to transfer the full detector information through the readout system.

High-Level triggers

Upon receipt of a Level-1 trigger, after a fixed time interval of about 3.2 μs, the data from the pipelines are transferred to the front-end readout buffers. After further signal processing, zero-suppression and/or data-compression, the data are placed in dual-port memories for access by the DAQ system. Each event, with a size of about 1.5 MB (pp interactions), is contained in several hundred front-end readout buffers. Through the event building "switch," data from a given event are transferred to a processor. Each processor runs the same high-level trigger (HLT) software code to reduce the Level-1 output rate of 100 kHz to 100 Hz. The output rate to be stored on mass storage is subdivided into different topologies, listed in Table 2.3 for the initial period at low luminosity.

Trigger	Threshold [GeV]	Expected Rate [Hz]	Cumulative Rate [Hz]
Inclusive e	29	33	33
ee	17	1	34
Inclusive γ	80	4	38
$\gamma\gamma$	$40 \otimes 25$	5	43
Inclusive μ	19	25	68
$\mu\mu$	7	4	72
Inclusive $\tau-$jets	86	3	75
Two $\tau-$jets	59	1	76
1 jet and $\not\!\!E_T$	$180 \otimes 123$	5	81
1 jet or 3 jet or 4 jet	657,247,113	9	89
e and jet	$19 \otimes 52$	1	90
Inclusive b-jets	237	5	95
Calibration and other events		10	105
Total			105

Table 2.3: High-Level trigger table at low luminosity. The thresholds correspond to the values of E_T or p_T with 95% efficiency (90% efficiency for muons).

2.3 The electromagnetic calorimeter

An homogeneous calorimeter has been chosen. The ECAL consists of almost 76000 Lead Tungstate $PbWO_4$ scintillating crystals divided into a barrel (EB) and two endcaps (EE). A three dimensional view of the calorimeter is given in Figure 2.11.
The design of CMS ECAL has been prompted by the possibility to observe the decay of a light Higgs boson into a pair of photons. Since in the region $m_H < 140$ GeV/c^2 the intrinsic Higgs width (Γ_H) is less than 30 MeV, the $\gamma\gamma$ invariant mass resolution is dominated by the experimental resolution, which should be of the order of 1% to enhance the significance of a possible signal.
In the following a detailed description of the ECAL and its performances are given.

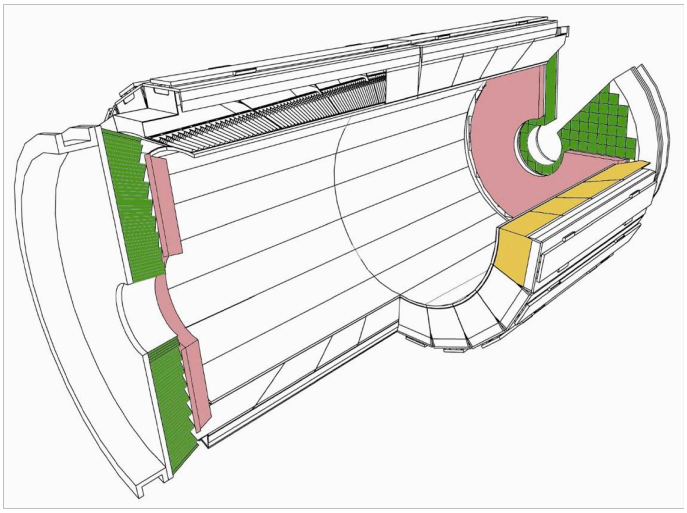

Figure 2.11: Three dimensional view of the electromagnetic calorimeter.

2.3.1 Layout and geometry

The barrel part of the ECAL covers the pseudorapidity range $|\eta| < 1.479$. The barrel granularity is 360-fold in ϕ and (2×85)-fold in η, resulting in a total of 61 200 crystals. The truncated-pyramid shaped crystals are mounted in a quasi-projective geometry so that their axes make a 3° angle with respect to the vector from the nominal interaction vertex, in both the ϕ and η projections. The crystal cross-section corresponds to approximately $0.0174 \times 0.0174°$ in η-ϕ or 22×22 mm^2 at the front face of crystal, and 26×26 mm^2 at the rear face. The crystal

length is 230 mm corresponding to 25.8 X_0.
The crystals are contained in a thin-walled glass-fibre alveola structures (submodules) with 5 pairs of crystals (left and right reflections of a single shape) per submodule. The η extent of the submodule corresponds to a trigger tower. To reduce the number of different type of crystals, all crystals in each submodule have the same shape. There are 17 pairs of shapes. The submodules are assembled into modules and there are 4 modules in each supermodule separated by aluminium webs. The arrangement of the 4 modules in a supermodule can be seen in the photograph shown in Figure 2.12. The crystals front faces in the supermodules are at a transverse radius of 1.29 m.
The endcaps cover the rapidity range $1.479 < |\eta| < 3.0$. The distance along the beam axis between the interaction point and the endcap envelop is 3144 mm. This figure takes into account the estimated shift toward the interaction point by 2.6 cm when the 4 T magnetic field is switched on. The endcap consists of identically shaped crystals grouped in mechanical units of 5×5 crystals (supercrystals, or SCs) consisting of a carbon-fibre alveola structure. Each endcap is divided into 2 halves, or "Dees". Each Dee comprises 3662 crystals. These are contained in 138 standard SCs and 18 special partial supercrystals on the inner and outer circumference. The crystals and SCs are arranged in a rectangular x-y grid, with the crystals pointing at a focus 1300 mm beyond the interaction point, so that the off-pointing angle varies with η. The crystals have a rear face cross section of $30\times30\,\mathrm{mm}^2$, a front face cross section of $28.62\times28.62\,\mathrm{mm}^2$ and a length of 220 mm (24.7 X_0).

2.3.2 Lead tungstate crystals

Lead Tungstate crystals ($PbWO_4$) are produced for CMS by the Bogoroditsk Techno-Chemical Plant in Russia (BTCP and APATITY crystals) and by the Shanghai Institute of Ceramics in China (SIC crystals). The high density ($8.3\,\mathrm{g/cm}^3$), short radiation length (0.89 cm) and small Molière radius (2.2 cm) results in a fine granularity and a compact calorimeter. The scintillation decay time is of the same order of magnitude as the LHC bunch crossing time: about 80% of the light is emitted in 25 ns. The light output is relatively low: about 4.5 photoelectrons per MeV are collected in both the avalanche photodiodes (APDs) and the vacuum phototriodes (VPTs), where the higher APD quantum efficiency is balanced by their smaller surface coverage on the back face of the crystal. The crystals emit blue-green scintillation light with a broad maximum at 420 nm [43]. The light output variation with temperature of -1.9% per °C at 18°C requires a cooling system capable of extracting the heat dissipated by the readout elec-

Figure 2.12: Photograph of a supermodule, showing modules.

tronics and of keeping the crystal temperature stable within ±0.05°C in order to preserve the energy resolution. To exploit the total internal reflection for optimum light collection on the photodetector, the crystals are polished after machining. This is done on all but one side for EB crystals. For fully polished crystals, the truncated pyramidal shape makes the light collection non-uniform along the crystal length, and the needed uniformity [44] is achieved by depolishing one lateral face. In the EE, the light collection is naturally more uniform because the crystal geometry is nearly parallelepipedic, and just a mild tuning is being considered.

The crystals have to withstand the radiation levels and particle fluxes anticipated throughout the duration of the experiment. Ionizing radiation produces absorption bands through the formation of colour centres due to oxygen vacancies and impurities in the lattice. The practical consequence is a wavelength-dependent loss of light transmission without changes to the scintillation mechanism, a damage which can be tracked and corrected for by monitoring the optical transparency with injected laser light. The damage reaches a dose-rate dependent equilibrium level which results from a balance between damage and recovery at 18°C [45]. To ensure an adequate performance throughout LHC operation, the crystals are required to exhibit radiation hardness properties quantified as an induced light attenuation length always greater than three times the crystal length even when the damage is saturated.

2.3.3 Photodetectors

The low light yield of the $PbWO_4$ makes the use of photodetectors with an intrinsic gain necessary. At the same time, the photodetectors for ECAL have to be radiation hard, fast and able to operate in the strong CMS magnetic field. The devices which best match these characteristics and that have been chosen for the electromagnetic calorimeter are the Avalanche PhotoDiodes (APDs) for the barrel and the Vacuum PhotoTriodes (VPTs) for the endcaps.
The APDs are silicon detectors with a reverse structure (i.e., with the bulk n-type silicon behind the p-n junction see Figure 2.13) specially developed for the CMS ECAL. Each APD has an active area of $5{\times}5\,mm^2$ and two are glued to the back of each crystal. The APDs are sorted according to their operating voltage into bins 5 V wide, and then paired such that each pair has a mean gain of 50. The APDs have an high quantum efficiency (∼75% at 430 nm) which well matches the emission spectrum of the $PbWO_4$. The APDs temperature sensitivity of the gain (1/M·dM/dT) is $-2.4 \pm 0.2\%/°C$ and their voltage sensitivity of the gain (1/M·dM/dV) is $3.1 \pm 0.1\%/V$.

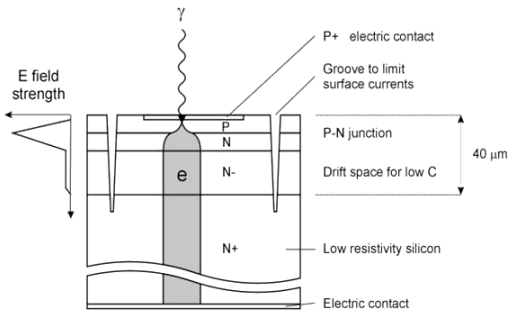

Figure 2.13: Scheme of an Avalanche Photo Diode.

The VPTs are phototubes with a bi-alkali photocathode deposited on a glass window. The electrons emitted from the cathode are accelerated towards a 10 μm thick anode; the fraction of them passing the anode grid impacts on a reflectivedy node with a planar geometry and then emits new electrons (∼ 20 secondary electrons are emitted for each impinging electron), which are accelerated back toward the anode.
The VPT quantum efficiency is about 15% at the peak of the $PbWO_4$ emission spectrum, but since the active area is almost 300 mm^2 the total light collection is at the same level as for the APDs. The VPTs operate at gain around 8-10 which is much lower with respect to the one of the APDs but which presents very little dependence on the temperature and on the biasing voltage.

2.3.4 Readout electronics

The front-end (FE) electronics has to be fast to match the LHC crossing rate and it must keep the standard deviation of the electronic noise level below ∼50 MeV per crystal over a dynamic range of about 95 dB. Finally, it is placed on the detector, so it has to be radiation hard. The electronics layout mirrors the trigger structure and its basic element is a group of 5×5 crystals called trigger tower. The signals coming from each photodetector are sent to a motherboard which hosts 5 Very Front End cards (VFE) and a Low Voltage Regulator card (LVR) providing the power for the VFE cards. The output of the 5 VFEs is fed into a FE card which processes the digitised data of one trigger tower. Each VFE card houses 5 identical channels, where the signal from the photodetector is amplified, shaped and then digitized by a 12-bit sampling ADC working at 40 MHz.
The electronic devices employ the radiation tolerant 0.25 μm CMOS technology. Each channel of the VFE cards consists of a Multi Gain Pre-Amplifier MGPA, an ADC and a buffer. The MGPA provides three outputs at three different gains, which are digitized in parallel by a four channel 12-bit ADC working at 40 MHz with an integrated digital gain switching logic. In addition, each VFE card has a Detector Control Unit (DCU) which measures the crystal temperature and the APD leakage currents.
One chip for the L1 Trigger primitive generation (the *FENIX ASIC*) is put on each trigger tower to store the data until the Level-1 response. Trigger data are transmitted to the off-detector electronics through a serial link which operates at 800 Mb/s. In case of a L1 accept, the data from the triggered events which are stored in the FENIX chip are transmitted to the off-line electronics through a separate serial data link also working at 800 Mb/s.
Further details on the front-end electronics can be found in Refs. [46][47].

2.3.5 The cooling system

The ECAL cooling system [48] employs a water flux to thermalize the detector at at ±0.05°C. An aluminum grid separates the crystals from the front-end electronics. The water reaching the supermodule is first split in parallel streams which run inside the grid, then it is collected by the grid return pipes and it is distributed to a set of aluminum cooling bars. These are connected in parallel and absorb the heat dissipated by the electronic cards which are thermally coupled to the bars by means a gap pad and gap filler (see Figure 2.14). The water flowing in the cooling circuit is thermalized at the level of ±0.01°C.

Figure 2.14: Picture of the grid. The connectors are visible, each of them hold 10 channels.

2.3.6 The laser monitoring system

Two laser wavelengths are used as basic source in the final version of the laser monitoring system. The first one at λ=440 nm, very close to the scintillation emission peak, is used to follow changes in crystal transparency due to radiation (blue line). The second one at λ=796 nm, far from the emission peak and hence very little affected by changes in transparency, is used to check the stability of the monitoring system (infrared line). The lasers are operated such that the full width at half maximum of the pulses is about 30 ns. The lasers can be pulsed at a rate of 80 Hz, and the pulse timing jitter is smaller than 3 ns to allow adequate trigger synchronization with the LHC clock train and the ECAL ADC clock.
The pulse energy of 1 mJ for the blue line corresponds to an energy of about 1.3 TeV, a linear attenuator allows steps down in energy to 13 GeV. The pulse intensity stability is guaranteed at the 10% level.
There are three light sources, two blue and one infrared. The duplication of the blue source provides fault tolerance and allows maintenance, ensuring availability of a source at the wavelength used to track changes in transparency. Each source consists of an Nd:YLF laser pumping a tunable Ti:Sapphire laser. Further details can be found in [49].
The monitoring light pulses are distributed via a system of optical fibres. A fibre optic switch at the laser directs the laser pulses to 1 among the 88 calorimeter regions. A two-stage distribution system mounted on each calorimeter region finally delivers the light to each crystal.
The fluctuations of the laser pulse are monitored via the PN silicon phodiodes, However reasonable stability of the pulse height is desirable to avoid effect of non linearities between the monitoring PNs and the APDs readout chain.

The ageing of the laser pump can reduce the pulse height. This can be compensated for by increasing the current in the pump lamp and replacing it periodically, as it will be shown in Section 3.3.2.

2.3.7 Detector performances

Amplitude reconstruction

The raw data for a single channel consists of a serie of consecutive samples of the analog signal making up a time frame. The signal from the APDs is at 40 MHz and 10 samples are recorded, including 3 samples before the signal rise in order to estimate the baseline.
In the test beam there is no synchronization between the clock and the trigger from the scintillators. Therefore the time of the samples with respect to the start of the pulse varies from an event to another. The time difference between the clock and the start of the pulse is measured by a TDC and this information allows an oversampling of the typical pulse shape, by averaging many events, once the proper time offset is taken into account. At LHC the timing of the signal will be adjusted so that the signal pulse maximum corresponds to one of the samples.
The simplest method to reconstruct the amplitude is to use the sample at the signal maximum. However, one of the reasons for reading out a larger number of samples is to reduce the noise contribution by using more sophisticated methods. Two different algorithms have been developed for the amplitude reconstruction. A first method, called analytic fit, consists in fitting the samples by a function that is derived from the readout electronics transfer function:

$$f(t) \;=\; A\left(\frac{t}{t_{peak}-t_{offset}}\right)^{\alpha} exp\left(-\alpha\frac{(t-t_{offset})-t_{peak}}{t_{peak}}\right), \qquad (2.4)$$

where A is the signal amplitude, t_{peak} is the time of the peak of the pulse shape, t_{offset} is the time offset between the start of the pulse and the first sample and α controls the rising shape (Figure 2.15) The average pulse shape of a run is fitted by the function 2.4 to obtain the proper value for α and t_{peak} for each crystal. For each event the signal amplitude is then computed by fitting only five samples (starting from one sample before the maximum and ending three samples after), fixing the parameters obtained on a crystal by crystal basis for the run. The fit is performed after subtracting the pedestal calculated as the mean of the pedestal of the previous 25 events.
The second method to obtain the signal amplitude is the weights method. The signal amplitude A is here computed as a linear combination of discrete time

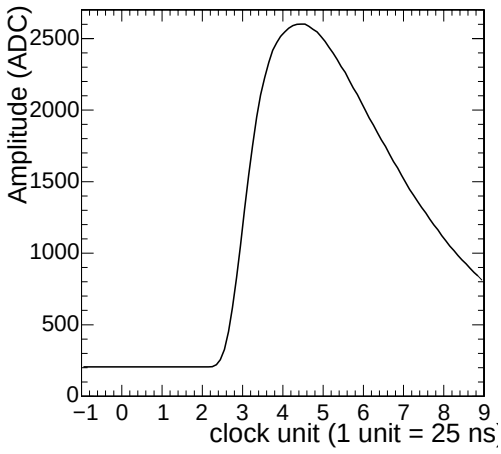

Figure 2.15: Profile of the signal pulse from a crystal using an electron beam of 120 GeV.

samples (S_i):

$$A = \sum_i S_i w_i \ . \tag{2.5}$$

The weight w_i are determined by minimizing the variance of A, with the additional requirement $\Sigma w_i = 0$ applied. Details of the mathematics of the optimization procedure can be found in [50].

Energy resolution

The energy resolution is parameterized as a function of energy:

$$\left(\frac{\sigma}{E}\right)^2 = \left(\frac{S}{\sqrt{E}}\right)^2 + \left(\frac{N}{E}\right)^2 + C^2, \tag{2.6}$$

where S is called the stochastic term, N the noise term and C the constant term. Different effects contribute to each term in Equation (2.6). The overall parametrization as well as the relative contributions are shown in Figure 2.16, the data points are measured during an ECAL test beam.
The stochastic term mainly includes the contribution of the fluctuations in the number of electrons which are produced and collected. Since these fluctuations are poissonian, this contribution goes like $\frac{1}{\sqrt{n_{pe}}}$, where n_{pe} is the number of photoelectrons emitted per energy unit. Contributions come from the light yield of the crystals, from the efficiency in the light collection and from the quantum efficiency of the photodetectors. Important contributions also come from the fluctuations in the multiplication process inside the photodetectors.

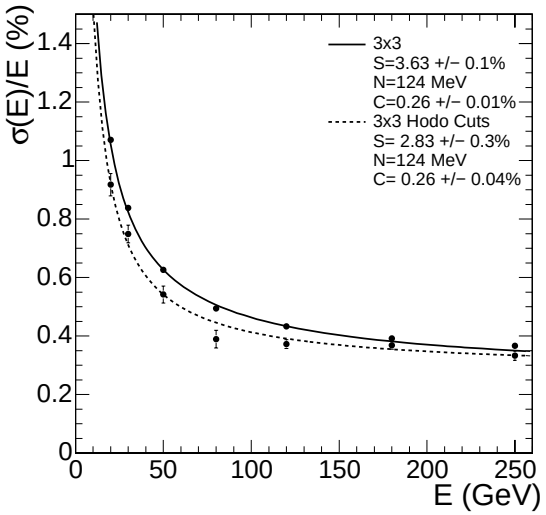

Figure 2.16: ECAL supermodule energy resolution, σ_E/E, as a function of electron energy as measured from a test beam. The upper series of points correspond to events taken with a 20×20 mm^2 trigger and reconstructed using a containment correction. The lower series of points correspond to events selected to fall within a 4×4 mm^2 region. The energy was measured in an array of 3×3 crystals with electrons impacting the central crystal.

The noise term includes contributions from the electronic noise, due to both the photodetector and the preamplifier, and from pile-up events. These contributions vary as a function of the pseudorapidity and of the luminosity of the machine.
The constant term is the dominating term above 50 GeV and parametrizes different contributions. Among them, the most important are:

- the stability of the operating conditions, such as the temperature and the photodetector high voltage.
- the presence of dead materials between the crystals and the rear of the electromagnetic shower.
- the longitudinal non uniformity of the crystal light yield. A light focusing effect of the light takes place due to the shape of the crystals and to the high refractive index, so that the light collection is not uniform.
- the crystal-to-crystal intercalibration errors. Since a typical electromagnetic shower is not entirely contained inside a single crystal, the relative crystal calibration could introduce systematic errors on the energy measurement.

- the radiation damage of the crystals, which induces their response to a certain amount of deposited energy and resolution is affected because of the shower longitudinal fluctuations.

The details of the crystals' calibration and of the radiation damage corrections are presented in Chapter 3.
In Table 2.4 the design goal for the different contributions to the energy resolution is reported, estimating the energy with a 5×5 crystal matrix.

Contribution	Barrel ($\eta = 0$)	Endcap ($\eta = 2$)
Stochastic term	$2.7\%/\sqrt{E}$	$5.7\%/\sqrt{E}$
Shower containment	$1.5\%/\sqrt{E}$	$1.5\%/\sqrt{E}$
Photostatistic	$2.3\%/\sqrt{E}$	$2.3\%/\sqrt{E}$
Preshower sampling	-	$5\%/\sqrt{E}$
Noise term	155(210) MeV	770(915) MeV
Preamplifier low(high) $\mathcal{L}$	150(150) MeV	750(750) MeV
Leakage current low(high) $\mathcal{L}$	30(110) MeV	-
Pileup low(high) $\mathcal{L}$	30(95) MeV	175(525) MeV
Constant term	0.55%	0.55%
Shower containment	$< 0.2\%$	$< 0.2\%$
Longitudinal non uniformities	0.3%	0.3%
Calibration	0.4%	0.4%

Table 2.4: Contribution to the energy resolution in the barrel and in the endcap for an array of 5×5 crystals. The values reported are the designed goal for the calorimeter.

2.4 Summary

In this chapter the Large Hadron Collider (LHC) has been introduced. The CMS detector and its subsystems have been described focusing on the electromagnetic calorimeter (ECAL).
The LHC is the new particle accelerator under construction at CERN which will collide protons at the centre of mass energy $\sqrt{s} = 14$ TeV with a design luminosity of $10^{34}\text{cm}^{-2}\text{s}^{-1}$. Once in operation, it will allow to explore New Physics at the TeV scale. Its physics programme includes investigations of the electroweak symmetry breaking, searching for new phenomena and detailed Standard Model studies. At four interaction regions along the LHC ring, the protons bunches collide against each other, Around these, four experiments are being constructed, among which the Compact Muon Solenoid (CMS).

CMS is a general purpose 4π detector, featuring a large solenoidal magnet producing a strong 4T field, a highly performant muon system, a full silicon inner tracking system, a crystal electromagnetic calorimeter and an hermetic hadron calorimeter.
The CMS electromagnetic calorimeter (ECAL) consists of almost 76000 Lead Tungstate $PbWO_4$ scintillating crystals for the accurate measurement of electrons and photons. $PbWO_4$ is chosen because of its short radiation length, fast scintillation process and intrinsic radiation hardness. The light yield and the photodetector response sensitivity to temperature require a cooling system. A laser monitoring will be used to control the response variation due to irradiation. An excellent energy resolution has been demonstrated in the testbeam, of better than 1% for energy greater than 100 GeV.

Chapter 3

Crystal energy response

As it has been described in the previous chapter, the ECAL $PbWO_4$ crystals predict excellent intrinsic resolution. In order to preserve such performance for the energy measurements of electromagnetic particle, and in particular electrons, a precise calibration is needed. In particular a channel-to-channel relative calibration, thereafter referred to as intercalibration, is necessary to keep the constant term of the energy resolution below 0.5%, requiring a detailed understanding of the single crystal energy response.
Before the installation in CMS, the ECAL channels will be intercalibrated using electron beams in a test beam, cosmic rays and laboratory measurements, to have an initial set of coefficients at startup. Morover, since the radiation damage affects the transparency of the crystals, the response of each channel will be constantly monitored with a monitoring system based on the injection of laser light.
The ECAL intercalibration procedure is described in Section 3.1. In the next section (Section 3.2), results from testbeam precalibration and the first cosmic data are presented and compared. The radiation damage, the concept of the laser monitoring and the results of an irradiation test are presented in Section 3.3.

3.1 Intercalibration procedure

Many small effects which are negligible at relatively low precision need to be treated with care as a level of precision of few per mil is envisaged. The essential issue is the stability in both time and space, so that showers in different locations in the ECAL, with data recorded at different times are accurately related to each other.
The main source of channel-to-channel response variation in the barrel is the crystal-to-crystal variation of the scintillation light yield whose distribution has

a standard deviation of about 8%.
Prior to installation in CMS, it is foreseen that at least some supermodules will be precalibrated in an electron beam at CERN. This will provide an initial set of crystal calibration coefficients at startup. Due to time constraints, only few supermodules will be pre-calibrated in this way, alternative strategies have been suggested to provide initial coefficients for the remaining crystals. The estimate of the intercalibration precision which can be reached using such alternative methods is necessary.
The first used strategy exploits the laboratory measurements performed during the assembly phase that all the crystals have to undergo before being accepted for ECAL. Such measurements aim at determining with the highest possible precision the optical properties of the crystals and the gain of the electronics for each crystal. The light yield is obtained by measuring the photopeak position in the scintillation energy spectrum of a ^{60}Co source [51].
Another strategy to pre-calibrate the full detector is the use of cosmic rays. The idea consists in preparing a comics telescope and in selecting only those events in which the muon traverses the crystal along the direction parallel to its axis. This can be done by choosing only the events where one single crystal presents a significative signal by vetoing in the neighboring crystals, with the help of external scintillators working as a trigger.
Finally, the radiation damage reduces the transparency of the crystals. Since the effect is different from crystal to crystal, this affects the system calibration and it is therefore necessary to correct for it. To cope with this effect, a laser monitoring system is used to follow the time evolution of each channel response.

3.2 Intercalibration at start-up

Preliminary estimates of the intercalibration coefficients (c_i) are obtained from test beam precalibration of some supermodules (c_i^{TB}), laboratory measurements of crystal light yield (c_i^{Lab}) and the commissioning of further supermodules with cosmic rays (c_i^{Co}).

3.2.1 Laboratory measurements

The calorimeter is being assembled in 2 regional centres: at CERN and at INFN-ENEA Casaccia near Roma. During the assembly phase, all the detector components are characterized [53],[54] and the data are saved in the construction database. It is thus possible to predict the calibration c_i^{Lab} of each channel i

using the laboratory measurements as

$$\frac{1}{c_i^{Lab}} \propto \mathrm{LY}_i \cdot \varepsilon_i \cdot c_i^{ele} \cdot \mathrm{M_i}, \tag{3.1}$$

where LY_i is the crystal light yield, M_i and ε_i are respectively the gain and quantum efficiency of the photo-detector and c_i^{ele} is the calibration of the electronics chain. The crystal LY is measured in the laboratory with a photo-multiplier tube (PMT), exciting the crystal with a ^{60}Co source. This gives an average $\mathrm{LY_{PMT}}$ for the $PbWO_4$ crystals of about 10 pe/MeV at 18°C.
It is a delicate and difficult measurement because the $PbWO_4$ crystals have a rather low LY and the energy of the ^{60}Co γ is only 1.2 MeV. Due to the different fraction of the crystal rear face covered by the PMT with respect to the VPT or APD and to the different quantum efficiency, different values are measured in equipped ECAL: about 4.5 pe/MeV for the barrel channels read out with APDs and a similar number for the endcap channels read out by VPTs because the larger surface area of the VPT photocathodes balances the higher quantum efficiency of the APDs.
The measurements span about 7 years of crystal production, so that the stability of the LY bench calibration is crucial and is constantly controlled using reference crystals. The LY measurement of each crystal is rescaled using daily reference crystal measurements [55].
The laboratory LY measurement can be improved exploiting the correlation between the crystal LY and the Longitudinal Transmission at 360 nm ($\mathrm{LTO_{360}}$).

3.2.2 The test beam precalibration

The setup

In 2004, extensive measurements have been carried in the H4 test beam facility at CERN. The facility consists of a secondary beam line capable to supply electron beams with a narrow momentum spectrum (between 20 and 250 GeV/c) and high rates (> 2000 electrons per burst).
Between October and November 2004 one totally equipped supermodule (SM10) was tested. The ECAL supermodule was installed on the H4 beam line on a movable table. The table could rotate in the horizontal and vertical planes, thus allowing the electron beam to be directed on crystals in all parts of the supermodule. It also allows the beam electrons to be set incident to reproduce the final geometry configuration. The transverse impact position of the beam electrons is determined by four planes of scintillating fibre hodoscopes located upstream of the movable table (see Figure 3.1).
Plastic scintillator counters are used to trigger the readout of the crystals. The

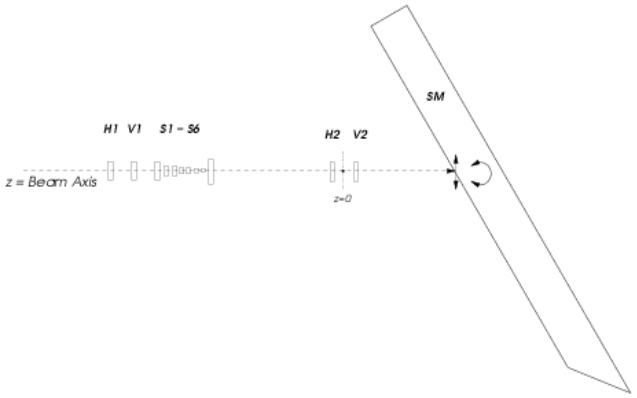

Figure 3.1: The test beam setup at H4. The four planes of scintillating fibre hodoscopes (H1, H2, V1, V2), the plastic scintillators working as triggers (S1 to S6) and the supermodule position are shown.

delay between the trigger and the digitisation clock is measured with a time-to-digital converter (TDC). The trigger defines an area of 20×20 mm^2 at the crystal front face. This area is only sligthly smaller than the transverse section of the crystals.
The main differences between the test beam setup and the data taking in the real experiment are the absence of material in front of the crystals and the absence of the magnetic field.
The supermodule was fully equipped with the final readout electronics as well as with the final cooling and temperature systems and laser monitoring system (see Section 2.3).

The intercalibration procedure

The response of a single crystal to electrons depends on the electron impact position (x,y) on the crystal front face because of the variation of the electromagnetic shower containment. Figure 3.2 shows the dependence of the response on the impact position in X and Y simultaneously ($F(x, y)$). This dependence can be factorized in the two coordinates:

$$F(x, y) = f_X(x) \cdot f_Y(y) \ , \tag{3.2}$$

where $f_X(x)$ and $f_Y(y)$ functions are well reproduced by a 4^{th} order polynomial. To better determine the polynomial in $X(Y)$ coordinate, only the events with an electron impinging in a narrow region ($\pm$ 2mm) in the $Y(X)$ are selected. The average responses of the crystal versus the impact position along the two

coordinates are fitted to determine the coefficients of the polynomials (see Figure 3.3). The dissimilarities between the two polynomials and their asymmetries with respect to the maximum are due to the difference between the crystal sizes in the X and Y directions and to the tilt of the crystals.

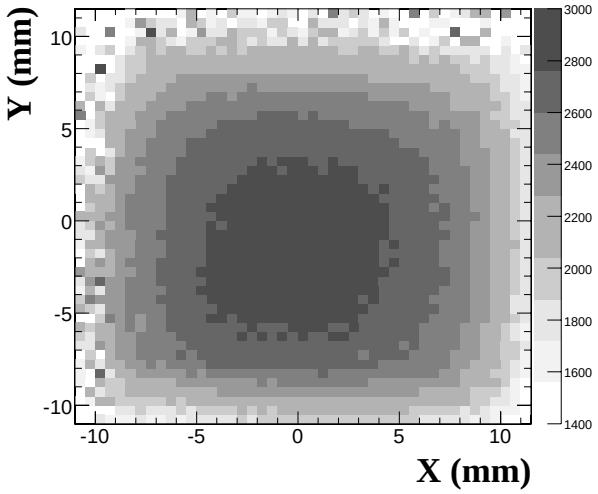

Figure 3.2: Raw crystal response (in ADC counts) versus the electron impact point in the $X \times Y$ plane. The maximum corresponds to the impact point that gives the maximum containment of the electromagnetic shower.

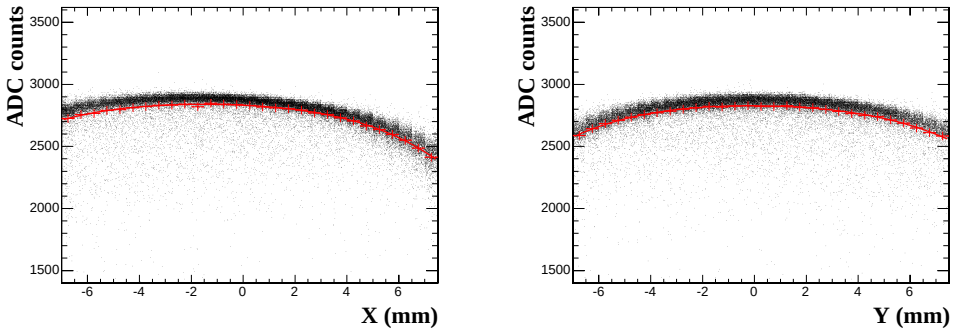

Figure 3.3: Raw crystal response (in ADC counts) versus the electron impact point for the X(left) and Y(right) coordinate. The 4^{th} order polynomial is superimposed.

The dependence of the response on the impact position has a similar behavior for all the crystals. Differences between two crystals can exist in the amplitude and in the coordinates of the maximum response.

Exploiting this similarity, two reference polynomials ($P_X^{ref}(x)$ and $P_Y^{ref}(y)$) are determined by a fit on a reference crystal. For all the others crystals the fit is performed by a polynomial $P_X(x)(P_Y(y))$, obtained from the reference one, allowing as free parameters the overall normalization factor $A_x(A_y)$ and a shift in the coordinate $x_0(y_0)$:

$$P_X(x) = A_x \cdot P_X^{ref}(x - x_0) \ , \tag{3.3}$$

$$P_Y(y) = A_y \cdot P_Y^{ref}(y - y_0) \ . \tag{3.4}$$

The choice of reference polynomials makes the whole strategy more stable, especially when working with low statistics. Local fluctuations can indeed arise and distort the polynomial shape, making a fit with many free parameters unstable. The correction, factorized in the X and Y directions, is applied event by event to obtain the corrected response (R_i^{cor}) starting from the raw measurement (R_i^{raw}):

$$R_i^{cor} = R_i^{raw} \frac{P_X^{MAX} \cdot P_Y^{MAX}}{P_X(x_i) \cdot P_Y(y_i)} \ , \tag{3.5}$$

where (x_i, y_i) are the impact points of the i^{th} event and P_X^{MAX} and P_Y^{MAX} are the maximum values which are assumed by the polynomials.
The correction works fine in removing the dependence of the crystal response on the impact position, as shown in Figure 3.4.

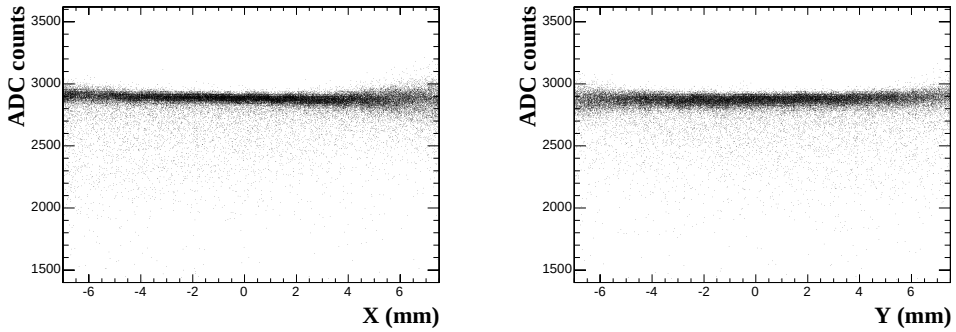

Figure 3.4: Crystal response (in ADC counts) as a function of the X(left) and Y(right) coordinate after the correction for the electron impact point on the crystal surface has been applied.

Only the events falling in a 7×7 mm^2 window around the centre have been selected for the analysis, since in the central region of the crystal surface the correction is less affected by fluctuations.
Figure 3.5 shows the distribution of the corrected energy for a crystal hit by electrons at 120 GeV. The tail on the low energy side is due to the oscillations

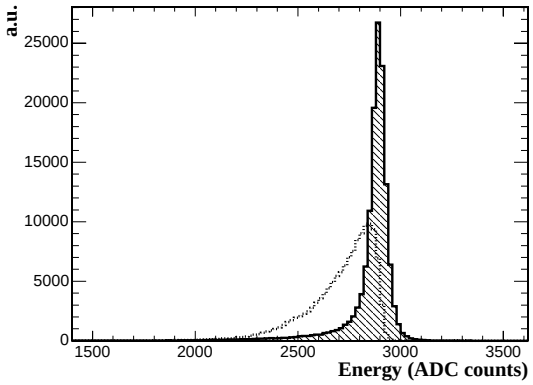

Figure 3.5: Distribution of the crystal response in ADC counts to a 120 GeV/c momentum electron beam before (dotted line) and after (solid line) the correction for the impact position.

in the shower containment. The distribution is fitted using a Gaussian plus an exponential left tail smoothly joined at 1σ from the peak, The position of the peak is chosen as the estimator of the crystal response. The test beam intercalibration coefficients (c_i^{TB}) are obtained as the response of a given channel (M_i) to the response of a reference crystal (M_{ref}):

$$c_i^{TB} = \frac{M_i}{M_{ref}} \ . \tag{3.6}$$

Intercalibration results

The intercalibration procedure has been applied to crystals of the SM10 supermodule using 120 GeV/c electrons. To optimize the data taking time with respect to the the test beam schedule, it has been chosen to collect for the many part of the channels only 2K events[1]. Due to technical reasons, four full trigger towers (composed by 5×5 crystals) and one token ring (composed by 16 trigger towers) in module 3 and module 4 could not be properly readout and were completely disconnected. Therefore only 1200 channels of the supermodule are readable. For about 10% of the channels a problem in the initialization of the DAQ system prevented from having good quality data and therefore a precise calibration.
The map of the intercalibration coefficients as a function of the crystal position in η and ϕ, is shown in Figure 3.6. As expected the coefficients are independent

[1]Dedicated studies, performed in the previous test beams, have shown that the intecalibration procedure is reliable with only 1000 events per crystal before any selection [52].

at the crystal position. The values of the two towers in module 4 has been traced down to an high voltage problem.
Figure 3.7 shows the distribution of the intercalibration coefficients obtained for the SM10 channels. The superimposed gaussian fit to the observed distribution has a standard deviation of (7.0 $\pm$ 0.2)%.

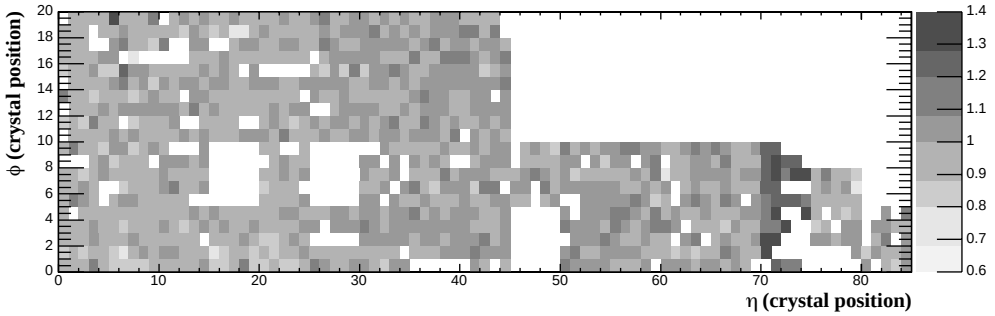

Figure 3.6: Intercalibration coefficients for the SM10 supermodule versus the crystal position.

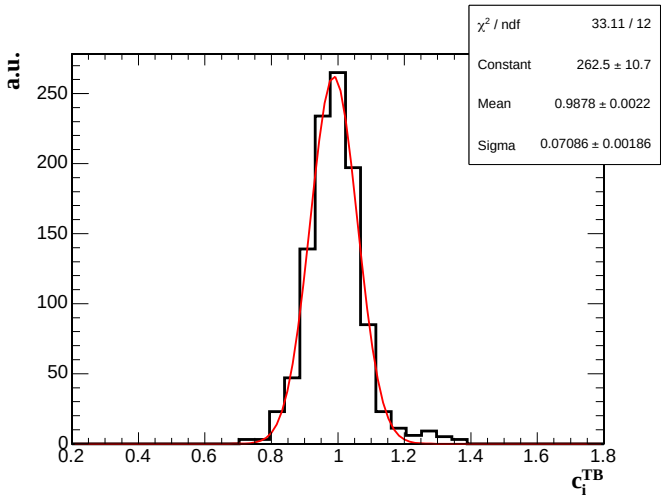

Figure 3.7: Distribution of the intercalibration coefficients obtained for the SM10 channels.

The table that moves the supermodule with respect to the beam is designed to automatically put every crystal on the beam centre. The algorithm is implemented to let 120 GeV/c momentum electron enter the crystal at the point that produces the maximum deposition of energy in the crystal, taken into account the tilt of the impinging particle with respect to the crystal axis.

The position of the beam with respect to the hodoscopes frame can be calculated by fitting the impinging position distribution to get its maximum, while the maximum of the 4^{th} order polynomial is the crystal point at which the beam is supposed to be pointing at.
Considering the beam, the comparison of the two maximum distributions is a way to measure the table alignment. In Figure 3.8 (left) the misalignments along the X and Y directions are measured by the shifts of the distributions with respect to zero. The mean misalignment as a function of the crystal type is shown in Figure 3.8 (right). Its systematic trend is related to the increase of the tilt between the crystal axis and the beam direction at higher η. Taking into account this effect in the intercalibration procedure, cutting events in a 7×7 mm^2 window around the maximum response solve problems

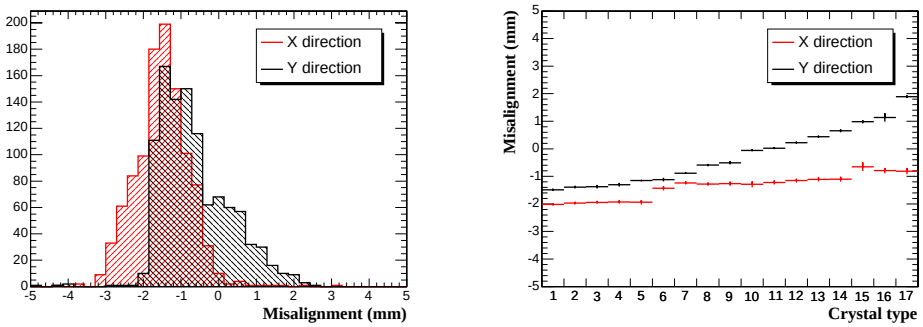

Figure 3.8: Left: distributions of misalignment along the X and Y directions. Right: the mean misalignment as a function of the crystal type. The values are in millimeters.

Test beam intercalibration coefficients can be used to measure the precision achieved by the laboratory intercalibration. Figure 3.9(a) shows the intercalibration coefficients calculated from laboratory measurements plotted against the test-beam measurements. Figure 3.9(b) shows that a resolution of about 4% is reached. CMS

Accuracy of the intercalibration procedure

The intercalibration procedure reliability can be affected by many factors both connected to the procedure itself, as the choice of the reference crystal, the choice of the polynomial for the fit, and by the calibration conditions, as the beam energy.
Dedicated studies during the 2003 test beam have shown that the choice of the reference crystal when working with a reference polynomial does not affect the

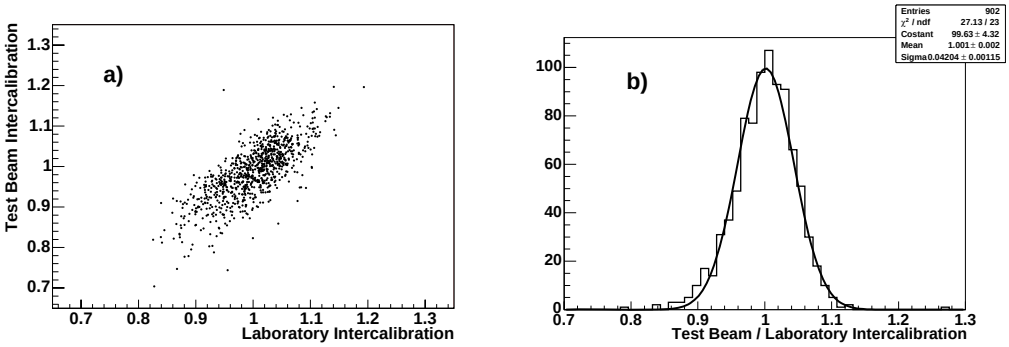

Figure 3.9: (a) Intercalibration coefficients obtained with SM10 versus intercalibration coefficients calculated from laboratory measurements and (b) distribution of the fractional difference between the laboratory estimated coefficients and coefficients measured in the test-beam.

intercalibration in a sizeable way. The agreement is at the level of 0.1% [52]. To check the ECAL linearity, the possible dependence of the intercalibration on the electron beam energy is studied. Here a comparison between the calibration coefficients computed with 120 GeV and 50 GeV electron beams is performed and the result is shown in Figure 3.10. The agreement between the two sets of coefficients is at the 0.3% level.

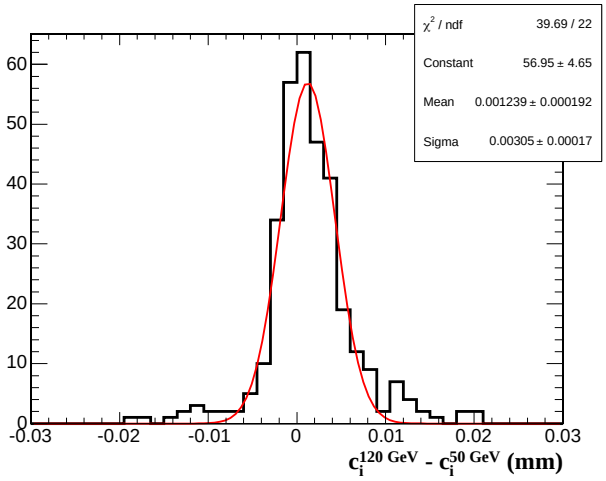

Figure 3.10: Distribution of the differences of the intercalibration coefficients calculated with electrons of different energies. The figure shows the distribution of $c_i^{120\ GeV} - c_i^{50\ GeV}$ for the SM10 crystals.

As already mentioned in the previous section, due to the tilt between the crystal

axis and the beam direction the point of maximum response differs from the geometrical centre of the crystal (see Figure 3.8), and this depends on the shower depth and therefore on the beam energy. Even if it is not directly related to the intercalibration procedure, an estimate of the accuracy in the determination of the point of maximum response can be interesting. The comparison of the results obtained from different data sets at two different beam energy (50 GeV and 120 GeV) is shown in Figure 3.11 (left). The distributions show a width of 0.77 mm for the X direction and of 0.55 mm for the Y direction and a systematic bias for both directions. The mean differences as a function of the crystal type are shown in Figure 3.11 (right), where no systematic dependences are observable.

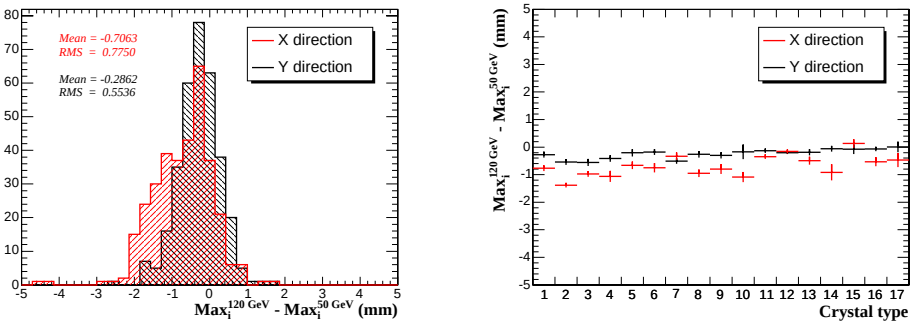

Figure 3.11: Distributions of the differences of X and Y coordinates of the point of maximum response determined in two different scans, at 120 and 50 GeV (left). Difference in function of the crystal type (right).

3.2.3 Measurements with cosmic ray muons

A new strategy to pre-calibrate the barrel supermodules is obtained by using the cosmic muons. which are well aligned with the crystals.
The method consists in using only those events which are releasing energy in a single crystal by vetoing on the neighboring channels [56]. This strategy is simple and effective, but it presents two difficulties. The first one is that the signal induced by a minimum ionizing particles, equivalent to about 11 MeV/cm in the $PbWO_4$, is comparable with the typical standard deviation level of the electronic noise (40 MeV equivalent [50]), when only a small part of the crystal is traversed. This makes the veto inefficient. The second difficulties concerns the crystal at the border of the modules, for which the efficiency of the surrounding veto would be reduced.
The first difficulty is easily overcome by increasing the multiplication voltage of the readout APDs therefore providing an increase of the gain by up to a factor

four. The second difficulty could also be overcome by using a more selective trigger, based on a set of more efficient scintillators.
The feasibility of this method was checked for the first time by measurements on a supermodule which was exposed to cosmic ray muons in November 2004, and by using a Montecarlo simulation.

Simulated cosmic ray data

Cosmic ray data in a ECAL barrel supermodule are simulated assuming the detector is exposed to muons. The energy deposition and the detector response are simulated by means of the GEANT4 package [57]. The detailed geometry of the supermodule and the framework necessary to reproduce the particle inside it are taken from a H4SIM package [58] modified version. The beam particles are replaced by a flux of muons reproducing the typical energy and angular distributions of cosmic ray data at sea level, based on experimental data [59].
To simulate the cosmic test, the supermodule is assumed to lie horizontally, with the front face of the crystals facing the ground. This orientation can be obtained by a 90° rotation with respect to the test beam position around an axis parallel to its longest side (η direction). Due to the increasing inclination of crystals along η, this position corresponds to essentially vertical crystals in module 1, while crystals in module 4 are the most difficult to calibrate because of the lower cosmic rate at large angles.
The simulation also assumed that the cosmic muons are triggered by an independent device, such as a telescope of plastic scintillators. The trigger efficiency is taken to be 100%. No external tracking device is assumed, so that the direction and energy of impinging cosmic particles, whenever needed in the analysis, are taken directly from the generated data.
The digitization of the detector response is performed according to a simplified scheme. The signal from each crystal is calculated by

$$E_j = \frac{E_{j,original} \times G}{35.6\text{MeV/ch}} \ , \tag{3.7}$$

where $E_{j,original}$ is the signal size (in MeV) provided by the H4SIM package and G is the increase (roughly a factor 4) in the APD gain obtained by modifying the APD biasing voltage. The assumed energy/(ADC counts) conversion factor is 35.6 MeV/ch.
The effect of the detector noise is also simulated by adding a gaussian smearing with a standard deviation of 40 MeV.
The analysis is based on purely calorimetric data and relies on a series of simple cuts, applied in sequence. In each event, the crystal with the highest deposited

energy is selected and the 8 surrounding crystals (i.e. the full 3×3 matrix centered around the candidate muon) are considered. The signal in the highest energy crystal (in ADC counts) is described by E_1, while the variable E_2 describes the highest signal in the 8 surrounding channels. The selection of muon candidates is based on the two variables E_1 and E_2.

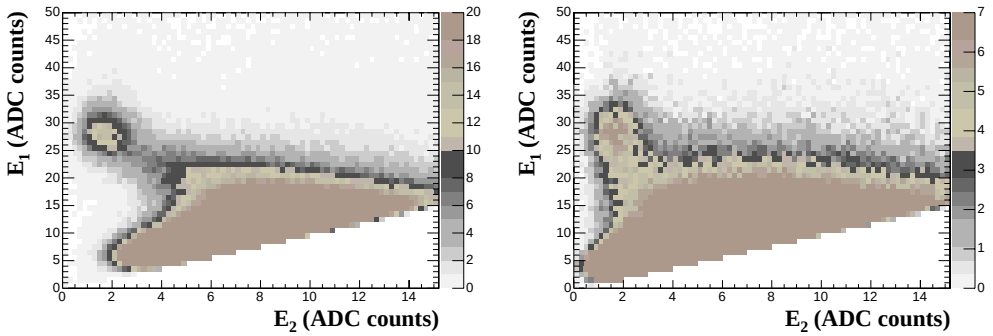

Figure 3.12: Scatter plot of E_1 vs E_2 for simulated cosmic events corresponding to one week of data taking. E_1 is the energy deposited in the crystal with the highest signal, while E_2 is the highest energy deposition in the immediately surrounding crystals. Edge crystals have been removed. Left: crystals in the module 1. Right: crystals in the module 4.

Figure 3.12 presents the scatter plots E_1 vs. E_2 for module 1 and module 4, obtained after removing edge crystals (crystals at the borders of the module or adjacent dead channels), for a simulated statistics equivalent to 7-days of data taking. The signal of well aligned muons is clearly visible as the blob at the top left corner, however, as expected, the situation is significantly worse in module 4 than in module 1, due to the smaller rate of properly aligned cosmics. To select through-going muons parallel to the crystal axes, the cuts $E_1 > 10$ ADC counts and $E_2 < 3$ ADC counts are imposed.

Real cosmic ray data

A data-taking campaign dedicated to cosmic rays was launched at the CERN north area on the ECAL supermodule SM10 for a total lifetime of about 41 hours.

As for the simulation, the gain of the APDs was increased by a factor four with respect to normal running conditions. To provide the trigger information, two plastic scintillators were positioned, respectively, above and below the supermodule, so that most of module 1 was efficiently covered. No data could be taken in the others modules. The data were collected using the H4 test beam acquisition

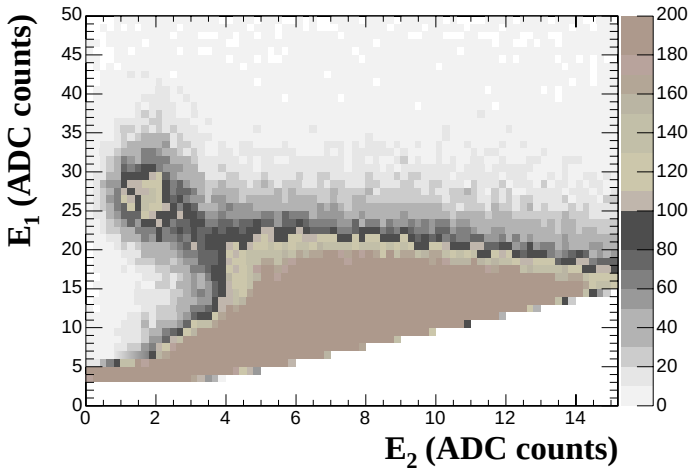

Figure 3.13: Scatter plot of E_1 vs E_2 in real cosmic ray events corresponding to 41h of data taking in the module 1. E_1 is the energy deposited in the crystal with the highest signal, while E_2 is the highest energy deposition in the immediately surrounding crystals. Edge crystals have been removed.

system. One full trigger tower (composed by 5×5 crystals) of module 1 could not be properly readout and was completely disconnected.

The real data are analyzed following the same procedure as for the simulated data. Events corresponding to muons passing through inactive regions of the detector (such as a disconnected tower) are discarded by a preselection requiring a minimum energy deposition $E_1 \geq 3$ ADC counts in at least one crystal.

Figure 3.13 shows the scatter plot E_1 vs E_2 obtained with real data. As for the simulated events, this plot does not contain particles detected at the edges of the supermodule or at the border of inactive regions, where the veto based on the calorimeter information alone is know to be inefficient. Moreover only to the region covered by the trigger scintillators is used.

The map of the preselected events, in the form of an occupancy plot as a function of the crystal position in η and ϕ is shown in Figure 3.14 (left). As expected, the occupancy distribution is hill-shaped due to the varying angular acceptance defined by trigger scintillators as a function of the muon impact point. The squared dead region corresponds to the inactive trigger tower.

As for the simulation, the final sample of cosmic muons useful for the calibration, i.e. well oriented with respect to the crystals, is selected by requiring $E_1 > 10$ ADC counts and $E_2 < 3$ ADC counts. The resulting occupancy plot as a function of the crystal position in η and ϕ is shown in Figure 3.14 (right). Here

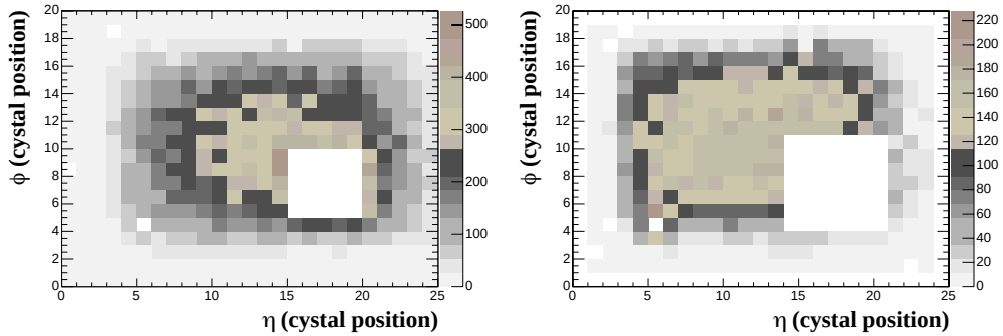

Figure 3.14: Distribution (occupancy) of the cosmic events versus the crystal position for the triggered events (left) and after the selection (right).

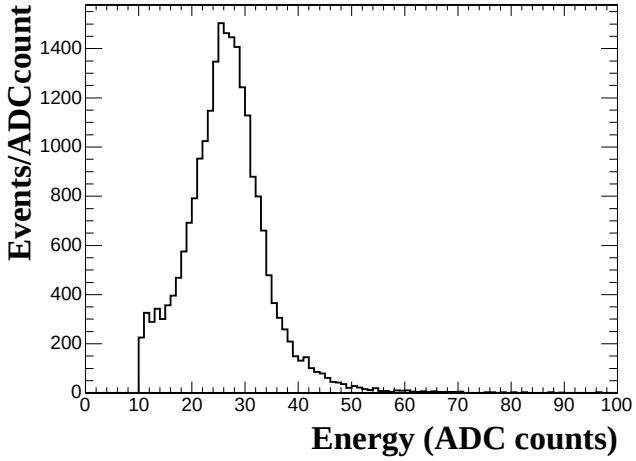

Figure 3.15: Energy deposited by real cosmic-ray data after the final selection, corresponding to 41h of data taking in the module 1. The histogram contains the data for all the channels.

the occupancy distribution is rather flat, apart from the region at the borders of the trigger scintillators due to acceptance inefficiency. The different shape with respect to Figure 3.14 (left) is an effect of the selection cuts, which, by keeping only those events parallel to the crystal axes, tends to equalize the geometrical acceptance of all the channels.
Figure 3.15 shows the E_1 distribution obtained in the final sample by superimposing the signal distribution of all channels.
The observed rate of selected cosmics in the data is 55 ± 2 per day per crystal on average, to be compared to an expectation of 61 ± 2 based on simulation. The

disagreement may be explained by some trigger inefficiency in the data and by possible inaccuracies of the cosmic rate in the simulation.

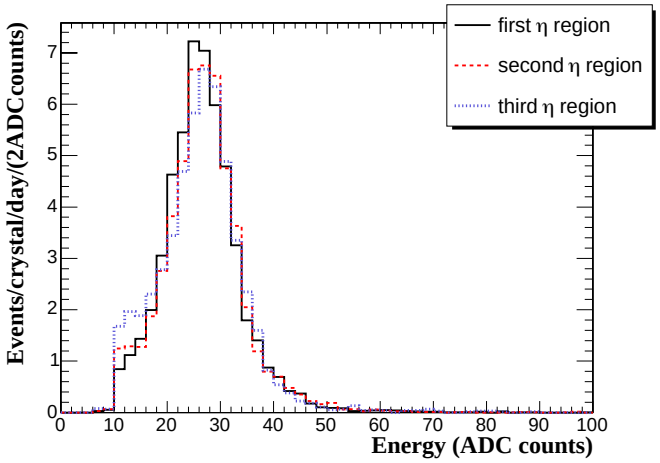

Figure 3.16: E_1 distributions observed in three η region of the module 1. The first region refers to rows 4 to 9 in η, the second region to rows 10 to 15 and the third region to rows 16 to 21. Three functions are derived from the histograms by linearly interpolating the bin contents. The curves are then fitted to the spectrum in individual channels to determine their calibration constants.

The calibration constants are extracted from a fit to the E_1 spectrum in each channel. Since the shape of the E_1 distribution is not gaussian, the peak position is obtained by fitting the data with a function that better reproduces the observed histograms. The functions are derived from the data themselves, by averaging over the spectra of the crystals belonging to three separate η region of module 1 (see Figure 3.16). Three functions are then obtained by linearly interpolating the contents of adjacent bins. The calibration constant for each channel is then extracted from a fit (through a likelihood maximization) of the observed spectrum for each of the three functions, keeping the case with the best likelihood. The overall normalization and the scale factor (F_i) are the only free parameters of the fit. The intercalibration coefficient of a given channel obtained with the measurements with cosmic rays muon (c_i^{Co}) is obtained as the scale factor response (F_i) divided by the one of a reference crystal (F_{ref}):

$$c_i^{Co} = \frac{F_i}{F_{ref}} \ . \tag{3.8}$$

Comparison between real cosmic and test beam data

In order to evaluate the precision obtainable with cosmic muons on the intercalibration coefficients (c_i^{Co}), a comparison between cosmic and test beam data is performed. Unfortunately, the test beam calibration coefficients (c_i^{TB}) are available only for a fraction of the module 1 crystals (see Section 3.2.2). Furthermore, some crystals have a particularly low statistics in the cosmic sample, due to the limited angular acceptance of the trigger. The comparison between cosmic and test beam data is thus restricted to those crystals for which the c_i^{TB} is available, which corresponds to 156 channels in total. To reduce the statistical uncertainties, a minimum of 50 good cosmic events per channel is requested which further reduces the analyzed sample to 130 crystals. These channels are characterized by an initial mis-calibration of 7% (r.m.s.), as obtained from the spread of their test beam calibrations coefficients.
The comparison between c_i^{Co} and c_i^{TB} in the 130 selected channels is shown in Figure 3.17. The gaussian fit to the observed distribution has a standard deviation of (3.1±0.3)%. The correlation between c_i^{Co} and c_i^{TB} is shown in Figure 3.18.

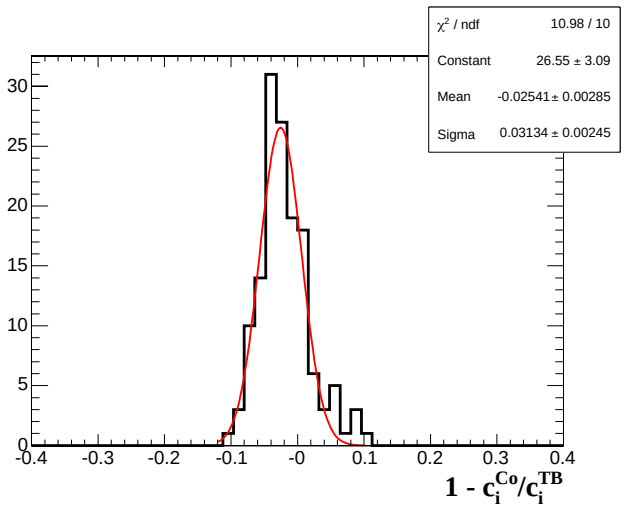

Figure 3.17: Relative precision of the cosmic calibration constants. Only those channels with more than 50 cosmic events are considered.

The statistical uncertainty affecting the cosmic calibration constants is estimated as follow. The peak of the distribution of the energy released by well aligned cosmic muons in one crystal can be approximated by a gaussian curve having a standard deviation of $15 - 20\%$, depending on the channel. Given that, on average, 95 cosmic events per channel are collected, the statistical contribution

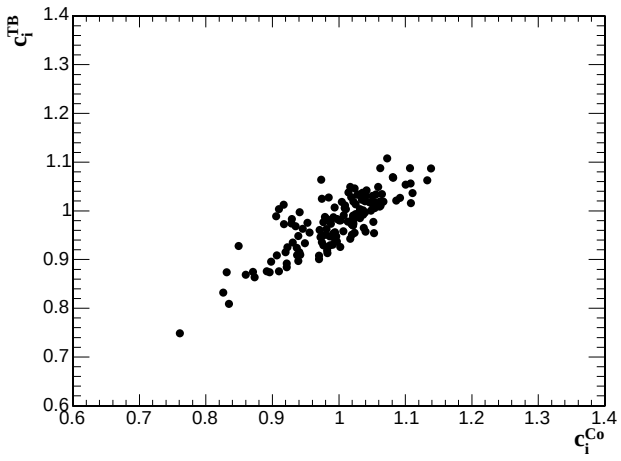

Figure 3.18: Correlation between test beam coefficients and cosmic data coefficients.

of the cosmics calibration precision can be roughly estimated to $(1.8 \pm 0.2)\%$. Statistical and systematic uncertainties associated to the test beam calibration values are assumed to be negligible.
After subtracting (in quadrature) the statistical contribution, a systematic uncertainty of $(2.6 \pm 0.3)\%$ is obtained. This result strictly applies to crystals in module 1 not belonging to edge rows. This estimate necessarily includes, among others, contributions coming from possible dis-uniformities of the electronics and from the spread introduced by the change in the APD gain.

Overall precision and setup improvements

The analysis of real cosmic events on the ECAL supermodule SM10 have shown that crystal intercalibration with cosmic rays is possible, with a relatively small uncertainty, typically of about 2.6% for crystals in module 1 not belonging to edge rows. For the rest of the supermodule simulated data can be used to estimate the achievable precision. Given the good agreement observed between real and simulated data and the simplicity of the analysis, the simulation estimate should be considered reliable.
By applying the same analysis to the simulated data in modules 2 to 4, it is possible to conclude that, for what concerns internal crystals, no dramatic deterioration of the systematic uncertainty should be expected as compared to module 1. Considering a data taking period of one week, the statistical contribution would be 0.9% in module 1, 1% in module 2, below 1.2% in module 3

(which guarantees an overall precision over 3%), but could exceed 2% at the edge of module 4. In any case, one should expect a calibration precision better than 3.5% for all internal crystals.
For edge crystals a different analysis procedure and a more refined setup are necessary to obtain the calibration constants with sufficient precision, given the inefficiency of the veto cut based on the neighboring crystals.
The statistics can only be increased by inclining the supermodule itself, possibly at an angle which maximizes the total flux of muons traversing the crystal along their longer axis. Unfortunately, constraints related to the mechanical structure of the supermodule do not permit an inclination larger than 10-20°. In the current setup the supermodules are inclined by 10°.
An additional trigger plane is used to improve the calibration of the edge crystals. This additional plane consists of several scintillators slabs, positioned above the supermodule and parallel to the module edges in order to precisely define the acceptance borders. Their signal, combined with those of the other scintillator planes, is used to tag muons that do not exit/enter from a side of the module.

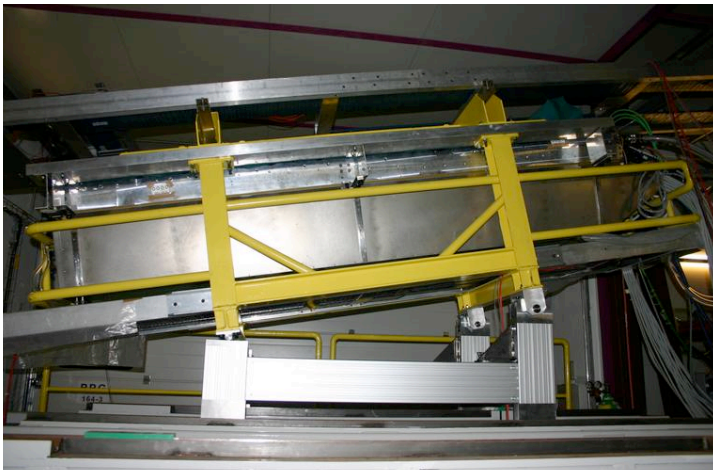

Figure 3.19: The supermodule in the current setup at H4 for the cosmic data taking.

Figure 3.19 shows a picture of a supermodule in the current setup for the cosmic data taking in the North area at CERN. Detailed studies to determine the achievable overall precision of all the channels in the four modules are on-going.

3.3 Correction for crystal transparency changes

3.3.1 Crystal behaviour under irradiation

Although radiation resistant, ECAL crystals show rapid loss of optical transmission under irradiation due to the creation of colour centers within $PbWO_4$, which absorb a fraction of the transmitted light [60]. This process is accompanied by a transmission recovery due to self annealing processes, leading to cyclical varying transparency between LHC collision runs and machine refills. The magnitude of the transparency loss is dose-rate dependent, and it is expected to range between 1% or 2% at low luminosity (10^{33} cm^{-2}s^{-1}) and in the barrel, and up to 10% in the high η regions of the endcap at high luminosity (10^{34} cm^{-2}s^{-1}). The electron energy measurement would be unacceptably degraded by these radiation induced transparency changes, were they not measured and corrected for.
The evolution of the crystal transparency is measured by the laser monitor system. Because of the different optical paths and spectra of the injected laser pulses and of the scintillation light, the change in response to the laser light is not equal to the change in response to the scintillation light. For attenuation smaller than 10% the relation between these two variations changes can be expressed by a power law:

$$\frac{S(t)}{S_0} = \Big(\frac{R(t)}{R_0}\Big)^{\alpha}, \tag{3.9}$$

where $S(t)$ and $R(t)$ are respectively the response to electrons impinging into the crystal and to the laser light at the time t, while S_0 and R_0 are the initial values. For changes larger than 10% the relation should also take into account two logarithm terms:

$$\frac{S(t)}{S_0} = \Big(\frac{R(t)}{R_0}\Big)^{\alpha}\Big[1 - \eta\, log\Big(\frac{R(t)}{R_0}\Big) + \phi\, log^2\Big(\frac{R(t)}{R_0}\Big)\Big]\ . \tag{3.10}$$

3.3.2 The irradiation test

During summer 2004, two endcap supercrystals were exposed to the H4 test beam and irradiated with 120 GeV/c electrons. They were assembled together in a module, named E0', which was installed in the H4 beam area. One supercrystal (SC03) was equipped with VPTs, the other one (SC04) was equipped with APDs and composed by only 15 crystals.
The goals of the irradiation test were:

- to check the performance of crystals coming from different batches and producers (the Russian crystals, APATITY and BTCP, and the Chinese crystals, SIC) when irradiated in conditions reproducing in the LHC environment;

- to test the procedure to correct for the change in response induced by the irradiation and to assess its accuracy.

The crystals were distributed inside both supercrystals as pictured in the Figure 3.20. The test beam period was divided into five different periods (Table 3.3.2). In the two first periods SC03 was tested while in the last three periods SC04 was put on the beam.

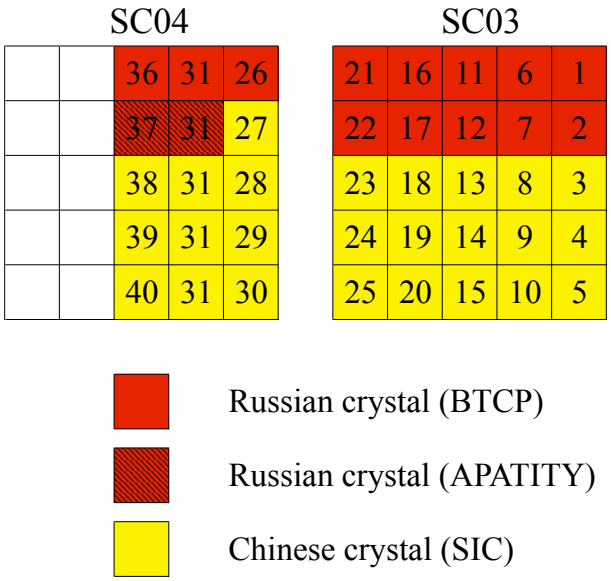

Figure 3.20: Distribution of the crystals, coming from different batches and producers, inside the two supercrystals.

Period	Date	Crystals irradiated
1^{st} (VPT)	28 May - 8 June	5 15 21 24
2^{nd} (VPT)	14 June - 21 June	3 5 12 13 15 20 21 24
3^{rd} (VPT)	27 June - 7 July	26 28 31 32* 35* 37* 39 40
4^{th} (APD)	28 July - 30 July	28 31 35
5^{th} (APD)	2 Sept. - 6 Sept.	28 31 35 39 40

Table 3.1: The date of each period and the index of the irradiated crystals. The starred crystals are irradiated two times during the same period.

The analysis presented here is focuses on the APDs periods because of rate problems on the VPTs which were understood and solved at the end of the acquisition period.

The beam intensity was modulated by a system of slits and the intensity monitored with trigger counters placed in the beamline upstream the module, recording the number of particles crossing a 20×20 mm^2 area aligned with the crystal under study. This number is directly related to the dose absorbed by the crystal, after the beam transverse dimensions and the shower profile induced by electrons are properly considered. For an 120 GeV/c electron beam and a gaussian profile with 1.5 cm standard deviation both in the X and Y coordinate, the dose at the shower maximum can be computed by the relation

$$\mathrm{Dose}_{\max}(e, 120\ \mathrm{GeV/c}) = 6.7 \times 10^{-4} \times N\ [\mathrm{Gy}]\ , \tag{3.11}$$

where N is the number of events in the trigger counter. The estimated accuracy between 10% and 20% [61].
From equations (3.9) and (3.10), it appears that the exact value of the dose is not relevant in this study, since the response to the laser beam is a direct measurement of the radiation damage occurred to the crystal. All the same, in Table 3.3.2 the irradiation doses on various crystals during the third period are reported. These rates are at the level of the ones expected in the ECAL endcap during the running at the LHC for a luminosity of 10^{34} cm^{-2}s^{-1}.

Crystal number	Crystal type	Dose (Gy)
26	BTCP	2.7
31	BTCP	4.6
32	APATITY	6.2
37	APATITY	4.6
35	SIC	5.6
40	SIC	1.6
28	SIC	4.4
39	SIC	2.9

Table 3.2: The total absorbed dose on the irradiated crystals during the third period.

3.3.3 Data treatment

The response to electrons during irradiation is obtained after applying the impact position correction described in Section 3.2.2.
It is as well necessary to define how to extract the response to the laser. The peak of the pulse amplitude distribution cannot be used directly as a measurement of the response to the laser since it presents both fluctuations from event to event and from run to run. As a consequence the spread of the distribution is of the

order of few per cents and the determination of the peak position is not precise. Reference PN diodes have been used to normalize the response of the APDs to the laser amplitude , significantly reducing both event-to-event and run-to-run fluctuations.

APDs and PNs non linearities corrections

The effects of the APD and of the PN readout electronics non linearities have to be taken into account when the APD/PN ratio is computed. A correction is applied event by event using the following formula:

$$\mathrm{PN}_{corr} = \mathrm{PN}_{raw}\Big(1 - g(\mathrm{PN}_{raw})\Big) , \tag{3.12}$$

$$\mathrm{APD}_{corr} = \frac{\mathrm{APD}_{raw}}{f(\mathrm{APD}_{raw})} , \tag{3.13}$$

where $g(x)$ and $f(x)$ are respectively a 2^{nd} and a 3^{rd} order polynomial function determined using a test pulse injected directly on the APDs and PNs readout electronics. The correction for the non linearity is below 10^{-3}.

Laser width correction

In the E0' test beam due to the ageing of the laser pump, from time to time its retuning was necessary. The retuning has caused a increase of 50% the laser pulse height and a correlated decrease of 17% of the laser width (see Figure 3.21). The pulse shapes of the APD and the PN can be described as the convolution of the laser pulse shape and of the shaping function of the respective readout systems. For the APD electronics $t_{\mathrm{rise}} \sim 50\,\mathrm{ns}$ and for the PN diode electronics $t_{\mathrm{rise}} \sim 800\,\mathrm{ns}$, so that the sensitivity to the laser pulse width is expected to be very different between the two.
In order to measure the systematics related to variations of the laser pulse width this convolution has been simulated for different laser pulse widths. As can be seen in Figure 3.22, the convolution results in a significant variation of the maximum height of the APD signal. On the contrary, the effect for the PN signal is negligible due to the long shaping time.
The correlation between the variation of the APD/PN ratio and the laser pulse width is used to correct for the ageing and the retuning of the laser. Figure 3.23 shows the used correction function, The set of points with the lowest values of the laser width are the runs after the retuning. The same function can be used for all the kinds of crystal.

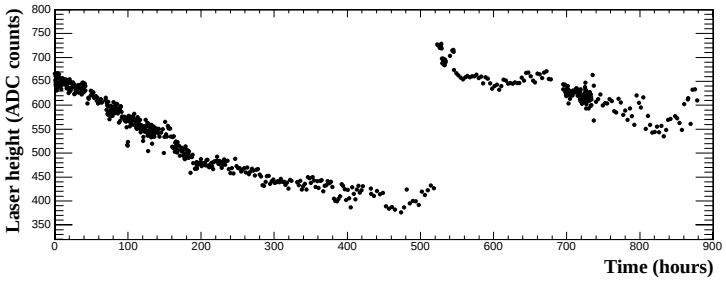

(a)

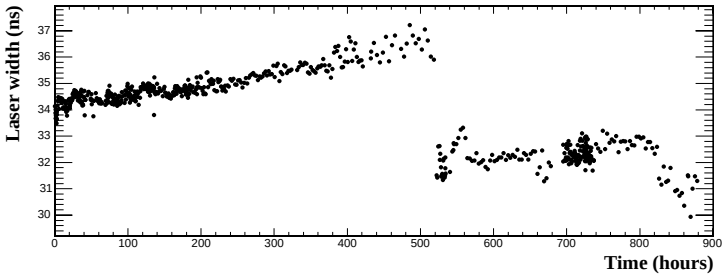

(b)

Figure 3.21: a): variation of the laser pulse height during the laser pump retuning. b): variation of the laser pulse weight during the laser pump retuning.

Temperature corrections

During the test, the temperature in H4 was not stable enough to negect the effects of temperature variations on the scintillation mechanism and the APD gain (see Section 2.3).
Different sensors were mounted in different positions to monitor the temperature during the irradiation. Two sensors (top/bottom) are put on the supercrystal cover, two sensors (A/B) on the supercrystal support plate and other sensors on the electronic cooling bars and on the black plate (see Figure 3.24(a)). The sensors are guaranteed to give a 0.2°C accuracy in the range $[0, 70]$°C, accord to specifications. In addition all the sensors are calibrated into a thermo-isolated box by recording a temperature curve in the $[15, 25]$°C range. They show a difference with respect to the nominal values less than 0.03°C in the considered range. Using the test records it is possible to correct the sensors and obtain an agreement within 0.005°C between any two or more points on the detector.
As it can be seen in Figure 3.24(b), the day-night fluctuations are changing the temperature by ± 0.05°C.
Corrections for temperature fluctuations are applied by using the formula at first

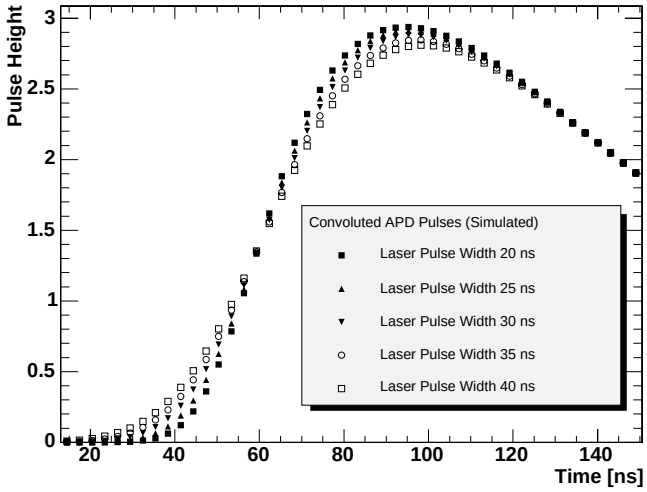

Figure 3.22: Convolutions, for the APD signal, of the preamplifier shaping and Gaussian functions simulating the laser pulse widths of 20 ns, 25 ns, 30 ns, 35 ns and 40 ns respectively. The PN diode response is stable due to the long shaping time of its readout electronic.

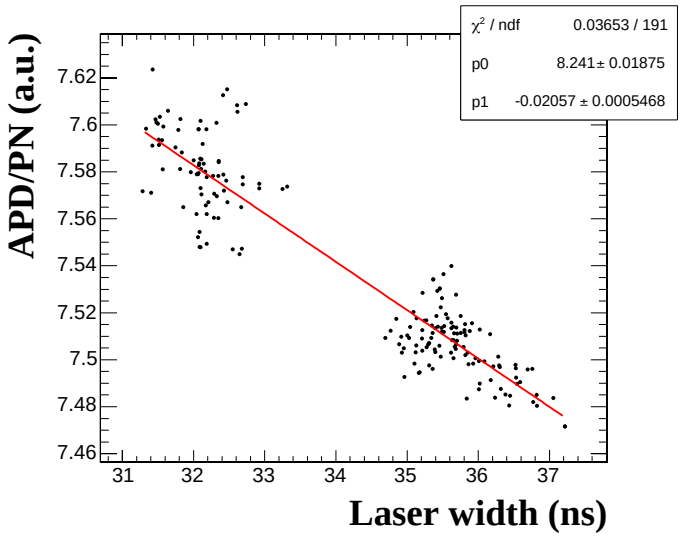

Figure 3.23: Correlation between the variation of the APD/PN ratio and the laser pulse width.

order in ΔT both for the laser (R) and for the beam (S) responses :

$$R_{corr} \quad = \quad R_{raw}(1 - \alpha_T \Delta T) \ , \tag{3.14}$$

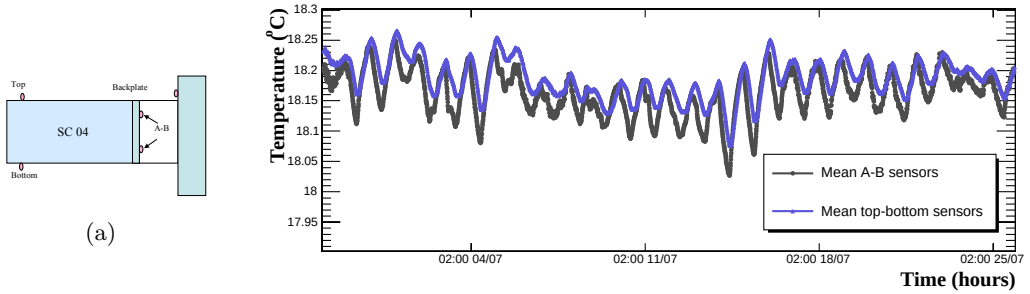

(a)

(b)

Figure 3.24: (a): position of the main temperature sensors in the supercrystal. (b): the variation the mean temperatures of the sensors A/B and of the sensors top/bottom in function of the time.

$$S_{corr} = S_{raw}(1 - \beta_T \Delta T) \ , \tag{3.15}$$

where α_T is temperature coefficient of the APD gain and β_T takes into account the dependence of both the crystal response and the APD gain. ΔT is the difference between the mean value of the temperature measured by the A/B sensors and the required working temperature of the ECAL cooling system (18°C). Both α_T and β_T are taken from previous analysis [48] giving $\alpha_T = -2\%/°\text{C}$ and $\beta_T = -3.8\%/°\text{C}$.

Results

After applying the corrections it is found that the distribution of the ratio of the laser signal measured by the APD normalized, event-by-event, to the PN response has a standard deviation on a single laser run scale of about 0.5% (see Figure 3.25(a)).
Over a period of two days the stability of the monitoring system, determined looking at the variation from run to run the mean response, is found to be within 0.1% (see Figure 3.25(b)). A similar stability was observed also in the previous test beam [62], and is well within the specifications.
In the following discussion, the energy corresponding to the peak of the distribution of the ratio APD/PN after the corrections will be called the laser response.

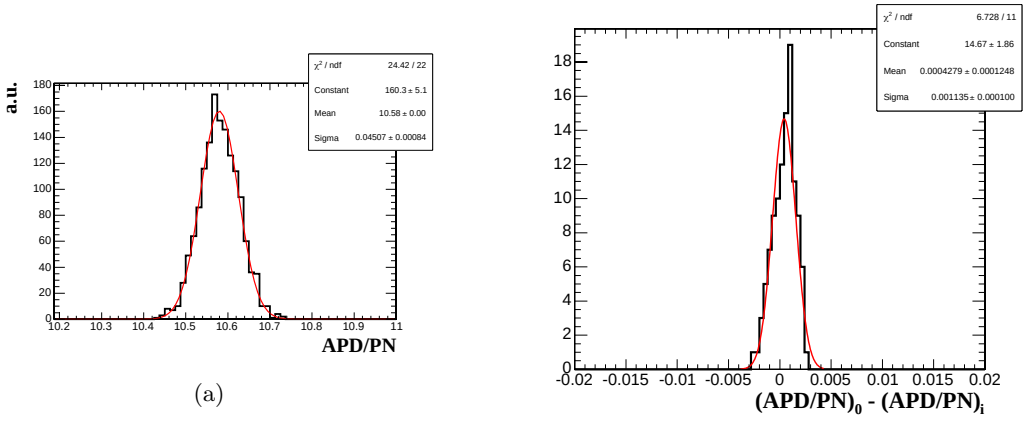

(a) (b)

Figure 3.25: a): distribution of the APD/PN ratio in a single laser run. b): stability of the monitoring system over a period of about two days.

3.3.4 Determination of the α parameter

In order to measure the coefficient of Equation 3.9, the equation is expressed using a logarithmic scale:

$$\ln S \;=\; \alpha \ln\Big(\frac{R}{R_0}\Big) + K \;, \tag{3.16}$$

where $K \;=\; \ln S_0$. According to this equation, for each irradiated crystal, the parameter α can be obtained from a linear fit of $\ln S$ as function of $\ln(\frac{R}{R_0})$. In this way, the response to electrons before irradiation (S_0) modifies only the constant parameter in the fit and does not affect the determination of α. Since the laser and the electron beam runs cannot be taken at the same time, the response to the laser R at the same dose as the response to the beam S has been determined by interpolating the results of two laser runs immediately before and after the beam run.

The uncertainties on the crystal response are evaluated *a posteriori*. The response to the laser is considered without error and the same experimental uncertainty σ_S is assumed for the response of each crystal, so that $\sigma_{\ln S} = \sigma_S/S$. An initial arbitrary value $\widetilde{\sigma}_S$ is given to σ_S determining a $\widetilde{\chi}^2$ value as the sum of the χ^2 in fit of the single crystal. The uncertainty σ_S, common to all the points, is then obtained by rescaling:

$$\beta \;=\; \sqrt{\frac{\widetilde{\chi}^2}{ndf}} \;, \tag{3.17}$$

$$\sigma_S \;=\; \beta \cdot \widetilde{\sigma}_S \;. \tag{3.18}$$

where *ndf* is the sum of degrees of freedom of the various fits. Using this procedure the uncertainty on response to the beam for each run is found to be 0.12%. A typical example of the time evolution of the irradiation measurements is given in Figure 3.26. The response to the beam and to the laser, normalized to the responses before irradiation, are given as a function of the mean dose absorbed by the crystals during an irradiation with electrons.

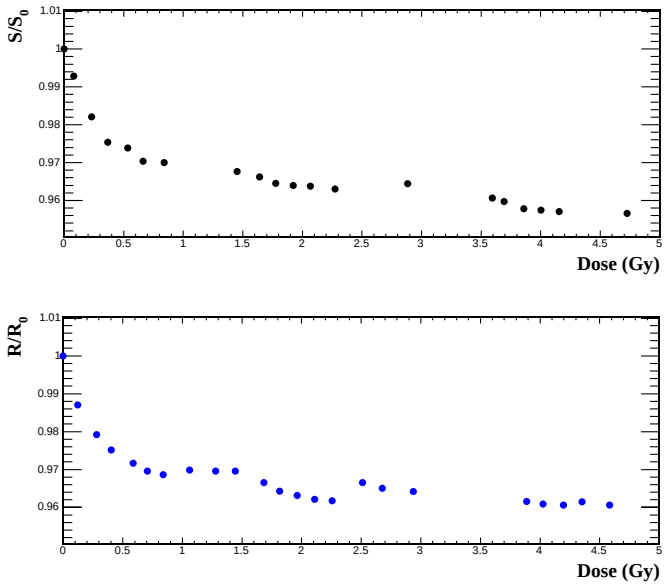

Figure 3.26: Top: relative response to the beam versus the mean absorbed dose. Bottom: relative response to blue laser versus the mean absorbed dose. The data refer to the BTCP crystal number 31 during the 3^{rd} period of data taking.

The evolution of the response to the laser as a function of time during irradiation is shown in Figure 3.27(a) for the BTCP crystal number 31 and in Figure 3.27(b) for the SIC crystal number 35. The long gap it is due to the laser repair between the 4^{th} and 5^{th} periods. For the BTCP crystal the full recovery is reached about 300 hours after the end of the irradiation while the SIC crystal does not reach a complete recovery. This different behavior is related to both the different time constant of these crystals and to the bad quality of the analyzed SIC crystals, coming from the first batch delivered to CERN. Further optimizations in the production chain have allowed to reach a good quality also for the SIC crystals.

Examples of the linear correlation between the response to electrons $\ln(S)$ and the relative response loss to the laser $\ln(R/R_0)$ is shown in Figure 3.28 for a

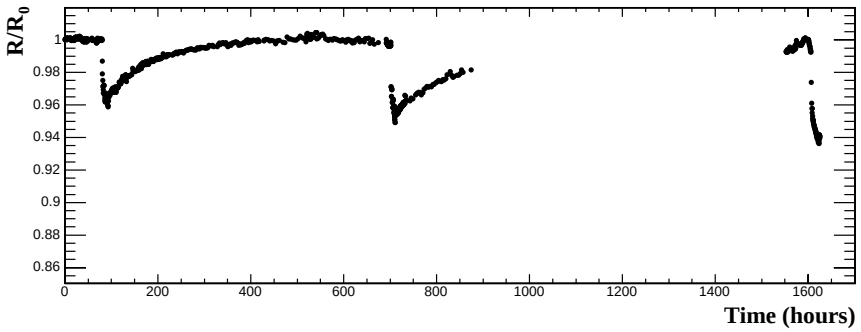

(a)

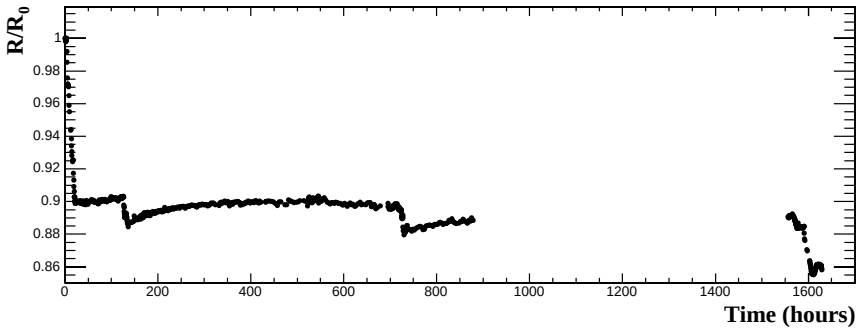

(b)

Figure 3.27: Response to the laser versus the time, both normalized to the first point. The data refer both to the BTCP crystal(a) and to the SIC crystal(b).

BTCP crystal. The linear fits to determine α are superimposed to the data. Table 3.3.4 summarizes the results obtained during the irradiation and the recovery periods. The values obtained for the various data taking periods are reported. A response loss to electromagnetic showers ranging from about 4% to 10% has been observed during an irradiation with 120 GeV/c electrons. Lower losses are observed with the laser monitoring system, which reflects in α coefficients above one. Using the data from this test, α is finally measured to be 1.26(0.99) with a relative uncertainty 5%(10%) for crystals produced by BTCP(SIC). Although the relative dispersion is larger for the SIC crystals, the absolute contribution to the systematic uncertainty is similar to the BTCP crystals (see Section 3.3.5).

3.3.5 Correction for irradiation loss

The ultimate goal of the laser monitoring procedure is the correction for the transparency losses due to the radiation damage. This is essential to reach a sta-

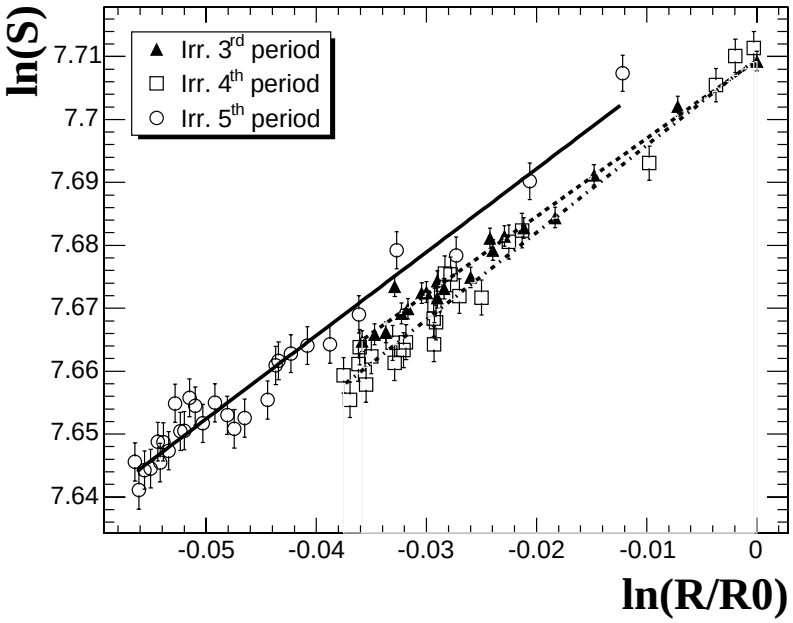

Figure 3.28: Response to the electrons (S) versus relative response to the laser (R/R_0) for three irradiation periods. The logarithms are plotted. Each point corresponds to a beam run and the laser response has been interpolated. The linear fits are superimposed. The data refer to BTCP crystal.

α coefficients						
Crystal number	Crystal type	3^{rd} period 1^{st} irr.	3^{rd} period rec.	3^{rd} period 2^{nd} irr.	4^{th} period irr.	5^{th} period irr.
26	BTCP	1.27 ± 0.11	1.5 ± 0.14	-	-	-
31	BTCP	1.24 ± 0.04	1.16 ± 0.3	-	1.38 ± 0.05	1.32 ± 0.05
32	APATITY	1.20 ± 0.07	1.21 ± 0.06	1.30 ± 0.07	-	-
37	APATITY	1.19 ± 0.08	1.18 ± 0.3	1.22 ± 0.11	-	-
Average		1.26 ± 0.08				
35	SIC	0.81 ± 0.02	3.5 ± 0.8	0.95 ± 0.34	1.3 ± 0.2	0.87 ± 0.06
40	SIC	1.04 ± 0.07	0.98 ± 0.04	-	-	1.10 ± 0.04
28	SIC	0.84 ± 0.05	1.3 ± 0.3	-	1.16 ± 0.06	1.10 ± 0.08
39	SIC	0.99 ± 0.03	1.85 ± 0.15	-	-	0.96 ± 0.16
Average		0.99 ± 0.09				

Table 3.3: α coefficients computed during the irradiations with electrons and the recovery period.

ble response over many LHC cycles, which means between subsequent calibration points. Following Equation 3.9 the correction can be expressed as:

$$S_{corr} \;=\; S(t)_{raw}\Big(\frac{R_0}{R(t)}\Big)^{\alpha}\,, \tag{3.19}$$

where $S(t)_{raw}$ represents the direct measurement at the time t. Unfortunately it will not possible to measure the parameter α for all crystals before the LHC operation so the correction has to be universal. The universality of the correction has been already demonstrated during the 2002 and 2003 test beams [63], however only for BTCP crystals, all belonging to the same production batch. All the data collected In this analysis are corrected with the two mean values of α, respectively for the for BTCP and SIC production batches (see Table 3.3.4). From the equation 3.19 it can be observed that the value of the first point affects the correction procedure. To measure it correctly, the mean of the crystals' response in many runs before the irradiation has been considered.
Figure 3.29 reports both the raw response and the response after the correction with the laser during the irradiation with electrons both for a BTCP crystal and for a SIC crystal. It shows that the accuracy of the correction does not depend on time. Figure 3.30 presents the distribution of the residuals $(S_{corr} - S_0)/S_0$ for both crystals irradiated with electrons. The accuracy after the correction is at the 0.24% level for the BTCP and 0.3% level for the SIC.
The effectiveness of the correction procedure during the whole irradiation with electrons, covering a time interval of more than 1600 hours, is finally tested (see Figure 3.31). The levels of accuracy reported above are confirmed by the analysis of the whole irradiation period of the crystals in the supermodule under irradiation, as shown in Figure 3.32 for the BTCP and for the SIC crystals. The stability of the corrected response is at the level of 0.4% for the BTCP batch and 0.41% for the SIC batch.

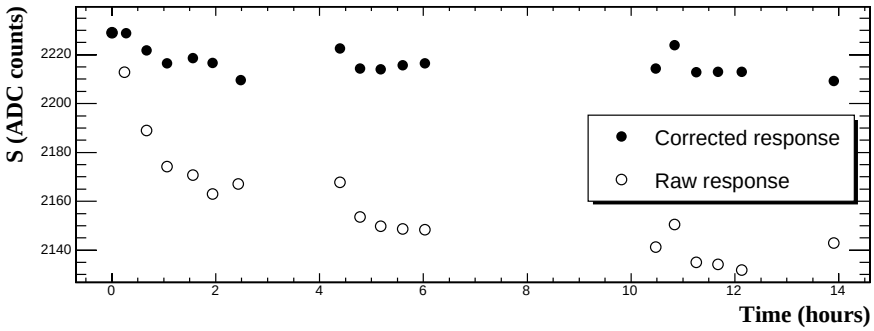

(a)

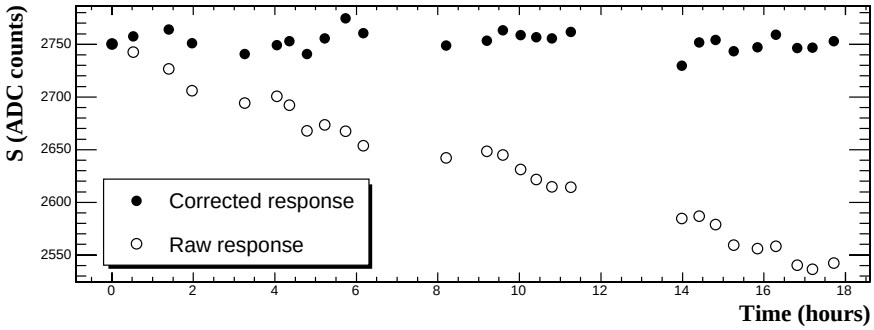

(b)

Figure 3.29: Dependence of the raw response (open dots) and corrected response (full dots) on the time. (a): irradiation with electrons of a BTCP crystal during the 3^{rd} period. (b): irradiation with electrons of a SIC crystal during the 3^{rd} period.

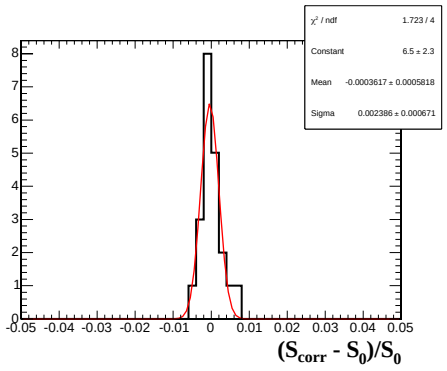

(a)

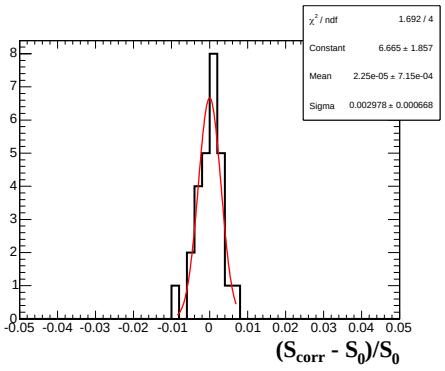

(b)

Figure 3.30: Distribution of the residuals $(S_{corr} - S_0)/S_0$ for a BTCP crystal (a) and a SIC crystal (b) irradiated with electrons during the 3^{rd} period.

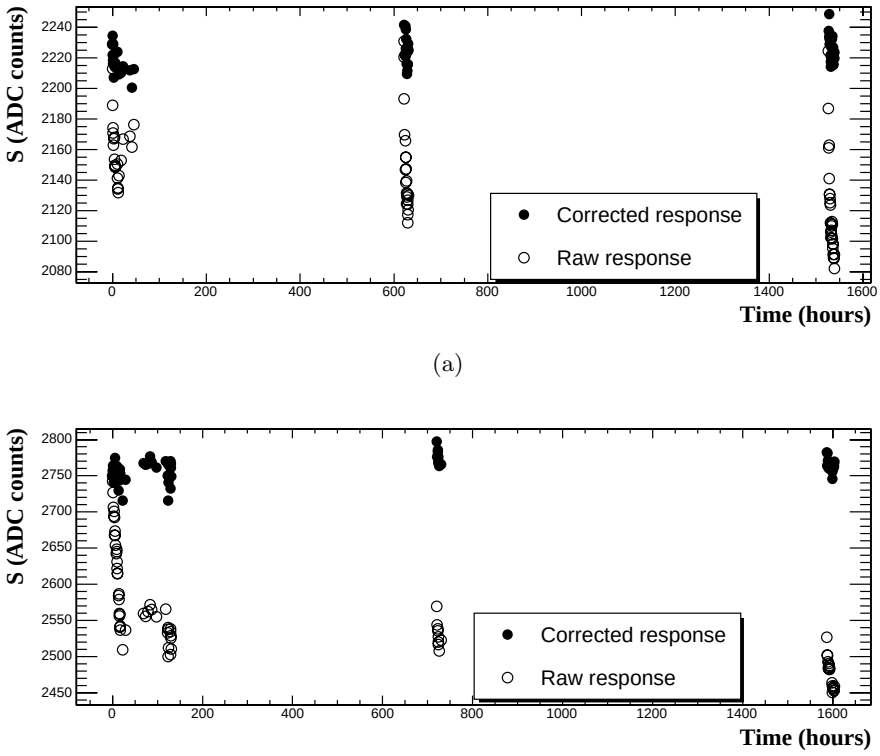

(a)

(b)

Figure 3.31: Dependence of the raw response (open dots) and corrected response (full dots) on the time. (a): irradiation with electrons of a BTCP crystal during the whole test beam period. (b): irradiation with electrons of a SIC crystal during the whole test beam period.

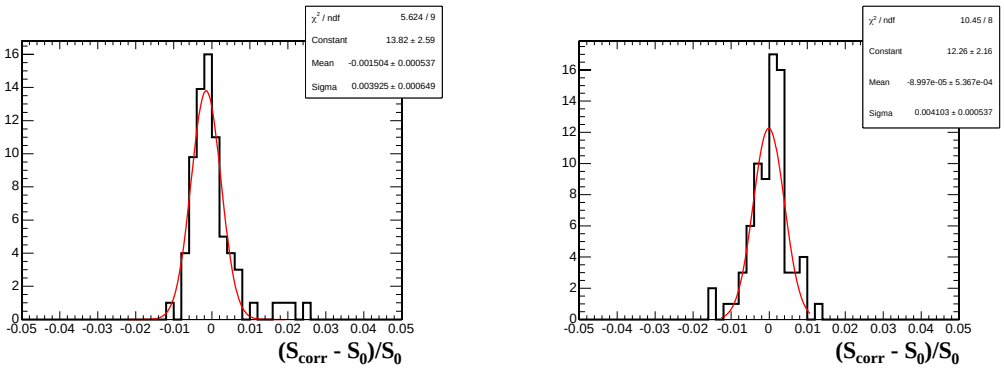

(a) (b)

Figure 3.32: Distribution of the residuals $(S_{corr} - S_0)/S_0$ for a BTCP crystal (a) and a SIC crystal (b) irradiated with electrons during the whole test beam period.

3.4 Summary

In this chapter a detailed investigation of the single crystal energy response has been presented.
This measurement is the key issue for the operations of the ECAL detector in order to allow for precise measurements of electrons and photons at high energy. The procedure of the intercalibration at the test beam and the robustness of the method have been discussed. The intercalibration coefficients obtained with laboratory measurements of the crystal light yield and the commissioning of further supermodules with the first cosmic rays data recorded have been performed.
Since the response of the crystals is affected by the irradiation, the evolution of the crystals response when irradiated with electrons has been studied, also to check its effect on the electron energy measurement. The reliability of the laser monitoring system has been demonstrated. The proposed correction procedure allows to stabilize the response of each single crystal with an accuracy below 0.4%.
The results discussed in this chapter confirm that the constant term of the energy resolution can be kept under $\sim 0.5\%$ value as required for precise measurements of photons and electrons.

Chapter 4

Electron selection and identification

The analysis of the physics channel $A/H \rightarrow \chi_2^0\chi_2^0 \rightarrow 4l^{\pm} + \not{E}_T$ ($l = e, \mu$) includes low p_T isolated electrons to be measured and identified in challenging kinematics and background conditions. At low p_T in particular it is mandatory to have refined electron reconstruction methods to preserve the signal efficiency and reject the "fake" electron contamination from QCD jets.
This requires studies in full simulation (`ORCA` [65]), which are presented in this chapter. The resulting knowledge is then fitted in the fast simulation program (FAMOS [64])) which will be used for the analysis of the CMS sensitivity for this channel. For the case of muons, it is expected that the fast simulation correctly describes the detector response.
The emphasis is put on the study of discriminating variables for the pre-selection of primary electron to tame possible background sources involving "fake" electrons (see Section 4.2). Lepton isolation requirements are introduced like a complementary step to the first data reduction (see Section 4.3). Finally electron identification, exploiting different electron measurement patterns, is shown and a simple cut approach is used to illustrate the identification capability (see Section 4.4).
The reconstruction studies presented here have been performed using back-to-back e^+e^- pairs, QCD di-jet samples and physics samples of $t\bar{t}$ and Higgs boson in the channel $H \rightarrow ZZ^* \rightarrow e^+e^-e^+e^-$.

4.1 Electron reconstruction

4.1.1 Electron clustering

For a single electron (or photon) reaching the ECAL, most of the energy is collected in a small number of crystals. For a supermodule of the ECAL barrel in the test beam, electrons with an energy of 120 GeV impinging at the centre of a crystal for instance deposit about 97% of their incident energy in a 5×5 crystal window [66].
The situation is in general more complicated for the average electron. Electrons traversing the tracker material radiate photons and due to the magnetic field the energy reaches the ECAL after spraying along the ϕ direction. Integrated along the electron trajectory the effect can be very large. About 35% of the electrons radiate more than 70% of their initial energy before reaching the ECAL. In about 10% of the cases, more than 95% of the initial energy is radiated.
Thus, to obtain a measurement of the electron energy at primary vertex and minimize the cluster containment variations, it is essential to collect bremsstrahlung photons. This is the purpose of the super-clustering algorithms.
The **Hybrid algorithm** attempts to profit from the simple geometry of the ECAL barrel and exploits the properties of the lateral shower shape in the transverse direction while dynamically searching for separated (bremsstrahlung) energy in the ϕ direction. In the language of the Hybrid super-clustering, what is considered here as a "seed" cluster is a collection over ϕ of contiguous dominoes made of 3 to 5 crystals in η and separated by other such collections by a valley where less than 100 MeV is observed.
The **Island algorithm** in the endcap builds clusters by connecting rows of crystals containing energies decreasing monotonically when moving away from a seed crystal. Then, superclusters are built by collecting other Island clusters along a ϕ road in both directions around each Island clusters, starting from a list of clusters ordered in E_T, in a procedure called bremsstrahlung recovery.
In order to improve the electron reconstruction for low p_T^{e}, the minimal E_T threshold for the basic seed cluster of a supercluster (E_T^{seed}) was lowered to 1 GeV. Having set this low supercluster seed threshold, extra basic clusters caused by radiated photons with $p_T^{\gamma} > 1\ \mathrm{GeV}/c$ tend to remain separate and form their own supercluster. To better collect the bremsstrahlung and reduce (well below 1%) the probability to find a number of superclusters in excess of the number of isolated electrons, the ϕ roads have been set to ± 0.3 rad in the endcaps and ± 17 crystals (i.e. about ± 0.3 rad) in the barrel.

4.1.2 Track reconstruction

The track reconstruction procedure in CMS is decomposed into several components. Firstly a seed is created whenever two hits compatible with a given beam spot are found in the pixel detector then, starting from the seed, a trajectory is created. Compatible hits on the next silicon layers are searched for and an extrapolation is performed, using a Bethe Heitler modeling of the electron losses and a Gaussian Sum Filter (GSF) in the forward fit [67, 68]. This procedure is iterated until the last tracker layer, unless no hit is found in two subsequent layers. A minimum of five hits is finally required to create a track.
Figure 4.1 shows the efficiency of electron track reconstruction as function of p_T and η, for isolated electrons with a uniform p_T spectrum between 5 and 50 GeV/c and a uniform η distribution within $|\eta| < 2.5$.

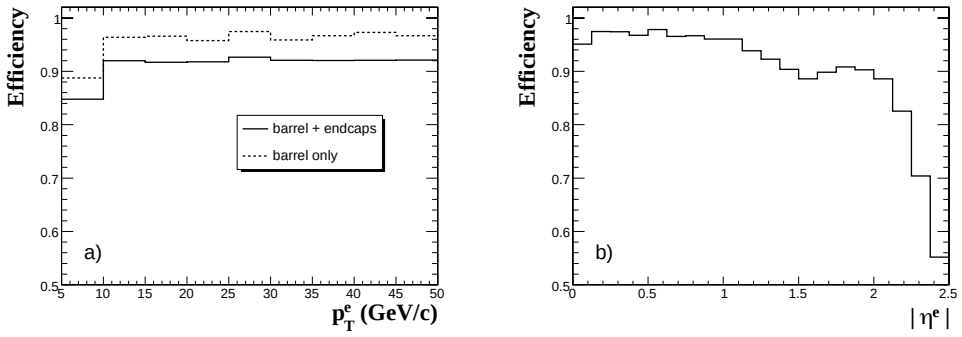

Figure 4.1: Electron track reconstruction efficiency (a) as a function of p_T and (b) as a function of $|\eta|$, for electrons uniformly distributed in p_T between 5 and 50 GeV/c. In (a), the efficiency is shown averaged over the full ECAL barrel and endcaps η range (full line) and for the barrel only (dotted line).

The efficiency is defined as the fraction of generated electrons which have a reconstructed electron track with the same charge and which matches in η and ϕ within ± 0.05 units. The reconstructed track parameters are evaluated at the point of closest approach to the generated vertex, with a further backward (i.e., outside-in) fit of the trajectory, so as to improve the accuracy of their determination. A drop in efficiency at low p_T is visible. The algorithm is quite efficient in the full pseudo-rapidity range with a drop at $|\eta^e| = 1.5$ and another one towards $|\eta^e| = 2.4$. The first drop corresponds to the transition region between the ECAL barrel and endcaps and is mainly due to an inefficiency in the reconstruction of superclusters. The second drop is due to the lack of coverage by the pixel endcap disks.
When using the GSF to fit the track, the parameters of all the Gaussian dis-

tributions The knowledge of the track momentum at the outermost state gives the possibility of estimating from the track fit the fraction of energy lost by bremsstrahlung. The difference between the magnitude of the momentum at the vertex and at the layer of the outermost hit is well visible in Figure 4.2a.

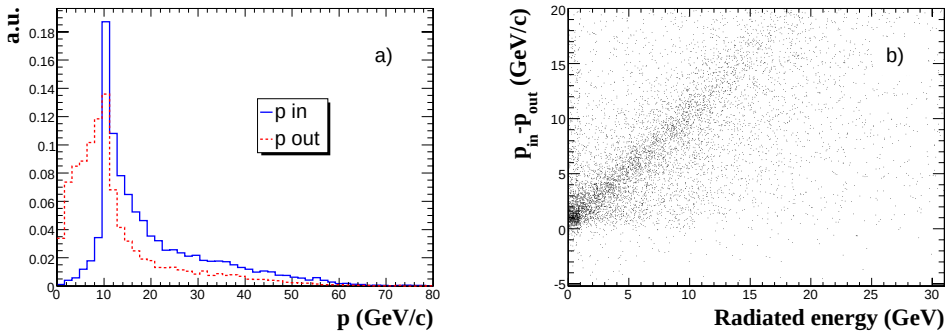

Figure 4.2: Estimation of the bremsstrahlung radiated energy using the GSF track parameters, for electrons with $p_T^e = 10$ GeV/c; a) track momentum evaluated at the vertex (full histogram) and at the outermost hit (dashed-dotted histogram); b) difference between track momentum at the vertex and at the outermost state against the energy radiated via bremsstrahlung photons along the electron trajectory. The momentum is obtained from the weighted mean of the Gaussian mixture.

The difference between the momentum magnitude at vertex and at the last hit, $p_{\text{in}} - p_{\text{out}}$, is a measure of the integral amount of bremsstrahlung. Figure 4.2b shows the difference of the momenta measured at both track ends versus the generated energy sum of the emitted photons. A strong correlation is observed. The mean fraction of the energy radiated along the complete trajectory is roughly proportional to the integral amount of material traversed which varies strongly with η. The relative difference between the momenta measured at both track ends,

$$f_{\text{brem}} = (p_{\text{in}} - p_{\text{out}})/p_{\text{in}} \tag{4.1}$$

is linearly dependent on the radiated energy fraction, f_{brem} is therefore used in the definition of electron classes (see Section 4.1.3).

4.1.3 Electron Classification

More elaborate reconstruction procedures, involving recognition of distinct track-supercluster patterns, are necessary to distinguish between "well measured" and "badly measured" electrons. This is particularly true towards low p_T^e. Observables sensitive to the amount of bremsstrahlung radiated along the electron

trajectory and to the pattern of photon emission and conversions are used to classify electrons.
The main observables used are the "measured bremsstrahlung fraction" f_{brem} (see equation 4.1), the ϕ match between the reconstructed track and the supercluster which is sensitive to the bremsstrahlung collection, the matching between the total energy collected by the supercluster with the momentum measured at the track origin which is sensitive to the energy lost in the tracker material ($E_{\mathrm{sc}}/p_{\mathrm{in}}$) and the pattern of clusters in the superclusters. The cases where an electron is impacting in the immediate vicinity (less than about half the η width of a crystal) of ECAL inter-module borders are considered separately. In such cases, a significant fraction of the electron shower can leak behind the ECAL. Whether or not an electron depositing energy near a border can be measured with precision, is to be evaluated by an algorithmic procedure described elsewhere [42]. The fiducial regions are defined to group such electrons with those impacting in the transition region $1.4442 < |\eta_{\mathrm{sc}}| < 1.5660$ between the ECAL barrel and endcaps. These are kept in a separate *Boundary* class. Such electrons are not further studied, in the other cases electrons are classified into four classes: "Golden electrons", "Big Brem electrons", "Narrow electrons" and "Showering electrons".

- *Golden* electrons. This class represents electrons least affected by radiation emission, with a reconstructed track well matching the supercluster and a well behaved supercluster pattern. It is defined as
  - a supercluster formed by a single "seed" cluster;
  - a measured bremsstrahlung fraction f_{brem} below 0.2;
  - a ϕ matching between the supercluster position and the track extrapolation from last point within $\pm$ 0.15 rad;
  - an $E_{\mathrm{sc}}/p_{\mathrm{in}}$ value in excess of 0.9.

- *Big Brem* electrons. This class contains electrons with a good matching between E_{sc} and p_{in}, a well behaved supercluster pattern, and no evidence of energy loss effects from secondary photon conversion despite a very large measured bremsstrahlung fraction. Electrons for which all the bremsstrahlung is radiated in a single step, either very early or very late when crossing tracker silicon layers, generally fall in this category. The class is defined as
  - a supercluster formed by a single "seed" cluster;
  - a measured bremsstrahlung fraction above 0.5;

  - an $E_{\mathrm{sc}}/p_{\mathrm{in}}$ value between 0.9 and 1.1.

- *Narrow* electrons. In this intermediate class, electrons have a significantly large bremsstrahlung fraction but not as high as for Big Brem electrons, a rather well behaved supercluster (i.e. the bremsstrahlung photons are merged inside the single cluster), but, as for Big Brem electrons, a relaxed track-supercluster geometrical matching. It is defined as

  - a supercluster formed by a single "seed" cluster;
  - an $E_{\mathrm{sc}}/p_{\mathrm{in}}$ value between 0.9 and 1.1;
  - a measured bremsstrahlung fraction and/or a ϕ matching outside the range of Golden and Big Brem electrons.

- *Showering* electrons. This class contains electrons which failed to enter any of the above classes. It includes electron supercluster patterns involving one or several identified bremsstrahlung sub-cluster(s), or case where a bad energy-momentum E/p matching is observed. This bad matching is very likely, for instance, in cases of secondary conversion of some early radiated bremsstrahlung for electrons having radiated a large fraction of their initial energy.

The population of the different classes as a function of the η is shown in Figure 4.3. The shape of the distribution for the Showering class clearly reflects the η distribution of the material thickness (see Section 2.2.1). On the contrary, the observed distribution for the Golden electrons is, as expected, anti-correlated with the material thickness. The small sub-structures observed for instance in the distribution for the population of Narrow electrons at $|\eta| \sim 2.35$ are also a direct consequence of sub-structures in the tracker material distribution.

4.1.4 Energy scale corrections

The lack of containment in cluster reconstructed energy is corrected for as a function of the measured number of crystals in the seed cluster (N_{cry}), as used in HLT reconstruction [69]. The dependence on N_{cry} is very well described by a universal $f(N_{\mathrm{cry}})$ containment correction function. This is found to remain true in the case of electrons from the Showering class, when considering N_{cry} from the seed cluster of superclusters which include bremsstrahlung clusters. In contrast, the total number of crystals in the superclusters does not follow a universal function in such cases.
The reconstructed energy E_{rec}, corrected via $f(N_{\mathrm{cry}})$ and divided by the generated energy E^{e}, is plotted in Figure 4.4 as a function of η for different electron

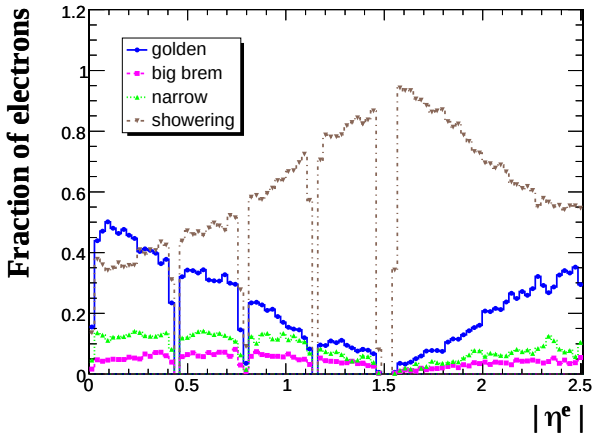

Figure 4.3: The fraction of electron population in the different classes as a function of the generated pseudorapidity for initial energies between 5 and 100 GeV.

classes. The results obtained for the electrons belonging to the Golden, Big Brem and Narrow classes have been found to nicely overlap, such that these classes are grouped together in Figure 4.4. The dependence on η of $E_{\mathrm{rec}}/E^{\mathrm{e}}$ is found

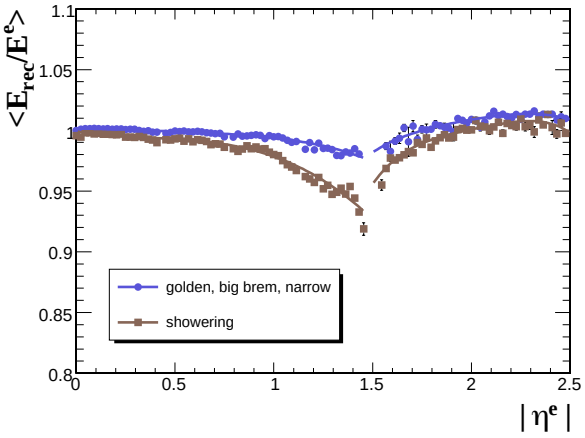

Figure 4.4: Mean of the reconstructed supercluster energy E_{rec} after $f(N_{\mathrm{cry}})$ correction divided by the generator electron energy E^{e} for different classes and as a function of the pseudorapidity. In the η range of the ECAL endcaps, E^{e} is taken as the generated initial energy minus the energy measured in the preshower detector.

to be very much attenuated for these three classes when compared to that for

showering electrons. A variation of more than 0.5% remains only in a band of about 0.7 unit in η centred on the transition region between the ECAL barrel and endcaps. The residual η dependence for the different classes in the barrel and endcaps range are parametrized and a correction is applied.
After having applied the corrections described above, a computation of the effective RMS (σ_{eff}), defined as the half width of the smallest window that contains 68.3% of the distribution, shows an improvement in the resolution of 5% in the barrel and of 10% in the endcaps over the whole 5 to 100 GeV energy range. A more significant gain in resolution is observed when considering only the low energy part of the spectrum.

4.2 Selection of primary electrons

In a multi-lepton final state channel involving electrons, it is important to introduce additional electron requirements to tame possible background sources. This data reduction in a hadron collider is useful to reject the "fake" electron contamination from QCD jets, isolated π_0's overlapping with a $\pi^{\pm}$ or randomly matching a track at primary vertex. The "pre-selection" requirements must preserve the signal acceptance, and especially the electron reconstruction efficiency, until later stages where an analysis can best profit from more evolved algorithms applied to reduced event samples.
In a pre-selection step, a loose geometrical and energy-momentum matching is imposed between the reconstructed electron track and the corresponding supercluster. Good energy-momentum matching is obtained by matching the supercluster energy after applying the energy scale corrections (E_{corr}) with the track momentum (p_{in}) at the closest position from the nominal vertex. The geometrical matching is performed taking the track parameters at interaction vertex, η_{in} and ϕ_{in}, extrapolating to the ECAL assuming a perfect helix, and matching the resulting $\eta_{\text{in}}^{\text{extrap.}}$ and $\phi_{\text{in}}^{\text{extrap.}}$ to the energy-weighted position of the supercluster, η_{sc} and ϕ_{sc}. This is possible thanks to the fact that the energy weighted average impact point of the electron and associated external bremsstrahlung photons, as calculated using information from the supercluster in the ECAL, coincides with the impact point that would have been measured for a non-radiating electron of the same initial four-momenta. The compatibility of the matched object with the expectations from an electron is reinforced by setting an upper threshold on the fraction of the supercluster energy collected in the hadron calorimeter (HCAL). Electron candidates are therefore defined as:

- a reconstructed electron track initiated by the reconstruction of a supercluster in the ECAL matched with hits in the pixel detector;

- an η geometrical matching $|\Delta\eta_{\rm in}| = |\eta_{\rm sc} - \eta_{\rm in}^{\rm extrap.}| < 0.02$;
- an energy-momentum matching between the supercluster and the track, $E_{\rm corr}/p_{\rm in} < 3$;
- a ϕ geometrical matching $|\Delta\phi_{\rm in}| = |\phi_{\rm sc} - \phi_{\rm in}^{\rm extrap.}| < 0.1$;
- a ratio of the energy deposited in the HCAL tower just behind the electromagnetic seed cluster over the energy of the seed cluster $H/E < 0.2$.

The performance of the pre-selection step is checked in terms of the absolute efficiency and of the contamination on electrons from Higgs boson decays $\mathrm{H} \rightarrow \mathrm{ZZ}^* \rightarrow \mathrm{e}^+\mathrm{e}^-\mathrm{e}^+\mathrm{e}^-$ for $m_{\rm H} = 150\ \mathrm{GeV}/c^2$ with a low luminosity pile-up included.
Figure 4.5 shows the absolute pre-selection efficiency of such electron candidate definition as a function of p_T and η. For comparison the efficiency after the loose pre-selection (dotted line) is shown. Loose pre-selection is defined the requested of a reconstructed electron track initiated by the reconstruction of a supercluster and the η geometrical matching with no constrains on the variables sensible on the bremsstrahlung radiation.

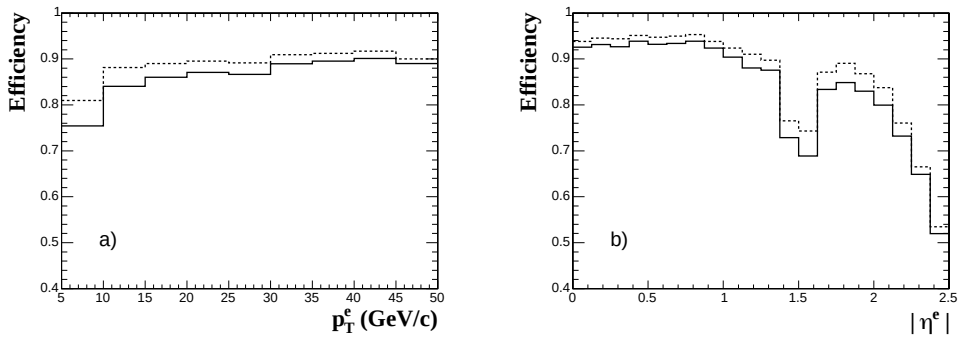

Figure 4.5: Pre-selection (solid line) and loose pre-selection (dotted line) efficiencies for electrons of the $\mathrm{H} \rightarrow \mathrm{ZZ}^* \rightarrow \mathrm{e}^+\mathrm{e}^-\mathrm{e}^+\mathrm{e}^-$ channel for $m_{\rm H} = 150\ \mathrm{GeV}/c^2$: a) as a function of $p_T^{\rm e}$; b) as a function of $\eta^{\rm e}$.

The efficiency is defined as the fraction of generated electrons from the Higgs boson decay which have a reconstructed pre-selected electron track with the same charge and which matches in η and ϕ within ± 0.05 units. For the pre-selected electron the efficiency steeply rises and reaches a plateau around 88% for $p_T^e > 20$ GeV/c, is above 90% for $|\eta^e| < 1.1$ and decreases towards the edge of the tracker acceptance when approaching $\eta^e \simeq 2.5$. The pre-selection efficiency for electrons from the same sample is represented in Figure 4.6 as a

two-dimensional map in the p_T^e versus η^e plane.

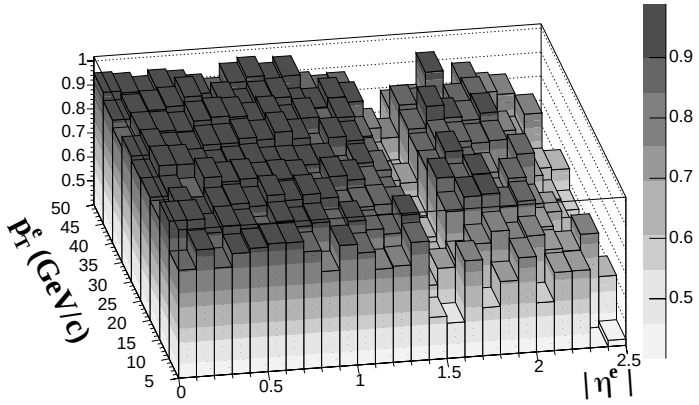

Figure 4.6: Pre-selection efficiency for electrons of the $H \rightarrow ZZ^* \rightarrow e^+e^-e^+e^-$ channel for $m_H = 150$ GeV/c^2 in the p_T^e versus η^e plane.

The contamination on the preselected (solid line) electrons and on the loose preselected ones (dotted line) is presented in Figure 4.7 as a function of p_T and η.

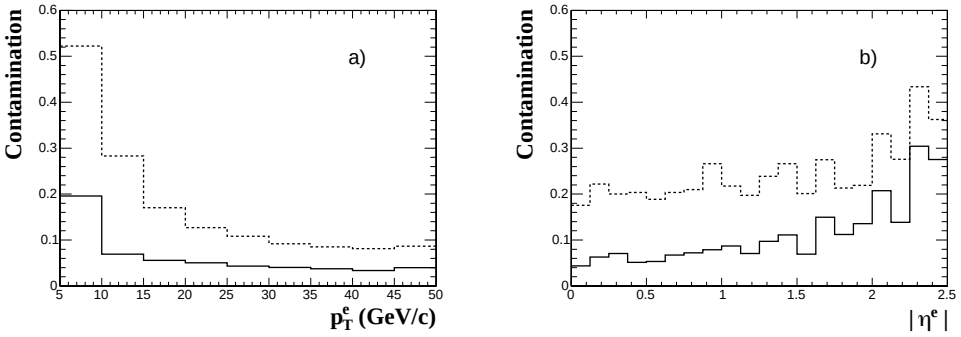

Figure 4.7: Pre-selection (solid line) and loose preselection (dotted line) contaminations for electrons of the $H \rightarrow ZZ^* \rightarrow e^+e^-e^+e^-$ channel for $m_H = 150$ GeV/c^2: a) as a function of p_T^e; b) as a function of $|\eta^e|$.

The contamination is defined as the fraction of reconstructed electrons which don't match any generated electron from the Higgs boson decay. For the preselected electrons the contamination is always kept below 10% for $p_T^e > 10$ GeV/c, is above 10% for $|\eta^e| > 2$ and decreases when approaching $\eta^e \simeq 0$. Imposing requirements on the variables sensible on the bremsstrahlung radiation, an advantage with respect the loose pre-selection step is that one can be reduced a

more-or-less severe fake rate of the electron candidates.

4.3 Electron isolation

Lepton isolation cone requirements can be imposed as a simple and powerful means of suppressing QCD background in multi-lepton physics channels at the LHC. For this reason the isolation step is complementary to the first rejection of electrons achieved from the use of the pre-selection.
For electrons in CMS, the simplest and most powerful isolation criterion is obtained from tracks originating from a common (primary) vertex. Using track measurements at a primary vertex for the electron isolation avoids the complication due to the severe external bremsstrahlung, photon conversion, and early showering in the tracker material. It moreover allows the question of the identification of possible internal bremsstrahlung photons (associated to final state electrons), which might appear in the ECAL within an isolation cone, to be postponed.
The performance of track-based electron isolation are illustrated here by considering the example of the suppression of the $t\bar{t}$ background to the Higgs boson in the channel $H \rightarrow ZZ^* \rightarrow e^+e^-e^+e^-$. Here also, the LHC pile-up for low luminosity is included.
Reconstructed tracks are considered within an isolation cone in the (η,ϕ) plane of radius $R_{\text{cone}} = \sqrt{\Delta\eta^2 + \Delta\phi^2}$ centred on each electron. The tracks are required to have $p_T > 1.5\,\text{GeV}/c$ and $|\Delta\text{IP}_L| < 0.1$ cm, where ΔIP_L is the difference between the longitudinal impact parameter and the z position of the primary vertex. The tracks reconstructed in this way are reconstructed in a completely separate and parallel way from the track associated to the electron candidate, therefore a track associated to the electron itself can be contained within the list of the isolation tracks. To avoid this, a veto cone can be defined around the direction of each reconstructed electron candidate. The dimension of the veto cone has been fixed to a value of 0.015
Starting from a list of tracks contained into the isolation cone region, there are several ways to define an isolation criterion.

- Define isolated those electrons which have no track contained in the isolation cone with transverse momentum greater than a certain threshold.

- Select the electrons for which the sum of the transverse momentum of the tracks contained in the isolation cone is below a certain threshold.

- Select the electrons for which the sum of the transverse momentum of the

tracks contained in the isolation cone divided by the electron p_T is below a certain threshold.

A comparison of these isolation variables is presented in Figure 4.8 for the Higgs boson signal and $t\bar{t}$ electrons, for cone sizes $R_{\text{cone}} = 0.3$ and 0.2 and after pre-selection requirements.

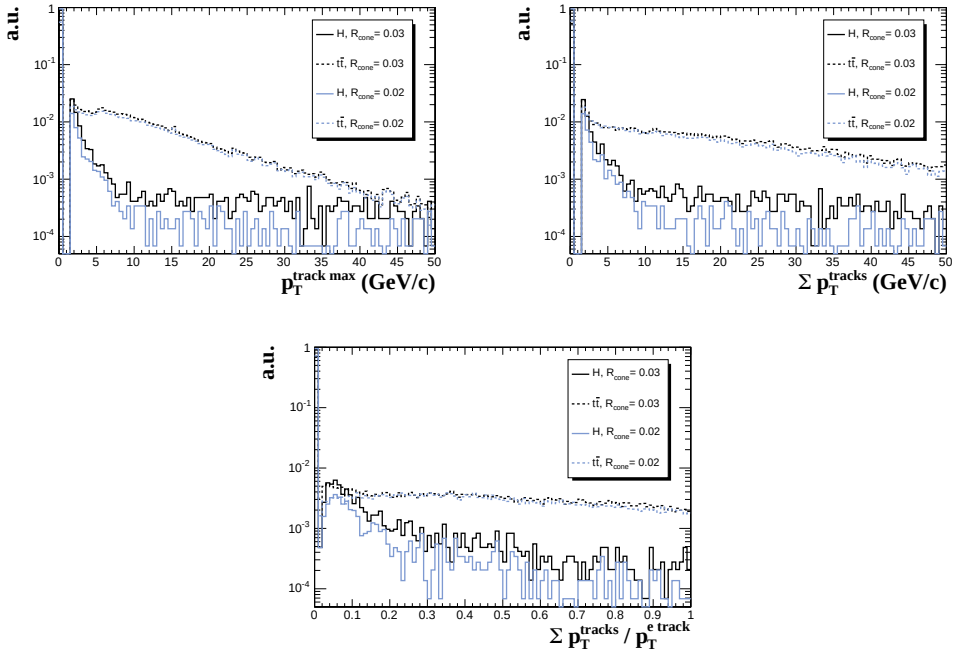

Figure 4.8: top left: track isolation $p_T^{tracks\ max}$, top right: track isolation Σp_T^{tracks} , bottom: track isolation $\Sigma p_T^{tracks}/p_T^e$, for the Higgs boson at $m_H = 150$ GeV/c^2 and for the $t\bar{t}$ background for a cone size $R_{\text{cone}} = 0.3$ and 0.2, for event samples after pre-selection.

In general, the isolation algorithms are performed separately for each electron, And the event isolation is finally defined as the request of having all the four electrons from the Higgs boson decay isolated. Another possibility is to define an event isolation variable, where the isolation region is defined as the sum of the isolation cones around each electron. The first possibility has been preferred. In order to present purely algorithmic isolation efficiency, the electrons are required to match real Monte Carlo electrons from the Higgs boson decay.
Figure 4.9 presents the track based isolation efficiency for the Higgs boson signal in the channel $H \rightarrow ZZ^* \rightarrow e^+e^-e^+e^-$ after preselection as a function of the isolation variable. In this case the sum of the transverse momentum of the tracks contained in the isolation cone divided by the electron p_T is used. The rejection

obtained against the $t\bar{t}$ background as a function of the isolation variable is also shown. The efficiency is defined as the number of events that pass the isolation cuts divided by the number of events which pass the pre-selection. The rejection for the background source is defined as the inverse of the efficiency. For all the

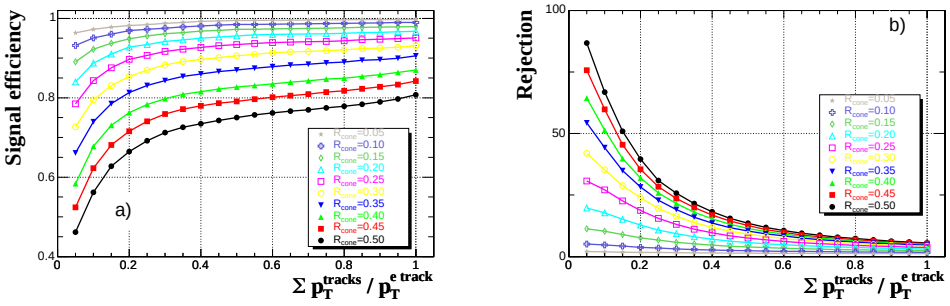

Figure 4.9: Performance of track isolation in the channel $H \rightarrow ZZ^* \rightarrow e^+e^-e^+e^-$ after the preselection described in the text: a) efficiency on the Higgs boson signal as a function of the isolation variable and for different cone sizes; b) rejection against the $t\bar{t}$ background.

cone sizes values the efficiency on the signal steeply rises and reaches a plateau at around 0.2. In term of efficiency, smaller radii give better results because the probability to find in an electron isolation cone another electron candidate is lower.

Figure 4.10 shows the isolation efficiency for the Higgs boson signal as a function of $t\bar{t}$ rejection for different cone sizes R_{cone}. For instance, setting the efficiency for the signal at 90% a rejection power of 20 against the $t\bar{t}$ is reachable.

For comparison, the same results obtained with track isolation $p_T^{tracks\ max}$ and Σp_T^{tracks} are shown in Figure 4.11. The isolation variable is therefore chosen as $\Sigma p_T^{tracks}/p_T^e$.

The selection of primary electrons is based on a further requirements on the hadronic isolation and on the impact parameter with respect to the nominal vertex. The hadronic isolation requirement is imposed on the transverse momentum sum of the considered HCAL towers divided by the electron transverse momentum [70]. As the beam spot is much better defined in the transverse plane, the normalized transverse impact parameter ($\text{IP}_T/\sigma_{\text{IP}_T}$) is used to select primary electrons [71].

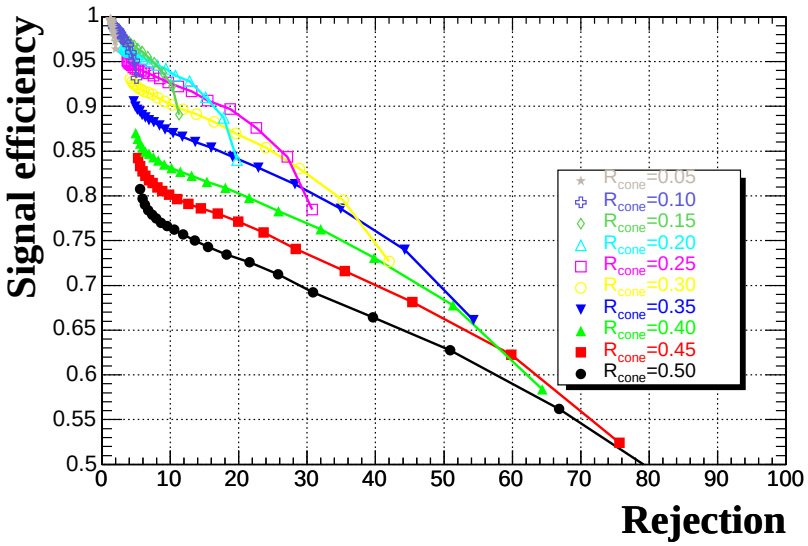

Figure 4.10: Performance of track isolation in the channel $H \rightarrow ZZ^* \rightarrow e^+e^-e^+e^-$ after the preselection, efficiency for the Higgs boson signal as a function of the rejection obtained against the $t\bar{t}$ background. Isolation variable $\Sigma p_T^{tracks}/p_T^e$.

4.4 Electron identification

Further electron identification requirements must be imposed to suppress the possible background, involving "fake" electrons. The performances (efficiency, rejection power, purity) of this identification depends on the nature of the considered background. It also depends on the quality requirements imposed on the electron objects themselves. In general, the electrons are likely to be differently affected by possible fake background sources. Finally, the distinction between multi-clusters and single cluster electron patterns is expected to play an important role in the separation of electron from "fake" electrons in QCD jets formed by overlapping particles.

An electron sample uniformly distributed in p_T from 5 to 50 GeV/c and a sample of di-jet QCD events are used here to evaluate the electron identification capabilities using the outer GSF track parameters and the electron classification. For the QCD di-jet sample the events considered have been generated in two $\hat{p}_T$ bins, $25 < \hat{p}_T < 50$ GeV/c and $50 < \hat{p}_T < 170$ GeV/c and the production cross sections in the two $\hat{p}_T$ bins are respectively 3.3×10^5 nb and 2.4×10^4 nb. A filtering has been applied at generator level to enrich the sample in events which

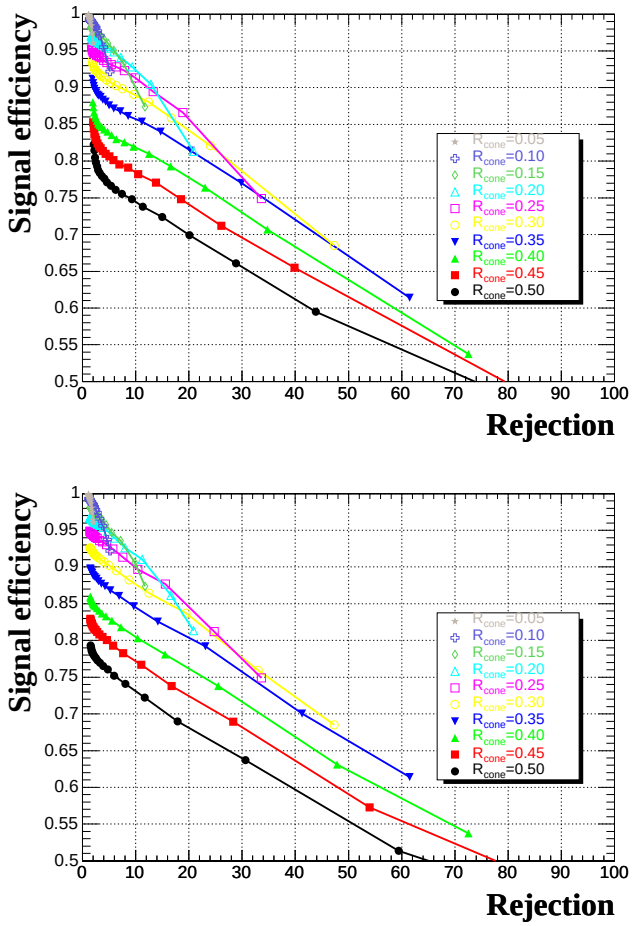

Figure 4.11: Performance of track isolation in the channel H $\rightarrow$ ZZ* $\rightarrow$ $e^+e^-e^+e^-$ after the preselection, efficiency for the Higgs boson signal as a function of the rejection obtained against the $t\bar{t}$ background, top :$p_T^{tracks\ max}$ isolation variable, bottom: Σp_T^{tracks} isolation variable.

would pass the Level-1 electromagnetic trigger of CMS. The filtering is carried out in the following way. Electrons, positron and photons are considered. The first step of the filtering is to look for seed particles with a transverse momentum greater than 5 GeV/c and $|\eta| < 2.7$. Candidate electromagnetic calorimeter trigger tower energies are then estimated by adding all the electromagnetic particles found within $|\eta| < 0.09$ and $|\phi| < 0.09$ from the seed. Trigger tower candidates that lie within $|\eta| < 0.2$ and $|\phi| < 0.2$ from each other are suppressed and only those with the highest transverse momentum are retained. Events have been generated requiring that the transverse momentum of the first candidate is larger that 20 GeV/c and no requirement is applied on the others candidates. About

the 1.3%(17.9%) of events of the first(second) $\hat{p}_T$ bin are found to satisfy the filtering condition. Considering the different production cross sections, the two $\hat{p}_T$ bins are expected to contribute very similar by after the generator filtering. After the generator filtering, about the 24%(45%) of jets are found to reconstruct at least an electron, thereafter called "fake", in the first(second) $\hat{p}_T$ bin. Finally, to further reduce the "fake" electron background, the pre-selection and a loose track isolation ($\sum_{\text{cone}} p_T^{\text{tracks}} \,/\, p_T^{\text{e track}} < 0.5$ and $R_{\text{cone}} = 0.35$) are applied.
Table 4.1 summarizes the QCD di-jet production cross-sections for the two $\hat{p}_T$ bins and the cross-sections after each step when at least one "fake" electron is found in the event.

Jet $\hat{p}_T$ bin	25 GeV/c < $\hat{p}_T$ < 50 GeV/c μb (%)	50 GeV/c < $\hat{p}_T$ < 170 GeV/c μb (%)
σ	330	24
Generator filtering	4.3 (1.3)	4.3 (17.9)
Reconstruction	1 (24)	1.9 (45)
5 GeV/c < p_T^e < 50 GeV/c	0.5 (48)	1.2 (65)
Preselection and Isolation	0.16 (32)	0.44 (35)

Table 4.1: Production cross-sections and cross-sections after each selection step for the two QCD di-jet $\hat{p}_T$ bins. Efficiencies with respect to the previous selection are quoted in brackets.

A QCD di-jet event electromagnetic preselected at generator level is found to have a probability of 7% to give at least a "fake" reconstructed electron with p_T in the range from 5 to 50 GeV/c, used for the electron sample. Considering the total number of fakes in the sample (N_{fakes}) and the total number of jet (N_{jets}) after the generator preselection, the percentage of the fake rate in the whole sample defined as N_{fakes}/N_{jets} is 18.5%. This background is constituted by e.g. isolated π^0's overlapping with $\pi^{\pm}$ (or randomly matching a track at the primary vertex) or by $\pi^{\pm}$ interacting early in the ECAL. Figure 4.12 shows the transverse momentum and η distributions of the "fake" electrons from the QCD jet background. The peak at ~ 20 GeV/c in the transverse momentum distribution corresponds to the jets that pass the single electron trigger while the tail at low momentum are the "fake" electrons kept when the response of the trigger is positive This "fake" electron background constitutes what is therein-after called the QCD jet background.
The jet background can be further discriminated by a precise matching in energy and position between the calorimeter cluster and the track and by the use of shower shape variables. Indeed, hadron showers are longer and broader, and subject to larger fluctuations, than electromagnetic showers. The bremsstrahlung,

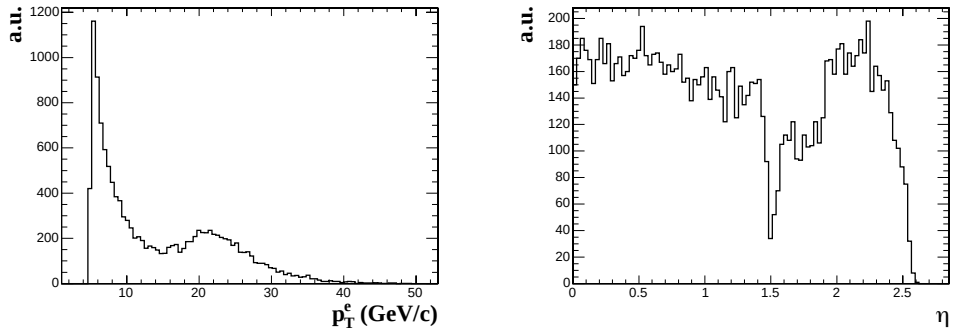

Figure 4.12: Transverse momentum (left) and eta (right) distributions for the "fake" electrons from the QCD di-jet background.

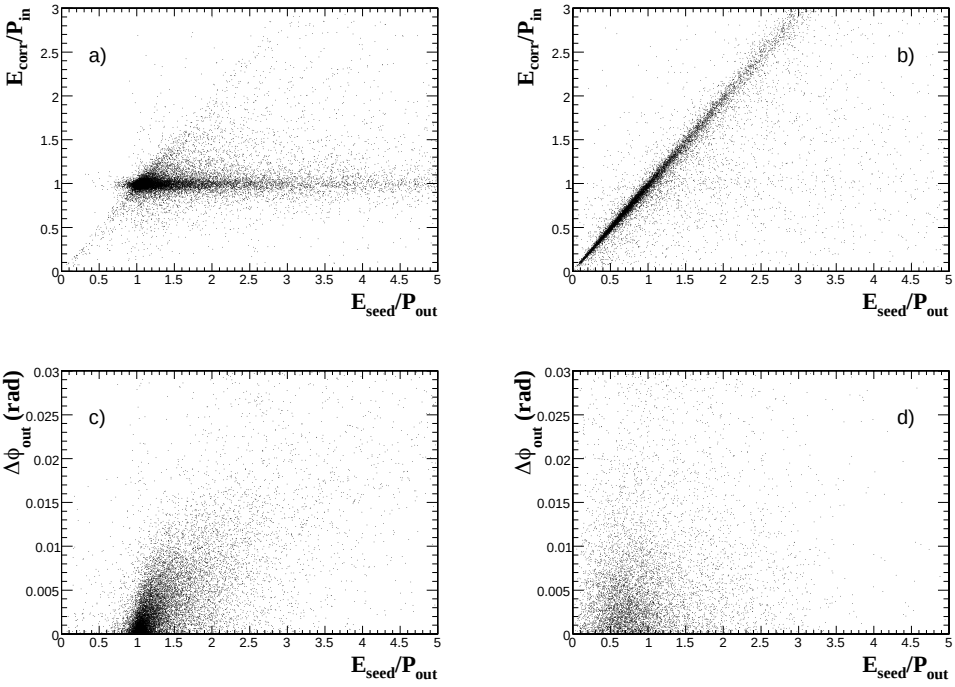

Figure 4.13: Correlations between different matching variables for electrons and for "fake" electron candidates from QCD jet background: a) $E_{\mathrm{corr}}/p_{\mathrm{in}}$ as a function of $E_{\mathrm{seed}}/p_{\mathrm{out}}$, electrons; b) $E_{\mathrm{corr}}/p_{\mathrm{in}}$ as a function of $E_{\mathrm{seed}}/p_{\mathrm{out}}$, jets; c) $\Delta\phi_{\mathrm{out}}$ as a function of $E_{\mathrm{seed}}/p_{\mathrm{out}}$, electrons; d) $\Delta\phi_{\mathrm{out}}$ as a function of $E_{\mathrm{seed}}/p_{\mathrm{out}}$, jets. Track parameters are either taken at the vertex ($_{\mathrm{in}}$) and matched with the supercluster parameters or at the outermost track position ($_{\mathrm{out}}$) and matched with the seed cluster. Distributions are for the barrel only.

however, affects the electron identification capability. The electron shower shape, in particular in the ϕ projection, appears distorted. On the other hand, the emission of radiation in the tracker volume is a characteristic almost exclusive to electrons.

In addition of using track parameters at interaction vertex, the cluster-track matching can take advantage of GSF track parameters at the outermost layer, as these can better match the electron-induced component of the supercluster. Figure 4.13 presents correlations between $E_{\text{seed}}/p_{\text{out}}$ and $E_{\text{corr}}/p_{\text{in}}$ and between $\Delta\phi_{\text{out}}$ as a function of $E_{\text{seed}}/p_{\text{out}}$ for electrons and for the jet background. Different patterns resulting from the physics correlation due to bremsstrahlung in the electron case can be seen. In particular the behavior of $E_{\text{corr}}/p_{\text{in}}$ versus $E_{\text{seed}}/p_{\text{out}}$ in the case of the electron shows a blob where the energy measurements using the vertex and the outermost position are precise and tail at high $E_{\text{seed}}/p_{\text{out}}$ values. These events are the big brem electrons exactly characterized by a good matching between the supercluster energy and the track parameters taken at the vertex and and no evidence of energy loss effects from secondary photon conversion despite a very large measured bremsstrahlung fraction.

A further improvement in electron identification can be expected from the electron classification. Figures 4.14 and 4.15 present the normalized distributions of CMS electron identification variables for electrons of the different classes and for the overall jet background, for electron candidates in the ECAL barrel. Figures 4.16 and 4.17 present the same distributions in the ECAL endcaps.

The variable H/E was introduced in Section 4.2. The variable Σ_9/Σ_{25} is the ratio of the energy sums over 3×3 and 5×5 crystal matrices centred on the highest energy (i.e. seed) crystal of the seed cluster. The shape variables $\sigma_{\eta\eta}$ and $\sigma_{\phi\phi}$ are defined from the crystals i and seed crystal s of the seed cluster as

$$\sigma_{\eta\eta} = \sum_{crystals} (\eta_i - \eta_s)^2 \frac{E_i}{E_{\text{seed cluster}}} \tag{4.2}$$

$$\sigma_{\phi\phi} = \sum_{crystals} (\phi_i - \phi_s)^2 \frac{E_i}{E_{\text{seed cluster}}} \tag{4.3}$$

The necessity to distinguish electrons from the different classes clearly appears. The effect of bremsstrahlung is visible on the shape variables that involves the ϕ projection, looking at the distribution for golden electrons compared to the the distribution for showering electrons. The distributions of $E_{\text{seed}}/p_{\text{out}}$ and $\Delta\phi_{\text{out}}$ show in addition the behaviour of the narrow and big brem electrons, classes for which the level of bremsstrahlung as measured by the track bremsstrahlung fraction is requested to be high. The threshold at 2 in $E_{\text{seed}}/p_{\text{out}}$ for the big brem

class corresponds to a bremsstrahlung fraction $f_{\text{brem}} > 0.5$ as required by construction for this class. Finally, as was already visible on Fig. 4.13, and expected as a consequence of bremsstrahlung, the shift in $E_{\text{seed}}/p_{\text{out}}$ towards values well above 1 is correlated for electrons with a shift in $\Delta\phi_{\text{out}}$ towards the position of the photon shower.
Considering further the distributions of classified "fake" electrons from the jet background, the following conclusions on the use of identification variables depending on the different electron classes can be drawn:

- the $\sigma_{\eta\eta}$ shape variable is discriminating for all electron classes;
- H/E and $\Delta\eta_{\text{in}}$ and $\Delta\phi_{\text{in}}$ are discriminating for all electron classes, with a slight loss of discriminating power for showering electrons;
- $\sigma_{\phi\phi}$ and Σ_9/Σ_{25} shower shape variables involving ϕ projection gives discriminating power for all but showering electrons;
- E/p_{in} and $E_{\text{seed}}/p_{\text{out}}$ are the most discriminating for the showering class;
- $\Delta\phi_{\text{out}}$, with track momentum from the outermost track position and energy from the electron seed-cluster, is discriminating only for golden electrons.

The fraction of electron candidates from the signal and from the jet background which populates the different classes, integrated over the η^{e} range below 2.5 and with p_T^{e} in the range from 5 to 50 GeV/c, are presented in Table 4.2. The jet

	ECAL barrel fraction of		ECAL endcaps fraction of	
Class	electron (%)	jets (%)	electron (%)	jets (%)
Golden	24	4	17	2
Narrow	9	1	5	0.5
Big Brem	4	0.5	3	0.2
Showering	53	85	69	96
Boundary	10	9.5	6	1

Table 4.2: Fraction of electron candidate from the signal and from the jet background in the different classes and in the barrel and in the endcaps part of the ECAL. The signal is constituted an electron sample uniformly distributed in p_T and η electron in the range $5 < p_T < 50$ GeV/c, and the jet background by "electromagnetic" jets with p_T in the range $25 < p_T < 50$ GeV/c.

background is found to almost exclusively contribute to the showering class. This is due to the fact that this class corresponds to bad E/p match or multi-cluster pattern in the ECAL that are characteristic of the jet background. A large part

of the real electron signal also populates the showering class. As a consequence, the showering class ultimately limits the overall (i.e. class independent) electron identification performance.
A simple cut approach is finally used to illustrate the electron identification capability based on the electron classification, focusing on the two extreme cases of golden and showering electrons. Cuts are defined for each class so as to provide an overall 90% electron efficiency and listed in Table 4.3, as well as the jet rejection for each class for an overall signal efficiency of 90%. The rejection factors are given as obtained relative to the sample of electron candidates after pre-selection and including the loose track isolation requirement. As can be expected, the rejection power obtained is higher for the golden than for the showering electrons. A clear difference is also observed between the barrel and the endcap parts of the ECAL.

	ECAL barrel		ECAL endcaps	
Cut	*Golden*	*Showering*	*Golden*	*Showering*
H/E	0.06	0.14	0.1	0.12
Σ_9/Σ_{25}	0.85	no cut	0.85	no cut
$\sigma_{\eta\eta}$	0.005-0.011	0.005-0.011	0.008-0.022	0.0-0.3
$\sigma_{\phi\phi}$	0.005	no cut	0.01	no cut
E/p	0.9-1.3	0.6-/	0.9-/	0.7-/
$\Delta\eta_{in}$	0.004	0.007	0.007	0.008
$\Delta\phi_{in}$	0.04	0.08	0.06	0.07
$E_{\text{seed}}/\text{p}_{out}$	0.9-1.6	0.75-/	0.6-2	0.8-/
$\Delta\phi_{out}$	0.011	no cut	0.02	no cut
rejection	9.0	7.3	5.9	4.2

Table 4.3: A typical definition of cuts for electron identification based on classes and for electrons in the barrel and in the endcap parts of the ECAL. The corresponding jet rejection factors are given relative to pre-selected electron candidates. The cuts are chosen so as to provide an overall electron efficiency of 90%.

Using these simple cuts adapted to each pre-selected electron class, an absolute overall jet background fake rate efficiency at the level of 6×10^{-4} is obtained while keeping efficiency on electrons of p_T from 5 to 50 GeV/c at the level of 90%.

4.5 Summary

The reconstruction of electrons in CMS has been presented. Cluster-driven pixel seed finding is used for applications in physics requiring high efficiencies for low

p_T^{e} electrons. Track reconstruction of electrons makes use of the Gaussian Sum Filter to build the tracks. CMS electron classes are defined according to the different electron topologies. These topologies are used to define appropriate energy corrections and to serve as basis for electron quality in further analysis involving electrons.

Based on the full sequence of steps for electron reconstruction a new strategy for the selection, isolation and identification of primary electrons exploiting different electron measurement patterns has been studied. Possible discriminating variables for the selection have been presented. The performance of the selection steps are checked in terms of the absolute efficiency and the contamination on electrons from Higgs boson decays $\mathrm{H} \rightarrow \mathrm{ZZ}^* \rightarrow \mathrm{e}^+\mathrm{e}^-\mathrm{e}^+\mathrm{e}^-$ for $m_{\mathrm{H}} = 150\ \mathrm{GeV}/c^2$ with a low luminosity pile-up included. Lepton track isolation requirements have been introduced as a complementary step to the first data reduction to tame possible background sources involving "fake" electrons. New observables sensitive to the amount of bremsstrahlung photons emitted in the tracker volume and their possible conversion in the tracker material have been introduced. It has been shown that different electron identification cut strategies and combination of electron identification observables are needed for the various "classes" of electron patterns. Based on a simple cut approach, the electron identification performance has been evaluated for electrons in the p_T range from 5 to 50 GeV/c against "fake" electrons coming from QCD di-jet background. It is shown that an absolute overall jet background fake rate efficiency at the level of 6×10^{-4} can be obtained while keeping efficiency on electrons at the level of 90%.

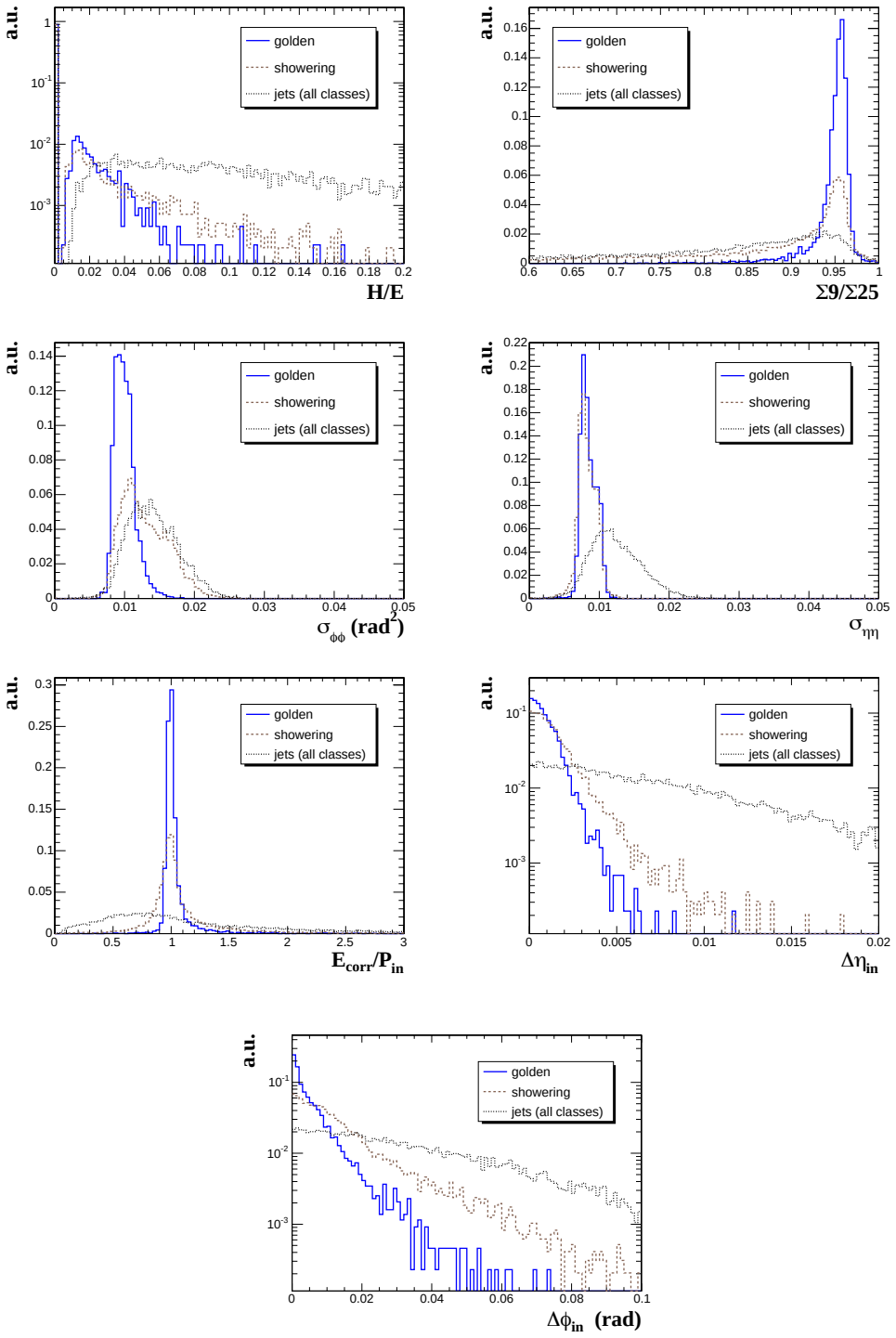

Figure 4.14: Distributions of electron identification observables in the ECAL barrel. The distributions of shower shape observables are shown for golden and showering classes of electrons, and in comparisons with distributions for "fake" electron candidates from QCD jet background.

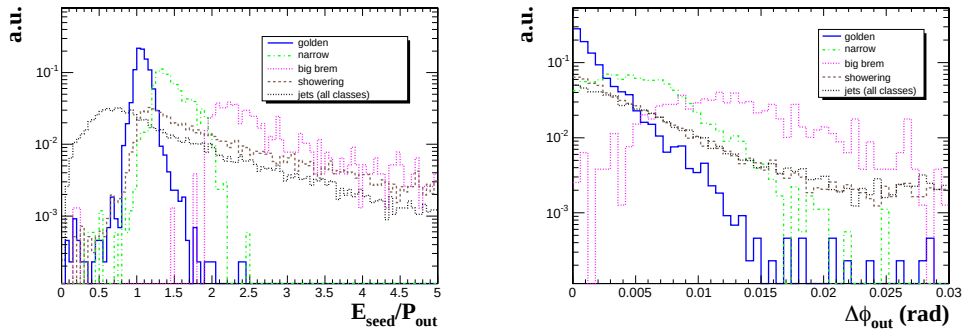

Figure 4.15: Distributions of electron identification observables in the η range of the ECAL barrel. The distributions of track-cluster matching observables are shown for all electron classes, and in comparisons with distributions for "fake" electron candidates from QCD jet background.

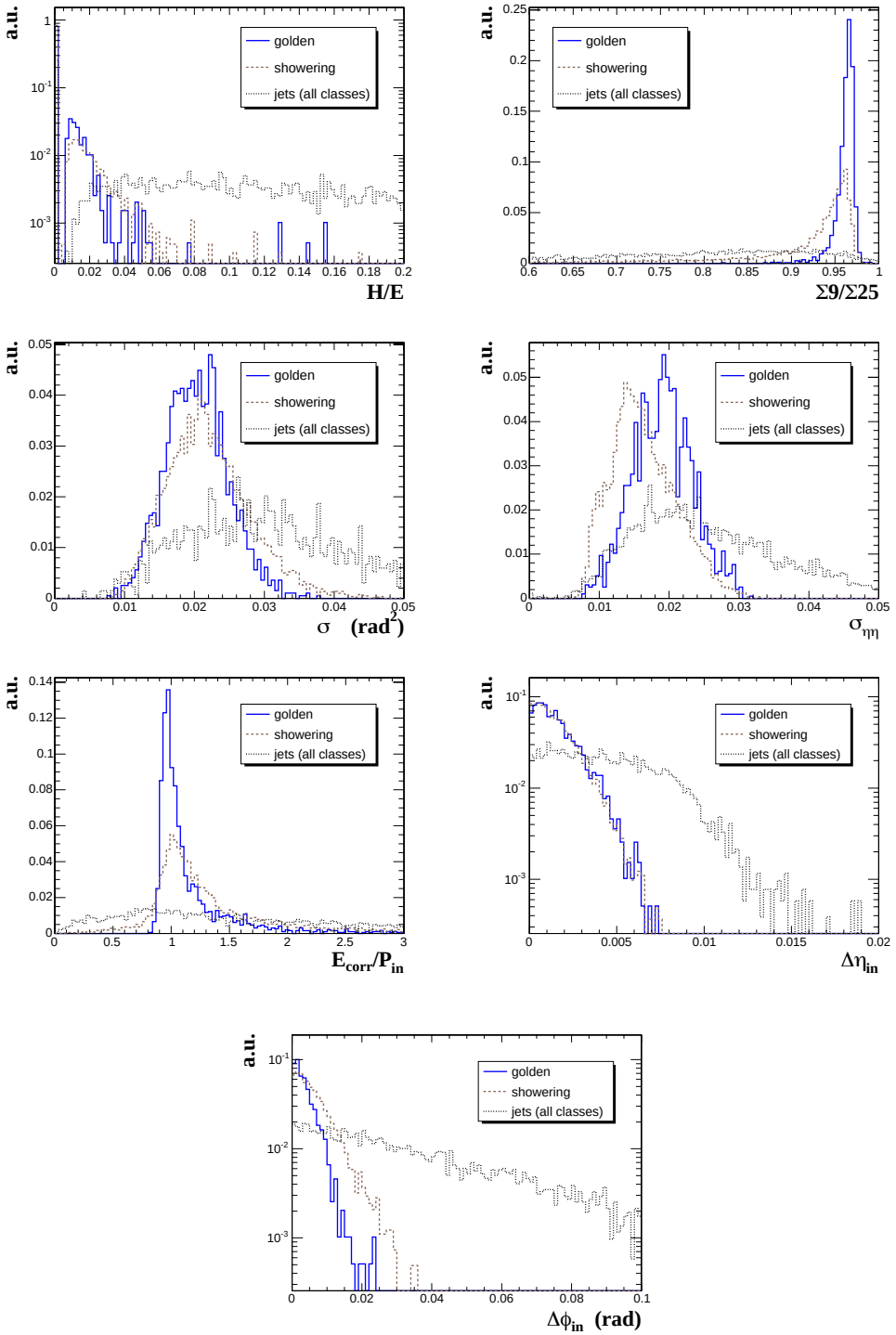

Figure 4.16: Distributions of electron identification observables in the ECAL endcaps. The distributions of shower shape observables are shown for golden and showering classes of electrons, and in comparisons with distributions for "fake" electron candidates from QCD jet background.

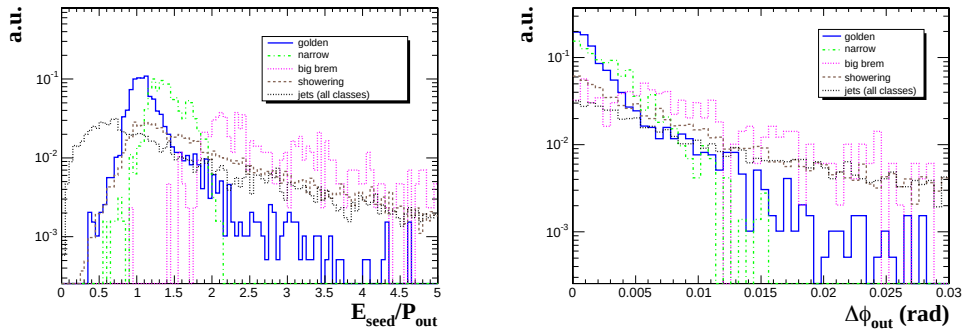

Figure 4.17: Distributions of electron identification observables in the η range of the ECAL endcaps. The distributions of track-cluster matching observables are shown for all electron classes, and in comparisons with distributions for "fake" electron candidates from QCD jet background.

Chapter 5

Observability of heavy neutral Higgs boson decaying into four leptons

In this chapter, prospective study for the observability, with the CMS detector, of the decay of the heavy neutral Higgs bosons into a pair of next-to-lightest neutralinos χ_2^0, followed by the cascade down to the lightest neutralino, $\chi_2^0 \to l^+l^-\chi_1^0$, is studied. The final state is characterized by the presence of four isolated leptons and missing transverse energy. As pointed out in Chapter 1, the Higgs bosons decay into sparticles opens possibilities to explore regions of the parameter space otherwise inaccessible via SM-like decays into ordinary particles [72, 29]. This is the case in particular in the low and intermediate tanβ region of the MSSM parameter space.

Since the phenomenological implications of SUSY are model-dependent, the discovery potential in given experimental conditions has to be studied resorting to some particular model, preferably with a limited number of free parameters. This implies some loss of "generality", but ensures tractable predictions. In the minimal Supergravity model (mSUGRA), only four parameters and one sign, in addition to the SM parameters, need to be specified: the universal scalar m_0 and gaugino $m_{1/2}$ masses, the SUSY breaking universal trilinear coupling A_0, the ratio of the vacuum expectation values of the Higgs fields tanβ and the sign of the Higgsino mass parameter sign(μ).

In Section 5.1 the mSUGRA parameter space is scanned and three benchmark points are defined. Backgrounds are discussed in Section 5.2. The event simulation and online selection are described in Section 5.3 and the analysis cuts are presented in Section 5.4, focusing on the 2e2μ decay channel. The results

obtained for the three benchmark points are shown in Section 5.5. Finally, the results are extrapolated to the whole parameter space and the CMS discovery reach for this decay channel is presented in Section 5.6.

5.1 Signal production

The purpose of this section is to determine the region of the mSUGRA parameter space where the decay chain of A/H into four leptons have a sizeable cross-section times branching ratio. A scan of the $(m_0, m_{1/2})$ parameter plane for $\tan\beta = 5, 10$ and $\text{sign}(\mu) = +$ is performed. Such values for $\tan\beta$ are motivated by the fact that this region is not accessible for the $A/H \to \tau\tau$ channel [24]. It has been checked that the branching ratios are rather insensitive to the sign of the Higgsino mass parameter μ, so that the results are also valid for the negative case. Finally, A_0 enters only marginally in the interpretation of the experimental results at the electroweak (EW) scale and is set to 0 throughout this study.
The signal cross-sections are computed using the HIGLU [73] and HQQ [74] programs. The branching ratios are evaluated using ISAJET [75] (version 7.69).

5.1.1 Production cross-section

The production of the MSSM heavy neutral Higgs bosons at a hadron collider proceeds essentially via the following processes:

$$\text{associated } H \text{ production with } W/Z: \quad q\bar{q} \to V + H \tag{5.1}$$

$$\text{vector boson fusion for } H \text{ production:} \quad qq \to V^*V^* \to qq + H \tag{5.2}$$

$$\text{gluon-gluon fusion:} \quad gg \to H/A \tag{5.3}$$

$$\text{associated production with heavy quarks:} \quad gg, q\bar{q} \to Q\bar{Q} + H/A \tag{5.4}$$

The relative Feynmann diagrams are presented in Section 1.3.2.
Figure 5.1 presents the production cross-sections of the CP-even and CP-odd Higgs bosons in function of m_A for $\tan\beta = 5$(left) and $\tan\beta = 10$(right).
The mass interval scanned (150 GeV/c^2 $< m_A <$ 700 GeV/c^2) is motivated by the fact that it covers the mSUGRA region of the parameter space where the Higgs bosons decay into neutralinos is kinematically accessible.
At $\tan\beta = 5$, the gluon-gluon fusion dominates for $m_A >$ 300 GeV/c^2. For $\tan\beta = 10$, the radiation of a Higgs boson from bottom quarks ($q\bar{q}/gg \to A/Hb\bar{b}$) is dominates over the gluon-gluon fusion. In particular Higgs boson radiation off down quarks cross section is greater than the radiation off top quarks. This is due to the enhancement of the Higgs coupling to bottom type at low $\tan\beta$ regime and has important experimental consequences due to the existence of forward

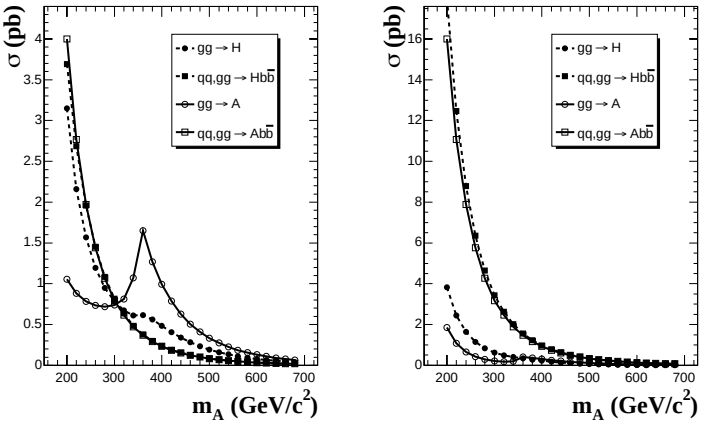

Figure 5.1: Production cross-sections of the heavy neutral Higgs bosons for the two dominant production processes $gg \to A/H$ (dotted lines) and $q\bar{q}/gg \to A/Hb\bar{b}$ (solid lines) for (left) $\tan\beta = 5$ and (right) $\tan\beta = 10$.

b-jets.

The cross sections of gluon-gluon fusion are different for the H and A because in the case of the scalar CP-even Higgs boson the process, mediated by SM-like top and bottom quark loops, has additional contributions from stop and sbottom squark loops.

5.1.2 Decay of the heavy Higgs bosons into next-to-lightest neutralinos

Figure 5.2 shows the branching ratios of A and H decays into next-to-lightest neutralinos in the $(m_0, m_{1/2})$ parameter plane for $\tan\beta = 10$, $\mathrm{sign}(\mu) = +$ and $A_0 = 0$.

In the scanned region, which covers $m_A < 500$ GeV/c^2, the probability for the heavy neutral Higgs bosons to decay into SUSY particles can be as high as 20%. The decay mode $\chi_1^+\chi_1^-$ has the highest branching ratio, however it produces a final state with only two leptons.

Also indicated on Figure 5.2 is the region forbidden for the theory, where no electroweak symmetry breaking is allowed, and the region excluded from cosmological constraints which require a neutral lightest supersymmetric particle. The 95% C.L. limit on the chargino mass obtained from searches at the LEP collider is also shown. The drop in branching ratio beyond $m_{1/2} \backsim 250$ GeV/c^2 which corresponds to $m_A > 350$ GeV/c^2 is due to the opening of the $t\bar{t}$ decay mode. The branching ratio of the CP-odd Higgs decay into next-to-lightest neutralinos

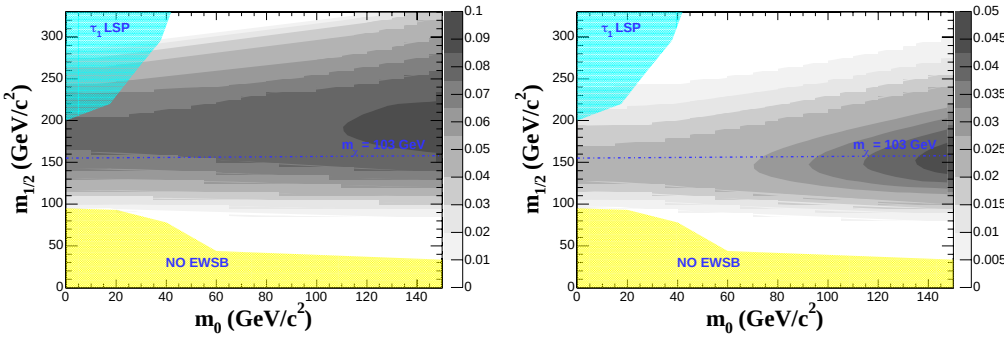

Figure 5.2: Branching ratio of the (top) A and (bottom) H decays into next-to-lightest neutralinos in the $(m_0, m_{1/2})$ parameter plane for $\tan\beta = 10$, sign(μ) $= +$ and $A_0 = 0$. The theoretically and experimentally excluded regions are indicated, as well as the LEP limit on the chargino mass (dashed-dotted line).

is substantially higher than for the CP-even case. This is due to the fact that for the CP-even Higgs the couplings to SM particles are larger, thus leading to a larger total decay width and smaller branching ratios left over for decays into sparticles.

5.1.3 Decays of the next-to-lightest neutralino into leptons

The next-to-lightest neutralino decays into two fermions and a lightest neutralino: $\chi_2^0 \to f\bar{f}\chi_1^0$. The fermions are most often quarks, leading to two jets and missing transverse energy ($\not{E}_T$) in the final state. To focus on a clean signature, the case where the neutralino decays into two leptons $\chi_2^0 \to l^+l^-\chi_1^0$, where $l = e$ or μ is considered here.

If the sleptons are heavier than the χ_2^0, and provided that direct decays into a Z boson are not allowed (or are suppressed), only three-body decays $\chi_2^0 \to l^+l^-\chi_1^0$ contribute. These decays are mediated by virtual slepton or Z exchange. The corresponding branching ratios are presented in Figure 5.3. It is observed that, for the three-body decays, the branching ratios are sizable in the region $m_{1/2} \gtrsim 75$ GeV/c^2, $m_0 \gtrsim 55$ GeV/c^2 and $m_{1/2} \lesssim 2m_0$.

If sleptons are lighter than the χ_2^0, direct two-body decays of the neutralino into a slepton-lepton pair are allowed. In mSUGRA the left and right-handed charged sleptons are not degenerated in mass and the two allowed regions for a χ_2^0 two-body decay are complementary. The branching ratios for such case are presented in Figure 5.4. The two-body decay branching ratios are significant only in a corner of the parameter space in the case of decay involving a left-handed slepton, and in the region $m_{1/2} \gtrsim 130$ GeV/c^2 and $m_{1/2} \gtrsim 2m_0$ in

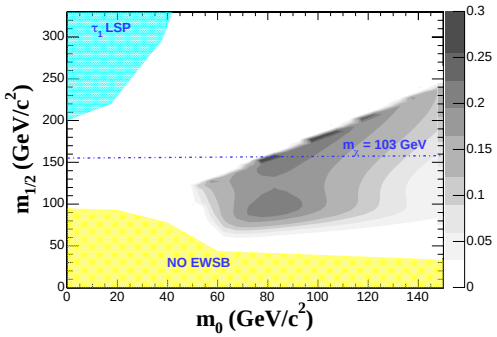

Figure 5.3: Branching ratio of the χ_2^0 three body decay $\chi_2^0 \to l^+l^-\chi_1^0$ in the $(m_0, m_{1/2})$ parameter plane and for $\tan\beta = 10$, sign$(\mu) = +$ and $A_0 = 0$.

the case of a right handed slepton. Beyond $m_{1/2} \simeq 250$ GeV/c^2 the decays of the next-to-lightest neutralino to slepton-lepton pairs are suppressed due to the opening of the $\chi_2^0 \to \chi_1^0 h$ and $\chi_2^0 \to \chi_1^0 Z$ decay channels, in particular for m_0 values above $\simeq 150$ GeV/c^2.

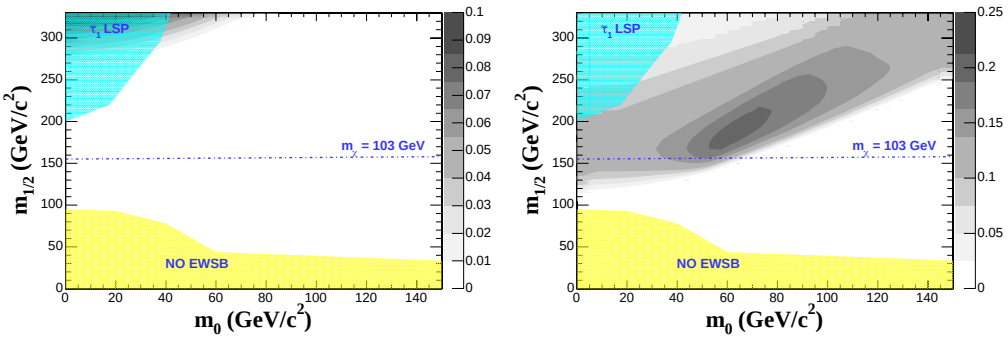

Figure 5.4: Branching ratio of the χ_2^0 two body decays (left) $\chi_2^0 \to \widetilde{l}_L l$ and (right) $\chi_2^0 \to \widetilde{l}_R l$ in the $(m_0, m_{1/2})$ parameter plane and for $\tan\beta = 10$, sign(μ) $= +$ and $A_0 = 0$.

5.1.4 Benchmark points

Figure 5.5 shows the production rate per fb^{-1} for the final state signature $A/H \to 4l^{\pm} + \not{E}_T$ $(l = e, \mu)$ in the $(m_0, m_{1/2})$ plane for fixed $A_0 = 0$, sign$(\mu) =$ $+$ and for $\tan\beta = 5, 10$.
Three benchmark points (A,B,C) are defined for the evaluation of CMS sensitivity whose corresponding mSUGRA parameters and mass of the involved particles

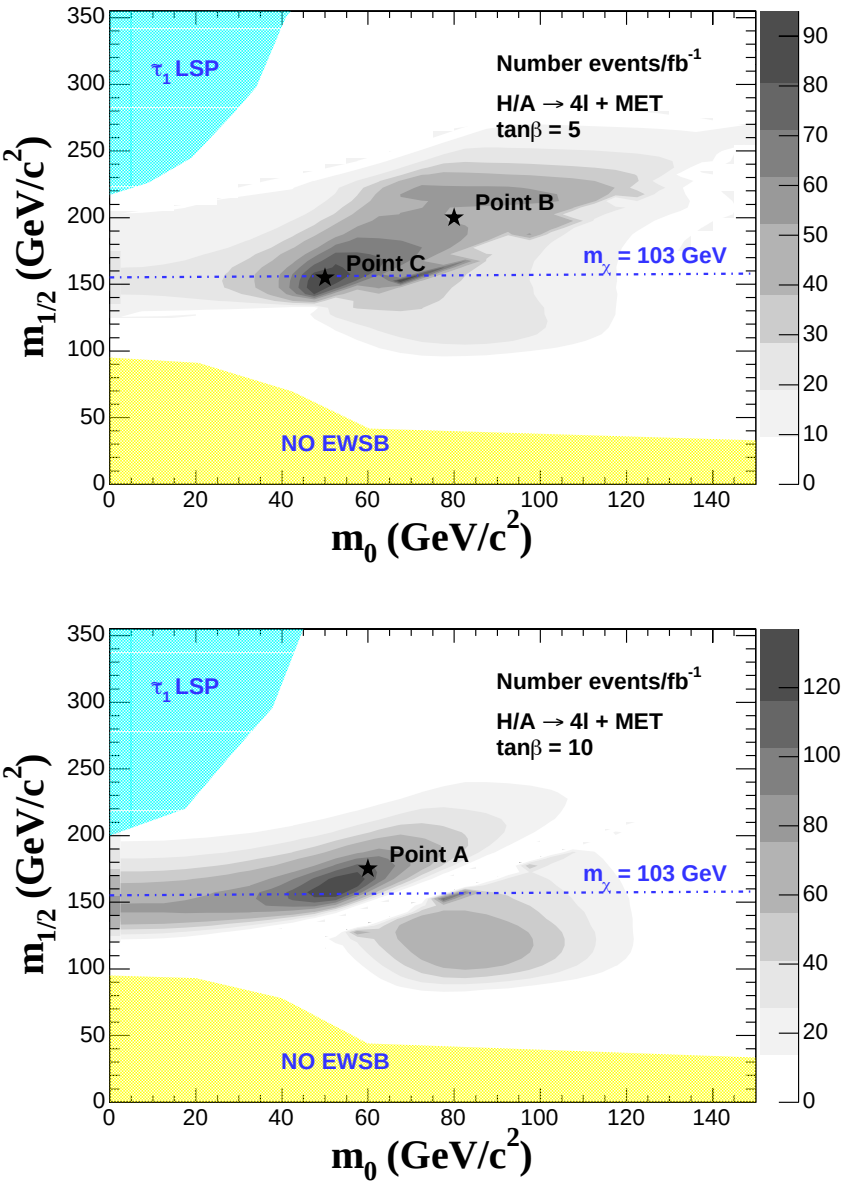

Figure 5.5: Event production rates for the final state signature $A/H \rightarrow 4l^{\pm} + \not{E}_T$ ($l = e, \mu$) in the $(m_0, m_{1/2})$ parameter plane for fixed $A_0 = 0$, sign(μ) = + and for (top) tanβ = 5 and (bottom) tanβ = 10. The three chosen benchmark points are indicated.

are presented in Tables 5.1 and 5.2. All these points have the following general features: a light right-handed slepton, implying that the direct two-body decay of the neutralino into a slepton-lepton pair is allowed, and light squarks and

gluinos. The point C is the closest to the experimental limit on the chargino mass. It is also the most challenging one due to the huge SUSY background and the presence of very soft leptons in the final state coming from the small mass difference between the χ_2^0 and the $\widetilde{l}_R$.

Point	m_0 (GeV/c^2)	$m_{1/2}$ (GeV/c^2)	A_0	tanβ	sign(μ)
A	60	175	0	10	+
B	80	200	0	5	+
C	50	150	0	5	+

Table 5.1: mSUGRA parameters for the three benchmark points.

Point	m_A	m_h	$m_{\chi_1^\pm}$	$m_{\chi 0_2}$	$m_{\chi 0_1}$	$m_{\tilde{l}_R}$	$m_{\tilde{l}_L}$	$m_{\tilde{g}}$	$m_{\tilde{t}_1}$
A	266	110	116	117	64	106	143	443	291
B	325	107	136	137	73	117	166	500	327
C	240	103	104	105	50	101	124	385	254

Table 5.2: Mass of relevant particles for the three benchmark points. Values are in GeV/c^2.

Figure 5.6 shows the transverse momentum of the four leptons in the Higgs signal events for the points A, B and C (after the generator pre-selection cuts defined in Section 5.3). From now on, the analysis focuses on the particular 2e2μ decay channel which benefits from a twice as large event rate as for the 4e or 4μ cases.

5.2 Background processes

There are two main categories of backgrounds to the considered signal: the SUSY and the SM backgrounds.

5.2.1 SUSY backgrounds

In the SUSY category the dominant source of background is the production of leptons from the decays of squarks and gluinos which cascade to charginos and neutralinos. Unlike the neutralinos from the Higgs boson decay, the leptons in this case are produced in association with quarks and gluons. Therefore, the associated large hadronic activity can be used to suppress this type of background. In function of the mass spectrum of the squarks and gluinos three different region can be identified.

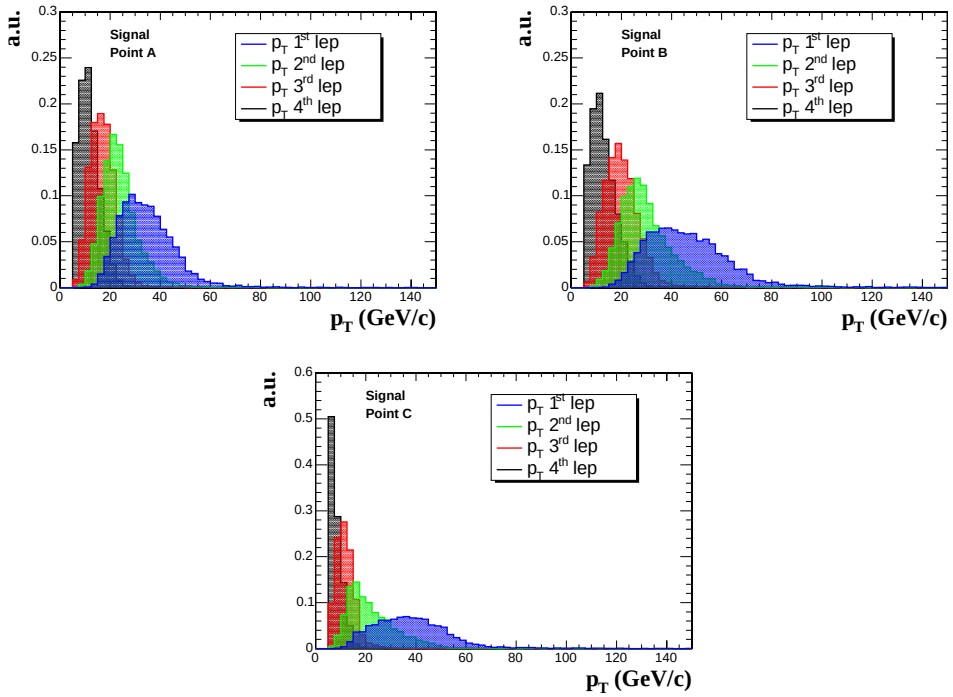

Figure 5.6: Transverse momentum distributions of the four leptons sorted in decreasing order for the Higgs signal and for the three benchmark points A (top, left), B (top, right) and C (bottom).

- Region 1: in this region, the gluinos are heavier than any of the squarks. The decay chains of the produced neutralinos and charginos, which decay in leptons, are

$$\widetilde{g} \to \widetilde{q}\widetilde{q}, \ \widetilde{q} \to q\chi \tag{5.5}$$

- Region 2: in this region some squarks are heavier, other are lighter than the gluino. Hence, rather complicated decay chains are possible, for instance

$$\widetilde{q}_L \to \widetilde{g}q, \ \widetilde{g} \to \widetilde{b}\widetilde{b}, \ \widetilde{b} \to b\chi \tag{5.6}$$

  as the $\widetilde{q}_L$ of the first two generations are expected to be among the heaviest squarks and the $\widetilde{b}_1$ (and $\widetilde{t}_1$) among the lightest.

- Region 3: in this region, the gluinos are lighter than any of the squarks. A typical decay chain is then

$$\widetilde{q} \to \widetilde{g}q, \ \widetilde{g} \to q\bar{q}\chi \tag{5.7}$$

  where the gluino gives rise to a three-body decay mediated by a virtual squark.

An additional but smaller source of background comes from the direct production of slepton or sneutrinos pairs via Drell-Yan processes. Slepton-spleton production predominantly ends up in a 2-leptons final state. Sneutrino-sneutrino production is also potentially a dangerous SUSY background. It can be possibly distinguished from the signal because of the larger $\not\!\!E_T$ and larger p_T of the leptons, as sneutrinos either decay into $\chi_2^0 + \nu$ (leading extra $\not\!\!E_T$) or into $\chi_1^+ + l^-$ (leading to harder leptons).
Another source of SUSY background is the pair production of heavier neutralinos and charginos which will lead of more and harder jets and will often contain a Z boson in the final state.
Finally the direct production of χ_2^0 pairs gives the same signature as the signal, but the production cross section is much smaller due to the strongly suppressed couplings of gauginos to the Z/γ intermediate states. In any case the rejection of this background is difficult, as the hadronic activity in these events is very small.

5.2.2 SM backgrounds

In the Standard model category a background source of four leptons final states arises from non-resonant SM continuum production of $Z^{(*)}/\gamma^* Z^{(*)}/\gamma^*$ and the production of real ZZ pairs which proceeds dominantly via quark-antiquark annihilation. This will be hereafter referred to as the "$ZZ^{(*)}$" background. Other 4l background sources come from pair production of heavy quark flavours such as the $t\bar{t}$ production and the $Z^{(*)}/\gamma^* b\bar{b}$ associated production mediated by QCD, and which proceed dominantly via gluon-gluon fusion. These will be hereafter referred to as the "$t\bar{t}$" and "$Zb\bar{b}$" background processes.

$ZZ^{(*)}$ background

The leading order process for gauge bosons pair production at hadron collider is $q\bar{q}$ annihilation. This process includes the t-channel and s-channel diagrams (see Figure 5.7). One may notice that very different kinematics are expected for the s-channel and t-channel events. For example, the invariant mass of the four leptons for the s-channel contribution will tend to have a peak around the mass with a tail to high invariant masses, because a Z/γ^* is radiated from one of the lepton legs in the decay of the first Z, whereas the t-channel has a more complicated structure with at least two distinct peaks around the Z/γ^* mass and twice the Z/γ^* mass, with a tail to even higher values.
Another production process is the gluon-gluon fusion, $gg \rightarrow ZZ^{(*)}$, which represents a process of higher order in α_s. However it gives a non negligible con-

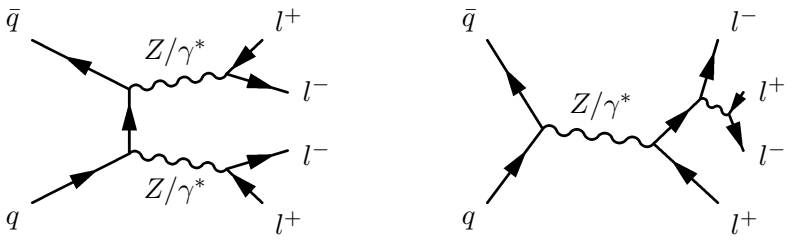

Figure 5.7: ZZ background: $q\bar{q}$ annihilation t-channel diagram (left), s-channel diagram (right).

tribution since gluon-gluon luminosity is much higher for low values of x than quark-antiquark luminosity (see Figure 5.8). The gg contribution is estimated to be of the order of 20% at LO [76], with ±8% uncertainties. Recent calculations with TopREX [77] of the production via gluon fusion of two real Z confirm the above estimation.

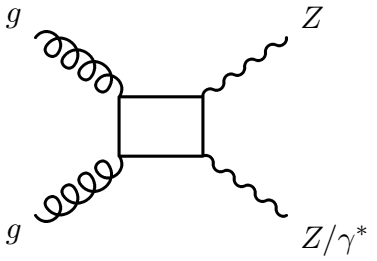

Figure 5.8: ZZ background: gluon-gluon fusion diagram.

The NLO corrections are available only for the quark annihilation and the differential cross-section is re-weighted using m_{4l} dependent NLO K-factors obtained with MCFM [78], with an average K-factor of $\langle \mathrm{K}_{NLO} \rangle = 1.35$. The total production cross section is 29 pb.

$t\bar{t}$ background

The two main processes for the $t\bar{t}$ production in the pp interactions are gluon fusion and quark annihilation (see Figure 5.9). Full NLO calculation is available for the production cross-section which is (840 ± 5% (scale) ± 3%(PDF)) pb [79]. The gluon fusion process has a cross section about six times higher than the quark annihilation process.
Sources of leptons in the final state are the two top quarks decay chains. $t \to Wb$

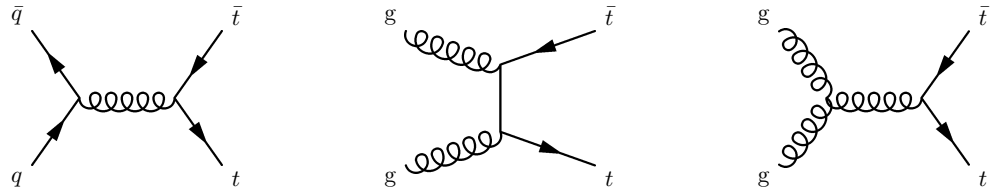

Figure 5.9: $t\bar{t}$ background: diagrams for the production in the $p-p$ interactions at tree level.

has a branching ratio of 99.8%, leptons (e, μ) arise from the semileptonic decays of the bottom quark and from the W, via direct $W \rightarrow l\nu$ or $W \rightarrow \tau\nu \rightarrow l\nu\nu$. Semileptonic decays of mesons produced in $W \rightarrow$hadrons give a negligible contributions to events with four leptons in the final state.

$Zb\bar{b}$ background

The third source of background having four leptons in the final state consists in the $Zb\bar{b}$ production and decay. The leading order diagrams correspond to two possible initial states gg and $q\bar{q}$.
For the cross section calculation, the total LO cross-section for $m_{l^+l^-} > 5$ GeV/c^2 is 115 pb of which about 89% originate from gg processes, 7.7% involve u-like quarks and 3.2% involve d-like quarks in the initial state. The hadronization and decay of the b quarks are left free. A NLO K-factor of 2.4 ± 0.3 is applied [80].
In addition to the $Zb\bar{b}$ production, any $Zq\bar{q}$ production can be studied, for example the $Zt\bar{t}$ or $Zc\bar{c}$ production. These two backgrounds are however negligible if compared to $Zb\bar{b}$. In particular, the production cross section for $Zt\bar{t}$ is 726 fb at leading order [81] and therefore about a factor 1000 lower than the one for $Zb\bar{b}$. On the contrary, a study at generator level for the $Zc\bar{c}$ has been made [82]. The cross-section is about 1.5 times greater than $Zb\bar{b}$, but the preselection efficiency has been found 10 times lower than $Zb\bar{b}$, because of the lower branching fraction into electrons and the softer electron momentum spectrum.

Further SM backgrounds

Another source of Standard Model backgrounds is constituted by events with one or more fake leptons. In particular the case of Z+2jets has been considered in the detailed $H \rightarrow ZZ^* \rightarrow 4e$ analysis [70]. The production rate per fb^{-1} came to 0 after preselection+isolation+electron ID cuts (as defined in the Sections 4.2, 4.3 and 4.4) and the p_T cuts. In addition the jet veto used in the analysis sequence, to suppress in particular the SUSY backgrounds, should further reduce the fake

background.

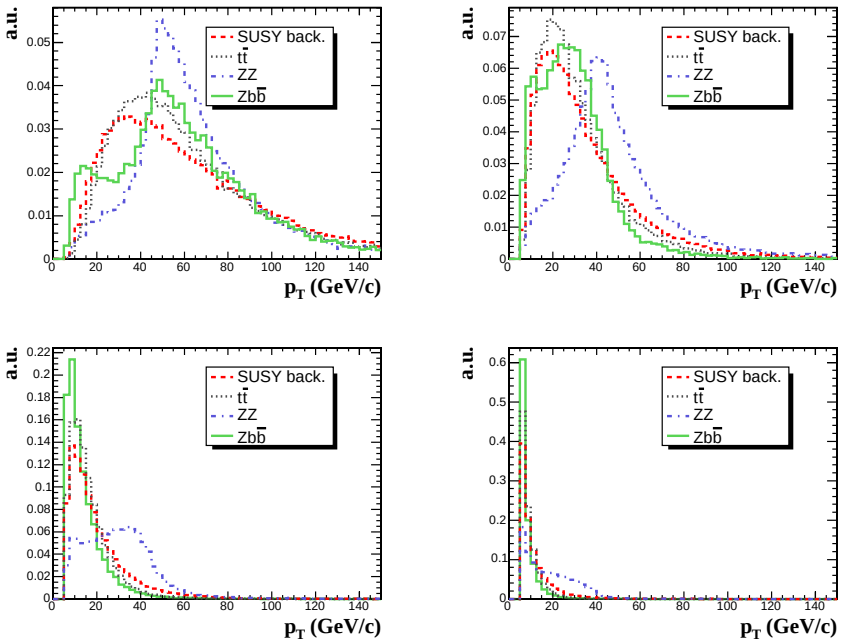

Figure 5.10: Transverse momentum distributions for each of the four leptons, sorted for each event in decreasing p_T^l order, for the different backgrounds to heavy neutral Higgs bosons.

Figure 5.10 shows the transverse momentum of the four leptons sorted in decreasing order for the two considered categories of backgrounds, the SUSY (point A) and the SM backgrounds.

5.3 Event simulation and online selection

ISAJET [75] (version 7.69) and PYTHIA [83] (version 6.225) are used to generate the SUSY mass spectrum, to simulate events and the hadronisation and fragmentation to final state particles for the signal and the SUSY background. PYTHIA is used for the simulation of the SM backgrounds, together with CompHEP [84] for the case of the Zbb̄ background. The parton density functions (PDFs) in the proton are taken from the so-called CTEQ5 distributions. The signal cross-sections are computed using HIGLU and HQQ whereas the SUSY background cross-section is evaluated using PROSPINO [85]. In the SM backgrounds, the Z

bosons (W bosons in the case of the $t\bar{t}$ backgrounds events) are forced to decay to electrons or muons or taus, and in the case of decay to taus, the taus are subsequently forced to decay to electrons or muons. A pre-selection at generator level is applied, requiring an $e^+e^-\mu^+\mu^-$ final state with p_T^e $(p_T^\mu) > 5$ (3) GeV/c and $|\eta| < 2.5$.
The CMS detector response is simulated using FAMOS [86] (version 1.4.0) with the effects of the low luminosity pile-up included. The off-line reconstruction of electrons and muons is performed using standard FAMOS algorithms. A muon candidate is defined as a track extending from the central tracking system to the outer muon system, and an electron candidate is defined as a supercluster in the electromagnetic calorimeter (ECAL) with an associated track.
A first and compulsory condition for the events is to satisfy the CMS Level-1 (hardware) trigger conditions and the filtering of the software High Level Trigger (HLT) [42]. For the two electrons and two muons case, it is found that taking the logical "OR" of the di-muon and di-electron triggers yields a high signal efficiency while suppressing the rate for the SM largest background, namely $t\bar{t}$. The use of single electron and single muon triggers does not improve the final significance. Tables 5.3 and 5.4 summarize the Level-1 and HLT efficiencies for the signal and

Requirement for leptons (matching Level-1/HLT settings)			Efficiency (%) after generator pre-selection		
			Point A	Point B	Point C
$2e\,2\mu$ channel	**I**	2μ candidates ($E_T > 7$ GeV)	94	95	76
	II	$2e$ candidates ($E_T > 14.5$ GeV)	47	57	13
	I OR **II**		**97**	**98**	**79**

Table 5.3: Level-1 and High Level Trigger efficiency for the Higgs signal in the $2e2\mu$ decay channel and for the three benchmark points. Both contributions of the di-electron and of the di-muon triggers are indicated.

Process	Level-1/HLT efficiency (%)
SUSY back. A	90
SUSY back. B	95
SUSY back. C	90
$ZZ^{(*)}/\gamma^*$	88
$t\bar{t}$	86
$Zb\bar{b}$	98

Table 5.4: Level-1 and High Level Trigger efficiency for each of the SUSY and SM background processes.

for the background processes with respect to the generator pre-selection. The

global trigger efficiency is above 95% for the signal at point A and B. It is significantly lower (79%) for the point C due to the very soft leptons spectra arising from the smaller mass difference between the next-to-lightest neutralino and the right-handed slepton in this case.

5.4 Signal versus background discrimination

The first step in the off-line event selection is to require that four leptons are reconstructed with the further requirement that the p_T of the electrons (muons) has a minimum value of 7 (5) GeV/c. The efficiency to reconstruct $e^+e^-\mu^+\mu^-$ events using off-line algorithms is given for the Higgs boson signal in Table 5.5.

	Point A	Point B	Point C
$e^+e^-\mu^+\mu^-$ reconstruction efficiency (%)	80	81	72

Table 5.5: 2e2μ off-line reconstruction efficiency with respect to HLT for each of the three signal benchmark points.

5.4.1 Jet Veto

As already mentioned in Section 5.2, the large hadronic activity associated with the SUSY backgrounds can be used to suppress this type of process. A jet veto is also very efficient to suppress the $t\bar{t}$ and the $Zb\bar{b}$ backgrounds, due to the presence of jets in the final states for both of these background sources.
Jets are reconstructed from the electromagnetic (ECAL) and hadronic (HCAL) calorimeter towers using the iterative cone algorithm [66]. In this algorithm, an E_T-ordered list of input calorimeter towers is created. A cone of size R in (η, ϕ) space is cast around the input object having the largest transverse energy above a specified seed threshold. The objects inside the cone are used to calculate a "proto-jet" direction and energy using the E_T scheme. The computed direction is used to seed a new proto-jet. The procedure is repeated until the energy of the proto-jet changes by less than 1% between iterations and the direction of the proto-jet changes by $\Delta R < 0.01$. When a stable proto-jet is found, all the objects in the proto-jet are removed from the list of the input objects and the stable proto-jet is added to the list of reconstructed jets. In the analysis a cone radius of $R = 0.5$ and a seed tower threshold of $E_T = 1$ GeV are used.
The jet veto consists in rejecting events with at least one reconstructed jet satisfying $E_T > 25$ GeV. A small fraction of signal events is found to be suppressed by the jet veto due to the presence of jets from pile-up events. The sensitivity of

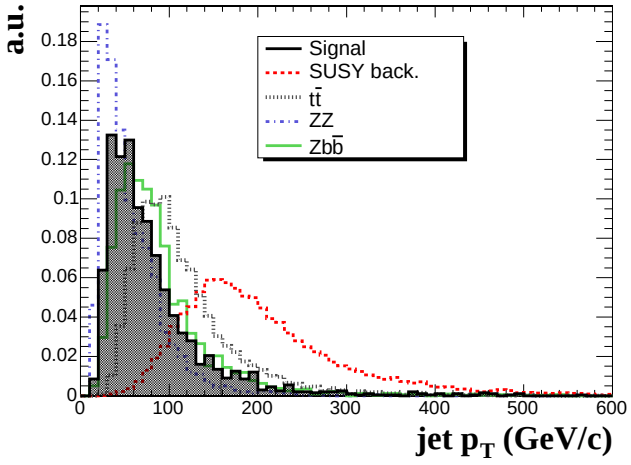

Figure 5.11: Distribution of the hardest jet for the signal (point A) and for the background processes.

the analysis on the signal loss coming from "fake" jets from pile-up is expected to be small and is not taken into account in this analysis. Figure 5.11 shows the distribution of the hardest jet for the signal (point A) and for the background processes.

5.4.2 Lepton isolation

Track-based lepton isolation is used as the main tool to get rid of the $t\bar{t}$ and $Zb\bar{b}$ backgrounds (see Section 4.2). Reconstructed tracks are considered within an isolation cone in the (η, ϕ) plane of radius $R_{\text{cone}} = \sqrt{\Delta\eta^2 + \Delta\phi^2}$ centred on each lepton. The tracks are required to have $p_T > 1.5$ GeV/c and $|\Delta\, IP_L| < 0.1$ cm, where $|\Delta\, IP_L|$ is the difference between the longitudinal impact parameter and the z position of the primary vertex. The lepton isolation variable is then defined as the sum of the p_T of all tracks satisfying these requirements but the lepton one, divided by the lepton p_T. The event isolation is finally defined as the requirement to have all the four leptons of the event isolated.
Figure 5.12 presents the track based isolation efficiency for the signal (point A) after the generator pre-selection as a function of the rejection obtained against the $t\bar{t}$ background for different cone sizes. The cone size and the threshold are tuned to maximize the signal significance. In practice, a sufficient rejection power is obtained for a working point corresponding to an efficiency around 80%.

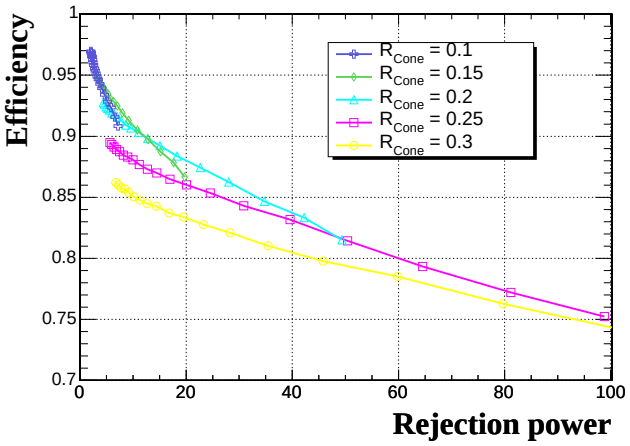

Figure 5.12: Isolation efficiency for the heavy Higgs boson signal (point A) as a function of the rejection obtained against the $t\bar{t}$ background.

5.4.3 Missing transverse energy and 4-lepton transverse momentum

The SUSY backgrounds are characterized by a significant missing transverse energy ($\not\!\!E_T$) due to the presence of lightest neutralinos and of neutrinos produced from W and Z decays in the cascade decays of squarks and/or gluinos.
The missing transverse energy vector is reconstructed from the calorimeter towers (ECAL+HCAL) by summing individual calorimeter towers having energy E_n, polar angle θ_n and azimuthal angle ϕ_n:

$$\sum_n (E_n \sin\theta_n \cos\phi_n \,\hat{\mathbf{i}} \;+\; E_n \sin\theta_n \sin\phi_n \,\hat{\mathbf{j}}) \;=\; \not\!\!E_x\hat{\mathbf{i}} \;+\; \not\!\!E_y\hat{\mathbf{j}}\;. \qquad (5.8)$$

Muon contributions are corrected by replacing the expected calorimeter deposit (about 4 GeV) by their reconstructed track p_T.
Figure 5.13 shows the missing transverse energy for the Higgs signal (thick line) and for the backgrounds. Events are required to have $\not\!\!E_T < 80$ GeV.
In addition, the correlation between $\not\!\!E_T$ and the 4-lepton transverse momentum (p_T^{llll}) in the case of the signal events is used. Events are selected if their distance to the axis $\not\!\!E_T = p_T^{llll}$ is less than 15 GeV. This selection is useful to further suppress the SUSY and $t\bar{t}$ backgrounds, as can bee seen on Figure 5.14 for the 2e2μ case.

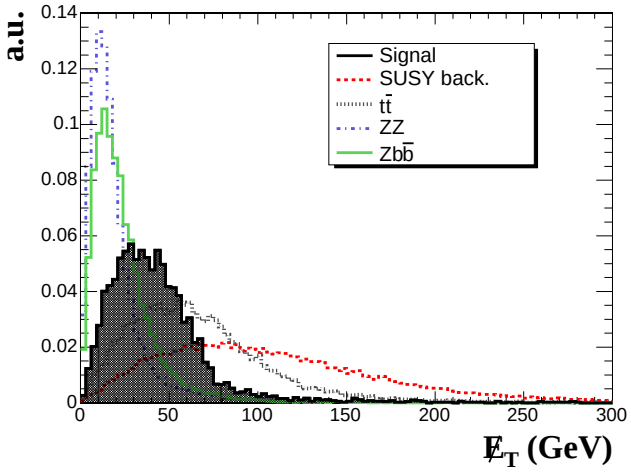

Figure 5.13: Missing transverse energy distributions for the signal (point A) and for the backgrounds.

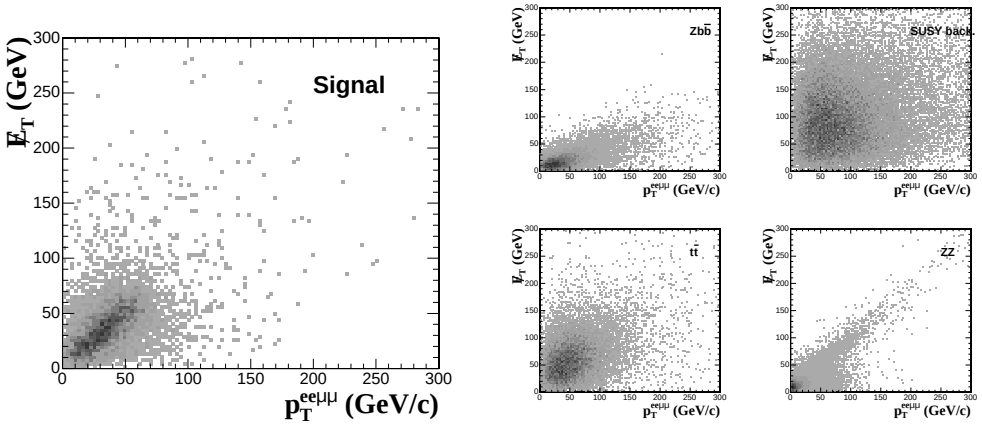

Figure 5.14: Correlation between the missing transverse energy and the 4-lepton transverse momentum: (left) for the Higgs signal (point A) and (right) for the background processes.

5.4.4 Invariant mass cuts

In order to suppress the backgrounds arising from SM $ZZ^{(*)}/\gamma^*$ and $Zb\bar{b}$ production, where at least one of the dilepton pairs is coming from a real Z boson, all events with a dilepton pair of opposite sign and same flavour leptons and satisfying $\mid m_{ll} - m_Z \mid \; < 10$ GeV/c^2 are rejected (Z veto). In addition, a minimum invariant mass of 12 GeV/c^2 is required on each dilepton pair in order to remove

the contamination of bottomed and charmed mesons (Υ, J/Ψ, ...). Figure 5.15 presents the reconstructed di-lepton invariant mass distributions for the signal and for the different backgrounds.

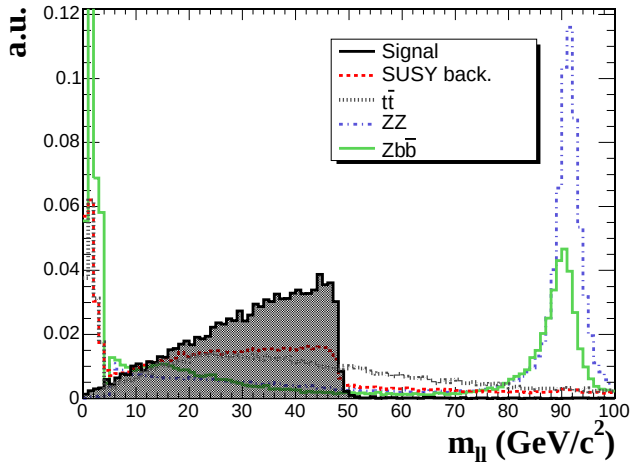

Figure 5.15: Reconstructed invariant mass of the di-muon and di-electron pairs for the signal (point A) and for the backgrounds.

An extra feature that can be exploited in the signal versus background discrimination is the shape of the dilepton invariant mass spectrum, which present a characteristic kinematical edge in the case of signal events. Since there are two χ_2^0's present in the Higgs decay, a double kinematical edge is visible in the particular case of the 2e2μ decay channel if one selects only events containing two electrons and two muons and then plots the di-electron invariant mass versus the di-muon invariant mass. The kinematical endpoint is near the mass difference between the χ_2^0 and χ_1^0, or if sleptons are intermediate in mass as is the case for the chosen benchmark points, near $\sqrt{(m^2_{\chi_2^0} - m^2_{\tilde{l}})(m^2_{\tilde{l}} - m^2_{\chi_1^0})}/m_{\tilde{l}}$. These distributions are shown for the three signal points and for the backgrounds in Figures 5.16 and 5.17 .

If not already discovered, the observation of such a kinematical edge would be a striking indication of supersymmetry. Conversely, an "a priori" knowledge of the mass difference between the next-to-lightest and the lightest neutralinos, in the case where SUSY would have been already discovered through squarks, gluinos, or sleptons, could help to separate a heavy neutral Higgs signal from the backgrounds. In the region of the parameter space relevant for this study, a loose cut in the mass difference at 65 GeV/c^2 is suitable for all Higgs mass values and is therefore used here as a starting value. An estimation of the mass difference

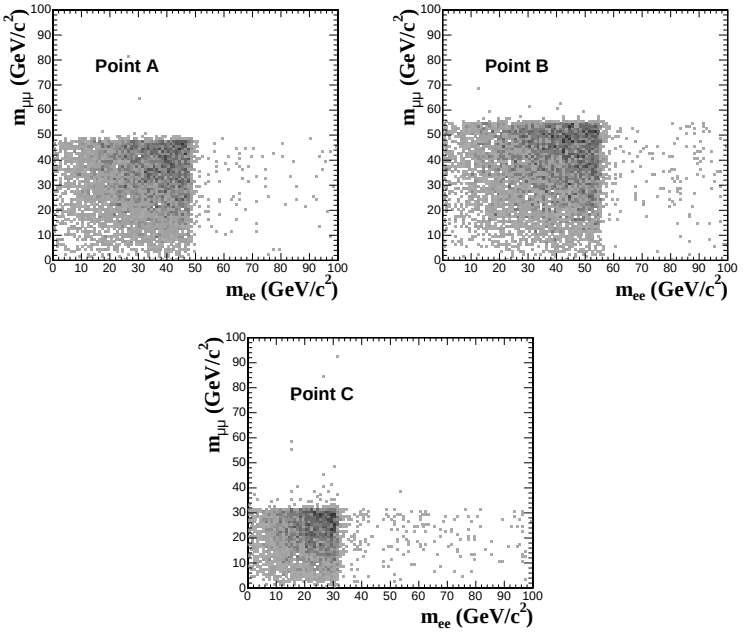

Figure 5.16: Double kinematical edge in the di-muon versus di-electron invariant mass distribution for the signal for the three benchmark points.

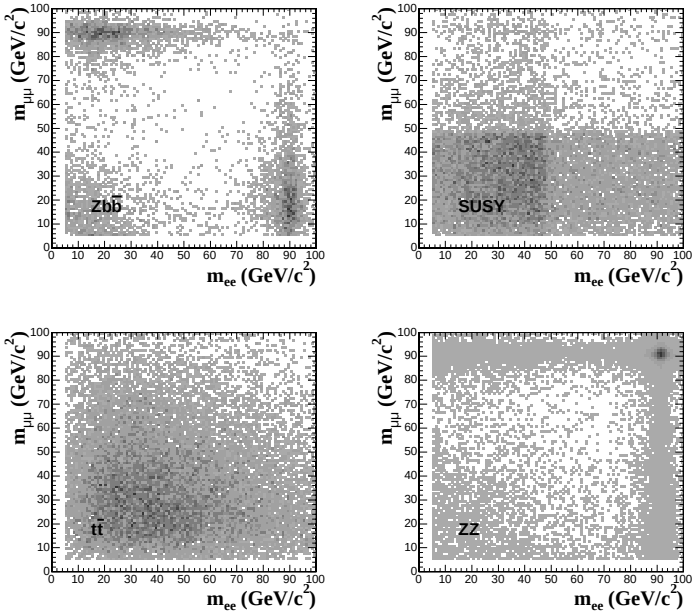

Figure 5.17: Double kinematical edge in the di-muon versus di-electron invariant mass distribution for the background processes.

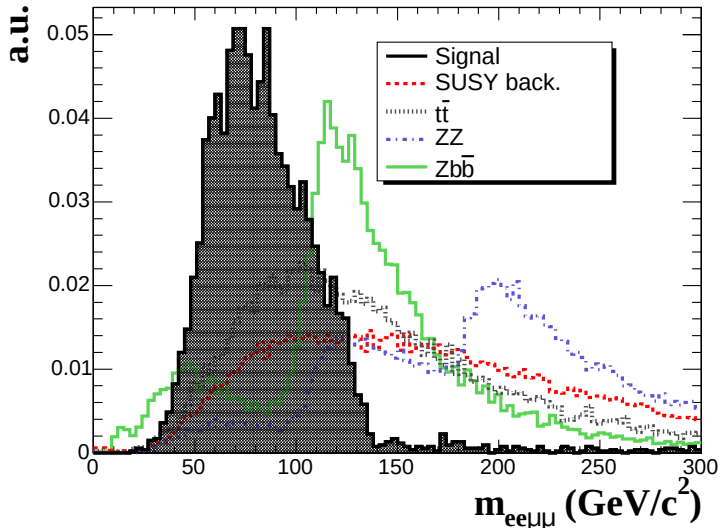

Figure 5.18: Distribution of the reconstructed invariant mass $M_{ee\mu\mu}$ for the Higgs boson signal (point A) and for the backgrounds.

from the discovery of other SUSY particles could be further used to improve the significance of the heavy neutral SUSY signal in a further refinement of the analysis.

Finally, a loose Higgs mass window cut is applied, also suitable for all relevant values of the parameter space. Events are required to have a reconstructed 4-lepton invariant mass within 20 GeV/c^2 $< m_{llll} <$ 180 GeV/c^2. Figure 5.18 presents the 4-lepton invariant mass distributions for the signal and the backgrounds and for the 2e2μ specific case.

5.5 Results for the three benchmark points

Tables 5.6 and 5.7 summarize the production cross-sections and the cross-sections after each step of the online and off-line event selection, for the Higgs signal and for the SUSY and SM backgrounds. The efficiency of each cut with respect to the previous one is indicated in brackets. The cross-sections are given in fb and efficiencies are in percent. The global signal acceptances with respect to the production cross-section times branching ratio are 6.3%, 5.1% and 2.5% respectively for point A, B and C, whereas the acceptances for the SUSY backgrounds are 1.5×10^{-6}, 3.6×10^{-6} and 2.6×10^{-6} respectively, relative to the total SUSY production cross-section.

	Point A fb (%)	Point B fb (%)	Point C fb (%)
σ	13.7 10^3	2.73 10^3	6.3 10^3
$\sigma \times B.R.$	108 (0.8)	54.5 (2)	65.9 (1.1)
$\sigma \times B.R. \times \epsilon$	33.4 (31)	18 (33)	13.1 (20)
Level-1/HLT	32 (97)	17.6 (98)	10.3 (79)
$e^+e^-\mu^+\mu^-$ reconstruction	25.5 (80)	14.2 (81)	7.4 (72)
Jet veto	8.2 (32)	3.5 (25)	1.9 (26)
Isolation cut	7.8 (97)	3.4 (96)	1.8 (94)
$\not{E}_T$& p_T^{llll} cuts	7.4 (94)	3.0 (89)	1.7 (95)
Z veto & min. dilepton mass	6.8 (92)	2.8 (95)	1.3 (75)
Dilepton edges cuts	6.8 (100)	2.8 (100)	1.3 (100)
Higgs mass window cut	6.8 (100)	2.8 (100)	1.3 (99)

Table 5.6: Production cross-sections and cross-sections after each step of the online and off-line selection for the Higgs signal and for the three benchmark points. Efficiencies with respect to the previous cut are quoted in brackets.

Figure 5.19 presents the reconstructed 4-leptons invariant mass distributions for each of the three benchmarks points after the selection. Results are given for an integrated luminosity of 30 fb^{-1}. Each background contribution is added to the previous one (histograms) and finally to the Higgs signal (points).
The A/H could be easily discovered at the points A and B with such an integrated luminosity, while for the point C the signal visibility is lower due to the higher SUSY background in this case.
To quantify the probability to observe a signal in a future experiment different significance estimators can be used. They are usually classified as event counting and likelihood methods. For a given luminosity $\mathcal{L}$ the expected number of events is $n_S = \sigma_S \mathcal{L}$ for the signal and $n_B = \sigma_B \mathcal{L}$ for the background. Therefore $\langle n \rangle = n_B + n_B$ events are expected in total on average in presence of signal.
Event counting methods compare n_S and n_B to define the significance in term of the number of standard deviations an observed signal is above the expected background fluctuations [87]. The most commonly used estimators are

$$S_1 = n_S/\sqrt{n_B} \tag{5.9}$$

$$S_{12} = 2(\sqrt{n_S + n_B} - \sqrt{n_B}) \tag{5.10}$$

$$S_2 = n_B/\sqrt{n_S + n_B} \tag{5.11}$$

Likelihood methods take also the shape of the distributions into account. They consider the ratio of the null hypothesis H_0 (background only, $\langle n \rangle = n_B$) to an alternative hypothesis H_1 (the signal is present,$\langle n \rangle = n_B + n_S$). The significance

	SUSY Back A fb (%)	SUSY Back B fb (%)	SUSY Back C fb (%)	$t\bar{t}$ fb (%)	$Zb\bar{b}$ fb (%)	$ZZ^{(*)}/\gamma^*$ fb (%)
σ	216 10^3	116 10^3	430 10^3	840 10^3	278 10^3	29 10^3
$\sigma \times B.R.$	-	-	-	53.9 10^3 (63)	18.6 10^3 (6.7)	368 (1.27)
$\sigma \times B.R. \times \epsilon$	517 (0.2)	586 (0.5)	2020 (0.47)	682 (1.3)	258 (1.4)	33.7 (9.2)
Level-1/HLT	467 (90)	556 (95)	1824 (90)	600 (88)	221 (86)	31.2 (98)
$e^+e^-\mu^+\mu^-$ reconstruction	335 (72)	430 (77)	1346 (74)	274 (46)	132 (60)	23.1 (74)
Jet veto	2.0 (0.6)	3.0 (0.7)	7.6 (0.6)	6.6 (2.4)	6.9 (5.2)	10 (44)
Isolation cut	1.3 (62)	2.2 (72)	3.7 (48)	0.59 (9)	3.4 (50)	9.9 (98)
$\not{E}_T$& p_T^{4l} cuts	0.8 (63)	1.2 (54)	2.3 (62)	0.37 (64)	3.1 (92)	9.5 (95)
Z veto & min. dilepton mass	0.6 (76)	0.98 (83)	1.7 (73)	0.27 (71)	0.28 (9)	0.71 (7.5)
Dilepton edges cuts	0.40 (66)	0.74 (76)	1.36 (73)	0.12 (47)	0.17 (59)	0.37 (53)
Higgs mass window cut	0.34 (85)	0.43 (57)	1.1 (80)	0.11 (86)	0.17 (100)	0.36 (96)

Table 5.7: Production cross-sections and cross-sections after each step of the online and off-line selection for the various backgrounds. Efficiencies with respect to the previous cut are quoted in brackets.

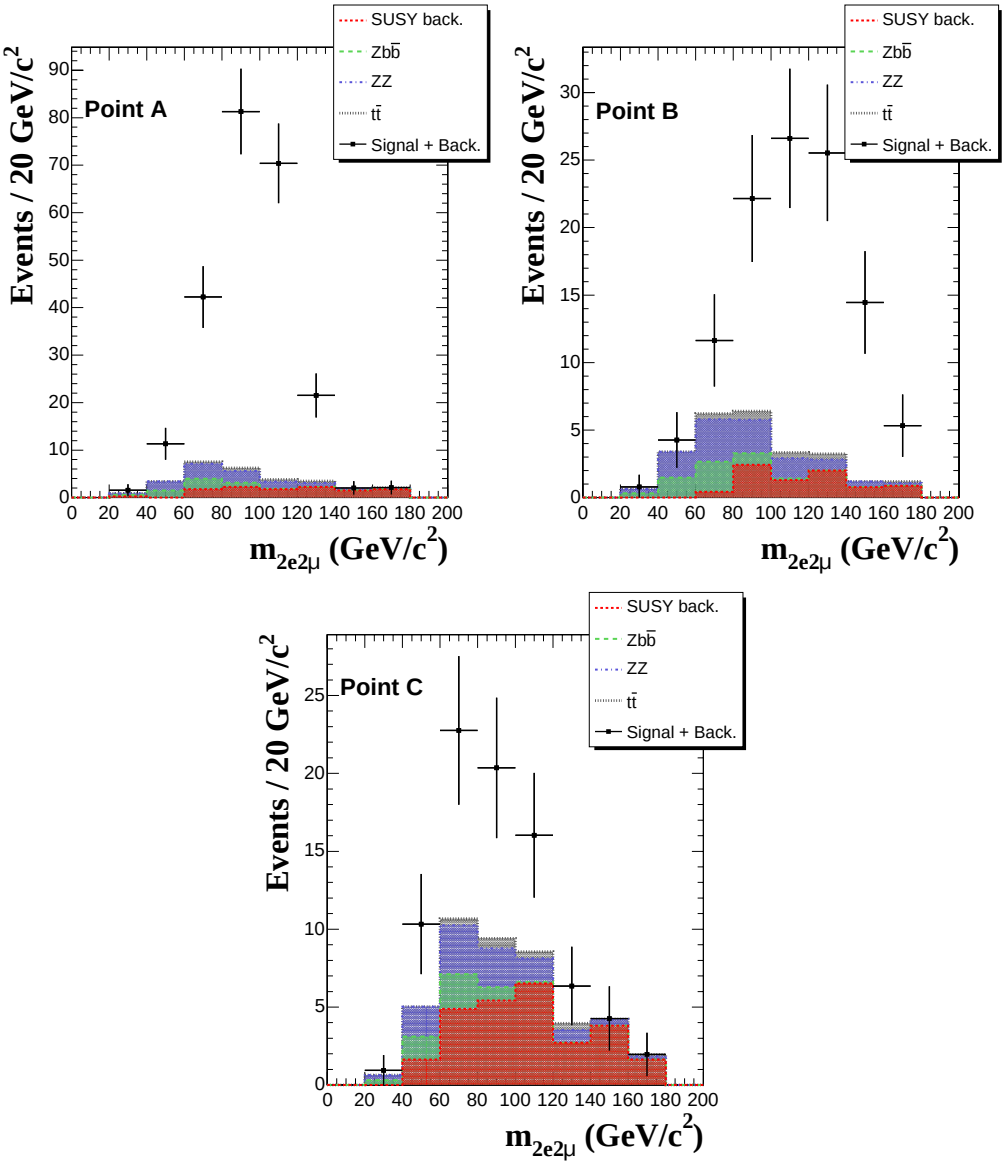

Figure 5.19: Four lepton invariant mass distributions for the three benchmark points: (top, left) point A, (top, right) point B and (bottom) point C. Each background contribution is added to the previous one (histograms) and finally to the Higgs signal (points). Results are given for an integrated luminosity of 30 fb^{-1}.

is defined as

$$S_L \;=\; \sqrt{2\,\ln Q} \;=\; \sqrt{2\,(\ln L_1 - \ln L_0)}$$

where L_0 and L_1 are the likelihood values in the null hypothesis and in the alternative one. Assuming Poisson statistics and considering

$$P_0(n; n_B) \;=\; \frac{1}{n!}\, n_B^n\, e^{-n_B}$$

$$P_1(n; n_B + n_S) \;=\; \frac{1}{n!}\, (n_B + n_S)^n\, e^{-(n_B+n_S)}$$

the previous expression can be expressed as

$$S_{cL} \;=\; \sqrt{2\,\ln Q} \quad \text{with} \quad Q \;=\; \left(1 + \frac{n_S}{n_B}\right)^{n_B+n_S}\; e^{-n_S}$$

The S_{cL} significance estimator is used here to quantify the signal sensitivity. Table 5.8 gives the significance S_{cL} for the points A,B and C, counting events in the range 20 GeV/c^2 $< m_{ee\mu\mu} <$ 180 GeV/c^2, after all selection cuts and for an integrated luminosity of 30 fb^{-1}.

	Point A	Point B	Point C
S_{cL}	23.6	11.5	4.8

Table 5.8: Statistical significance for the three benchmark points counting events in the range $20 < m_{ee\mu\mu} < 180$ GeV/c^2, after all selection cuts and for an integrated luminosity of 30 fb^{-1}.

5.6 CMS discovery potential

A calculation of the CMS 5σ discovery reach is performed, extrapolating the results obtained for the three benchmark points. To determine the reach in the $(m_0, m_{1/2})$ parameter plane, the calculation of the signal $\sigma \times B.R.$ at each point of the $(m_0, m_{1/2})$ plane is used (see Figure 5.5). The signal selection efficiency is parametrized as a function of the pre-selection efficiency determined for each point of the plane, using the fact that this pre-selection efficiency is directly related to the leptons p_T spectra and approximating the signal selection efficiency to a pure p_T dependence effect. The number of SUSY background events is evaluated using for each point in the plane the total SUSY production cross-section and taking as the background acceptance the highest value among the ones obtained for the three representative points after the selection (conservative approach). For the SM backgrounds, the final cross-sections after all selection cuts as given in Table 5.7 are used. Finally, the significance for an integrated luminosity of 30 fb^{-1} is computed taking into account an estimation of the systematic uncertainty on the number of background events.

The jet energy scale is expected be calibrated in CMS using photon plus jet events and an integrated luminosity of 10 fb^{-1} [88]. Accordingly, a variation of the jet energy of 10% to 3% depending on the jet p_T is applied. Its effect on the background estimation is found to be of the order of 6%. The missing transverse energy is expected to be well measured and understood from single Z and single W production. The $\not\!\!E_T$ measurement can be controlled, e.g. via single Z production by artificially removing one lepton. Uncertainties of 4.5% for the $\not\!\!E_T$ resolution and of 2% for the $\not\!\!E_T$ scale are deduced from W mass measurement studies [89] and are applied. The resulting uncertainty on the background estimation is found to be of the order of 4%. Finally, a 5% uncertainty is taken as the systematic uncertainty on the background estimation from the luminosity measurement.
Figure 5.20 shows the extrapolated 5σ-discovery contours in the $(m_0, m_{1/2})$ plane, for an integrated luminosity of 30 fb^{-1}. The values of the other mSUGRA parameters are: $A_0 = 0$, sign$(\mu) = +$ and tan$\beta = 5, 10$.
The complex structure of the discovery region is mainly determined by the cross-section times branching ratio of $A/H \rightarrow \chi_2^0\chi_2^0 \rightarrow 4l + \not\!\!E_T$. The A/H could be discovered through their decays to neutralino pairs in the region 150 GeV/c^2 $< m_{1/2} <$ 250 and 40 GeV/c^2 $< m_0 <$ 130 GeV/c^2 for tan$\beta = 5$ and in the region 140 GeV/c^2 $< m_{1/2} <$ 240 GeV/c^2 and $m_0 <$ 110 GeV/c^2 for tan$\beta = 10$. This corresponds to heavy neutral Higgs bosons masses in the range 250 GeV/$c^2 \lesssim m_{\mathrm{A,H}} \lesssim$ 400 GeV/c^2, as can be seen from the iso-mass curves also indicated on the Figure 5.20.

5.7 Summary

A prospective study for the observability in CMS of heavy neutral Higgs bosons decaying into two next-to-lightest neutralinos and then to four leptons plus missing transverse energy has been performed. Sizable regions of the parameter space where the event rate is high have been identified. The main backgrounds can be sufficiently suppressed using appropriate selection criteria. In particular, the important SUSY background which arises in the mSUGRA framework from the existence of light sleptons can be efficiently reduced using a jet veto, mass independent missing transverse energy and 4-lepton transverse momentum cuts, and exploiting also the correlation between these two kinematical variables in signal events. In the 2e2μ decay channel, the characteristic double kinematical edge in the dilepton invariant mass distributions can be further used to suppress the backgrounds. A starting value is used which could be further refined in a scenario where SUSY would have been already discovered through the observa-

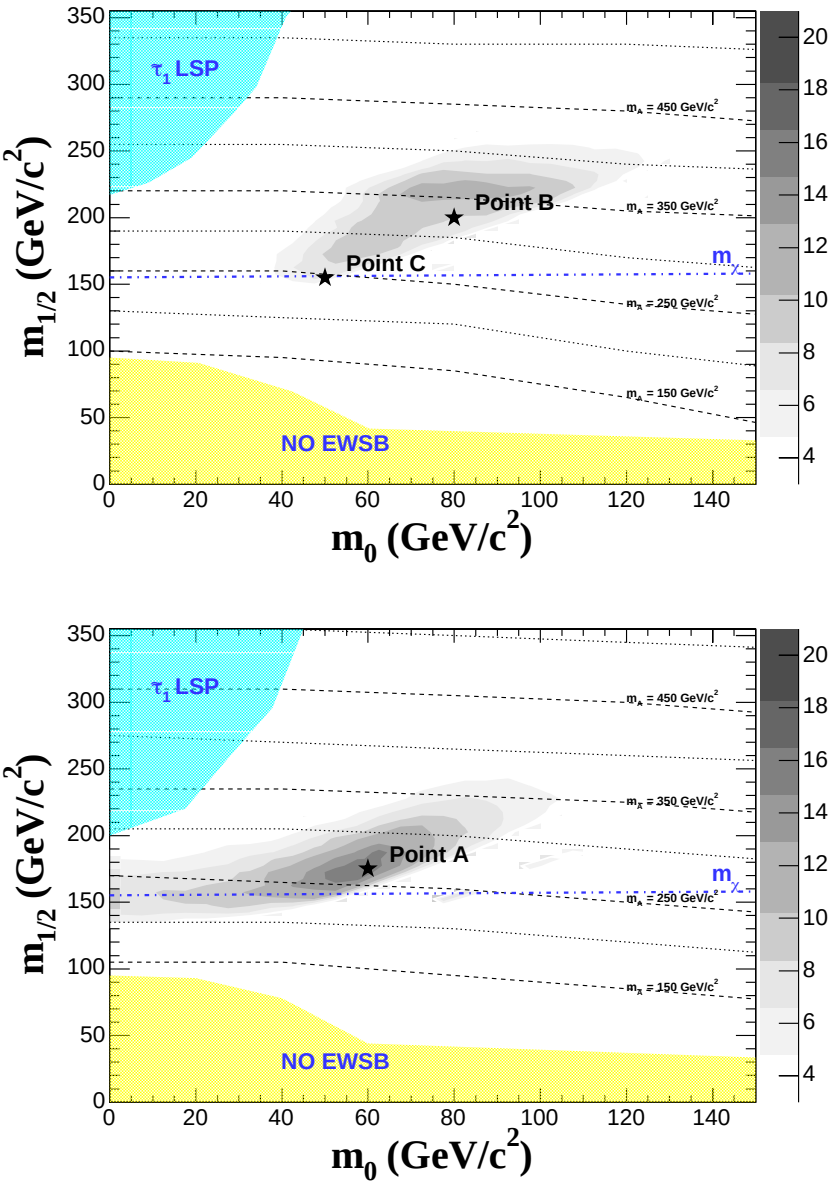

Figure 5.20: 5σ-discovery contours for $A/H \rightarrow \chi_2^0\chi_2^0 \rightarrow 4l + \not{E}_T$ in the $(m_0, m_{1/2})$ plane for fixed $A_0 = 0$, sign$(\mu) = +$ and for (top) tan$\beta = 5$ and (bottom) tan$\beta = 10$. Iso-mass curves for the CP-even Higgs boson are indicated (dashed and dotted lines). The results are shown for an integrated luminosity of 30 fb^{-1}.

tion of SUSY particles. It is shown that, depending on the selected point in the SUSY parameter space, the A and H Higgs bosons could be discovered in the

2e2μ decay channel in the mass region 250 GeV/$c^2 \lesssim m_{\mathrm{A,H}} \lesssim$ 400 GeV/c^2 for an integrated luminosity of 30 fb^{-1} .

Conclusions

In this thesis a prospective study for the observability of heavy neutral Higgs bosons decaying into supersymmetric particles at the Large Hadron Collider with the CMS detector has been presented. The analysis focuses on the decay of the heavy neutral Higgs bosons into a pair of next-to-lightest neutralinos χ_2^0, followed by the cascade down to the lightest neutralino, $\chi_2^0 \rightarrow l^+l^-\chi_1^0$. The final state is characterized by the presence of four isolated leptons and missing transverse energy. The Higgs bosons decay into sparticles opens possibilities to explore regions of the parameter space otherwise inaccessible via SM-like decays into ordinary particles This is the case in particular in the low and intermediate tanβ region of the MSSM parameter space.

The final topology of the physics channel includes electrons, and for this reason a central role is played by the CMS electromagnetic calorimeter, with the aim to reach an excellent intrinsic energy resolution. A direct contribution to the constant term of the energy resolution is given by the intercalibration of the calorimeter crystals. The intercalibration coefficients obtained with laboratory measurements of the crystal light yield and the commissioning of further supermodules with the first cosmic rays data recorded have been performed. Moreover, since the response of the crystals is affected by the irradiation, the evolution of the crystals response when irradiated with electrons has been studied. The accuracy of the laser monitoring system, in order to followed up the crystals transparency during irradiation, has been demonstrated. The proposed correction procedure allows to stabilize the response of each crystal with an accuracy better than 0.4%.

The analysis this physics channel requires low p_T isolated electrons to be measured and identified in challenging kinematics and background conditions. For this reason based on the full sequence of steps for electron reconstruction a new strategy for the selection, isolation and identification of primary electrons exploiting different electron measurement patterns has been studied. Possible discriminating variables for the selection have been presented. Lepton track isolation requirements have been introduced as a complementary step to the

first data reduction to suppress possible background sources involving "fake" electrons. New observables sensitive to the amount of bremsstrahlung photons emitted in the tracker volume and their possible conversion in the tracker material have been introduced. It has been shown that different electron identification cut strategies and combination of electron identification observables are needed for the various "classes" of electron patterns. Based on a simple cut approach, the electron identification performance has been evaluated for electrons in the p_T range from 5 to 50 GeV/c against "fake" electrons coming from QCD di-jet background. It has been shown that an absolute overall jet background fake rate efficiency at the level of 6×10^{-4} can be obtained while keeping efficiency on electrons at the level of 90%.

Finally, the last part of the presented work is devoted to the detailed study of the physics subject. Sizable regions of the SUSY parameter space where the event rate is high have been identified. It has been shown that the main backgrounds can be sufficiently suppressed using appropriate selection criteria. In particular, the important SUSY background which arises from the existence of light sleptons can be efficiently reduced using a jet veto, mass independent missing transverse energy and 4-lepton transverse momentum cuts, and exploiting also the correlation between these two kinematical variables in signal events. In the 2e2μ decay channel, the characteristic double kinematical edge in the dilepton invariant mass distributions can be further used to suppress the backgrounds. A starting value is used which could be further refined in a scenario where SUSY would have been already discovered through the observation of SUSY particles. It is shown that, depending on the selected point in the SUSY parameter space, the A and H Higgs bosons could be discovered in the 2e2μ decay channel in the mass region 250 GeV/$c^2 \lesssim m_{\mathrm{A,H}} \lesssim$ 400 GeV/c^2 with an integrated luminosity of 30 fb^{-1} .

Bibliography

[1] F. Halzen and A. Martin, *"Quarks and Leptons: An Introductory Course in Modern Particle Physics,"* John Wiley and Sons, New York, 1984;
C. Quigg, *"Gauge Theories of the Strong, Weak, and Electromagnetic Interactions,"* The Benjamin/Cummings Publishing Company, London, 1983;
G. Kane, *"Modern Elementary Particle Physics,"* Addison-Wesley Publishing Company, Reading, MA, 1993.

[2] M.Martinez *et al.*, *"Precision Tests of the Electroweak Interactions at the Z Pole"*, CERN-EP/98-27.

[3] U . Amaldi, W. de Boer and H. Fuerstenau, Phys. Lett. B **260** (1991) 447.

[4] L. Maiani, *Proceedings of the 1979 Gif-sur-Yvette summer school on particle physics, 1*;
E . Witten, Phys. Lett. B **105** (1981) 267.

[5] E . Kolb and M. Turner, *"The Early Universe"*. (1989).

[6] S. R. Coleman and J. Mandula, Phys. Rev. **159** (1967) 1251.

[7] D. Boulatov and V. Kazakov, Int. J. Mod. Phys. A **8** (1993) 809.

[8] J. Iliopoulos, *Prepared for European School of High-Energy Physics (ESHEP 2002), Pylos, Greece, 25 Aug - 7 Sep 2002.*

[9] D. N. Spergel *et al.*, arXiv:astro-ph/0603449.

[10] J. Ellis *et al.*, Nucl. Phys. B **238** (1984) 453; H. Goldberg, Phys. Rev. Letter **50** (1983) 1419.

[11] L. Brink, S. Deser, B. Zumino, P. Di Vecchia and P. S. Howe, Phys. Lett. B **64** (1976) 435.

[12] R. Farrar ana P.Fayet, Phys. Lett. B **76** (1978) 575.

[13] J. R. Ellis, T. Falk. G. Ganis, K. A. Olive and M. Schmitt Phys. Lett. D **58** (1999) 95.

[14] J. R. Ellis and S. Rudaz, Phys. Lett. B **128** (1983) 248.

[15] L. Girardello and M. T. Grisaru, Nucl. Phys. B **194** (1982) 65.

[16] F. Englert and R. Brout, Phys. Rev. Lett. **13** (1964) 321;
P. W. Higgs, Phys. Lett. **12** (1964) 132;
G. S. Guralnik, C. R. Hagen and T. W. B. Kibble, Phys. Rev. Lett. **13** (1964) 585.

[17] J.F. Gunion, H.E. Haber, G. Kane and S. Dawson, *"The Higgs Hunters Guide"* Perseus Publishing, Cambridge, MA (1990).

[18] H.E. Haber and Y. Nir, Phys. Lett. B **306** (1993) 327.

[19] **LEPSUSYWG, ALEPH, DELPHI, L3** and **OPAL** Collab., Preliminary results from the combination of LEP data, prepared by the LEP SUSY Working Group. LEPSUSYWG/02-01.1, 02-02.1, 02-04.1, 02-05.1, 02-06.2, 02-07.1, 02-08.1, 02-09.2, 02-10.1, 01-03.1, 01-07.1 See also `http://www.cern.ch/lepsusy/`.

[20] **D**$\emptyset$: Phys. Rev. Lett. **83**, (1999) 4937 and Phys. Rev. Lett. **75**, (1995) 618; **CDF**: Phys. Lett. D **56**, (1997) 1357 and Phys. Rev. Lett. **76**, (1996) 2006.

[21] **CDF**: Phys. Rev. Lett. **88**, (2002) 041801.

[22] The LEP Working Group for Higgs searches, **ALEPH, DELPHI, L3** and **OPAL** Coll., Phys. Lett. B **365** (2003) 61.

[23] W.N. Yao (for the **CDF** and **D**$\emptyset$ Coll.), arXiv:hep-ex/0411053.

[24] D. Denegri *et al.*, CMS NOTE 2001/032.

[25] D . Benedetti *et al.*, CMS NOTE 2006/119.

[26] R. Kinnunen, CMS NOTE 2006/100.

[27] S. Abdullin *et al.*, CMS NOTE 2003/033.

[28] S. Abdullin D. Denegri and F. Moortgat, CMS NOTE 2001/042.

[29] H. Baer and X. Tata, Phys. Rev. D **47** (1993) 2739.

[30] T. L. S. Group, "The Large Hadron Collider Conceptual Design", CERN-AC-95-05 (1995) arXiv:hep-ph/0601012.

[31] T.S. Virdee, Phys. Rept. **403** (2004) 401.

[32] ATLAS Collaboration, "ATLAS Technical Proposal for a General-Purpose pp Experiment at the Large Hadron Collider at CERN", CERN/LHCC 94-43 (1994).

[33] CMS Collaboration, The Compact Muon Solenoid Technical Proposal, CERN/LHCC **94-38** (1994).

[34] ALICE Collaboration, "ALICE Technical Proposal", CERN/LHCC **2001-021** (2001).

[35] LHCb Collaboration, "LHCb Technical Proposal", CERN/LHCC **98-004** (1998).

[36] CMS Collaboration, "The Tracker System Project Technical Design Report", CERN/LHCC **98-06** (1998).
CMS Collaboration, "Addendum to the CMS Tracker TDR", CERN/LHCC **2000-016** (2000).

[37] CMS Collaboration, "The Electromagnetic Calorimeter Technical Design Report", CERN/LHCC **97-033** (1997).

[38] CMS Collaboration, "The Hadron Calorimeter Technical Design Report", CERN/LHCC **97-031** (1997).

[39] CMS Collaboration, "The Muon Project Technical Design Report", CERN/LHCC **97-32** (1997).

[40] CMS Collaboration, "The Magnet Project Technical Design Report", CERN/LHCC **97-010** (1997).

[41] CMS Collaboration, "The Trigger and Data Acquisition Project, Volume I: The Level-1 Trigger Technical Design Report", CERN/LHCC **00-38** (2000).

[42] CMS Collaboration, "The Trigger and Data Acquisition Project, Volume II: Data Acquisition and High Level Trigger Technical Design Report", CERN/LHCC **02-26** (2002).

[43] A. A. Annenkov, M. V. Korzhik, and P. Lecoq, Nucl. Instrum. Meth. A **490** (2002) 30.

[44] D. Graham and C. Seez, CMS NOTE 1996-002..

[45] R. Y. Zhu, Nucl. Instrum. Meth. A **413** (1998) 297.

[46] M. Raymond *et al.*, "The MGPA Electromagnetic Calorimeter Readout Chip for CMS", *Proceedings of the 9th Workshop on Electronics for the LHC Experiments, 2003*, CERN-LHCC **2003-055**.

[47] G. Minderico *et al.*, "A CMOS low power, quad channel, 12 bit, 40 Ms/s pipelined ADC for application in particle physics calorimetry", *Proceedings of the 9th Workshop on Electronics for the LHC Experiments, 2003*, CERN-LHCC **2003-055**.

[48] P.Baillon *et al.*, CMS Conference Report 2004/030, `http://cmsdoc.cern.ch/documents/04/cr04_030.pdf`

[49] L. Zhang *et al.*, IEEE Trans. Nucl. Sci. **52** (2005).

[50] R. Brunelière and A. Zabi, CMS NOTE 2006-037.

[51] F. Cavallari *et al.*, CMS Rapid Note 2004/002, `http://cmsdoc.cern.ch/documents/04/rn04_002.pdf`.

[52] G. Franzoni *et al.*, CMS Internal Note 2004/046, `https://cmsdoc.cern.ch/documents/04/in/in04_046.pdf`

[53] E. Auffray *et al.*, Nucl. Instrum. Meth. A **456** (2001) 325.

[54] E. Auffray *et al.* (CMS Collaboration), Nucl. Instrum. Meth. A **523** (2004) 355.

[55] L. M. Barone *et al.*, CMS Rapid Note 2004/003, `http://cmsdoc.cern.ch/documents/04/rn04_003.pdf`.

[56] W. Bertl *et al.*, Eur. Phys. J. C **41S2** (2005) 11.

[57] S. Agostinelli *et al.* [GEANT4 Collaboration], Nucl. Instrum. Meth. A **506** (2003) 250.

[58] Th. Frisson and Ph. Miné, CMS Internal Note 2004/001 , `https://cmsdoc.cern.ch/documents/04/in/in04_001.pdf`

[59] L. Bonecchi, Ph.D Thesis, Universitá di Firenze (in Italian).

[60] P.Bonamy *et al.*, CMS NOTE 1998-013.

[61] C. Seez *et al.* CMS Internal Note 1998/026 , `https://cmsdoc.cern.ch/documents/98/in/in98_026.pdf`

[62] A. Van Lysebetten, P. Verrecchia, CMS Rapid Note 2004/001, `http://cmsdoc.cern.ch/documents/04/rn04_001.pdf`.

[63] A. Ghezzi *et al.* CMS NOTE 2006-038.

[64] `FAMOS`, "Fast Monte-Carlo Simulation", version 1.4.0. (December 2005).

[65] `ORCA`, "Object-oriented Reconstruction for CMS Analysis", version 8.7.3. (February 2005).

[66] CMS Collaboration, "CMS Physics Technical Design Report, Volume 1", CERN-LHCC **06-001** (2006).

[67] R. Frühwirth, Comput. Phys. Commun., **100** (1997) 1-16.

[68] W. Adam, R. Frühwirth, A. Strandlie, and T. Todorov, CMS Note 2005/001.

[69] E. Meschi, T. Monteiro, C. Seez, and P. Vikas, CMS NOTE 2001/034.

[70] S. Baffioni *et al.*, CMS NOTE 2006/115.

[71] P. Meridiani, "Optimization of the discovery potential of the Higgs Boson in the decay channel $H \to ZZ^{(*)} \to 4e^{\pm}$ with the CMS detector", Doctor degree thesis, University of Roma-1 (September 2004) 199pp.

[72] C. Charlot, R. Salerno and Y. Sirois, CMS NOTE 2006/126.

[73] M. Spira, arXiv:hep-ph/9510347.

[74] M. Spira, `http://mspira.home.cern.ch/mspira/proglist.html`.

[75] F. E. Paige, S. D. Protopopescu, H. Baer and X. Tata, arXiv:hep-ph/0312045.

[76] C. Zecher, T. Matsuura and J. J. van der Bij, Z. Phys. **64** (1994) 219.

[77] S. R. Slabospitsky and L. Sonnenschein, Comput. Phys. Commun. **148** (2002) 87.

[78] J. M. Campbell and R. K. Ellis, `http://mcfm.fnal.gov`.

[79] M. Beneke *et al.*, CERN preprint CERN-TH-2000-100.

[80] CMS Collaboration, CMS Physics Technical Design Report Volume II, CERN/LHCC **06-021** (2006).

[81] J. Campell *et al.*, arXiv:hep-ph/0510362.

[82] D. Giordano, *Presentation at the CMS Higgs group meeting.*

[83] T. Sjostrand *et al.*, Comput. Phys. Commun. **135** (2001) 238.

[84] E. Boos et al., CompHEP Collaboration, Nucl. Instrum. Meth. A **534** (2004) 250.

[85] W. Beenakker, R. Hoepker and M. Spira, arXiv:hep-ph/9611232.

[86] `http://cmsdoc.cern.ch/famos/`.

[87] V. Bartsch and G. Quast, CMS NOTE 2005/004.

[88] J. Rohlf and C. Tully, CMS NOTE to be submitted.

[89] V. Buge *et al.*, CMS NOTE 2006/061.

Acknowledgements

Working in the field of high energy physics involves extensive international collaboration, adding and important social and cultural dimension to the scientific research. Therefore I am grateful to many people for their help and support during the past years.
The work of this thesis has been carried out in the Da Vinci PhD collaboration program between the Univesità di Milano-Bicocca and the Ècole Polytechnique de Palaiseau
First of all, I wish to thank Claude Charlot and Marco Paganoni, for accepting to be my supervisors and always support me. Thank you for your infinite patience, your continuos help, suggestions and encoragements. I'm sure that all the results containing in this thesis are also yours. A special thank to Yves Sirois for all the useful discussions which really made me learn a lot.
Thank you Antonino Pullia, you are a reference figure in the Milano group. I would like to thank Alberto De Min, Stefano Ragazzi and Tomasso Tabarelli de Fatis for a lot of fruitful discussions. Thank you to all my young Italian colleagues: Alessio, Chiara, Federico, Giovanni and Pietro. Thanks for your friendship, knowledge and company.
Thank you Ludwik Dobrzynski and Philippe Busson, from my first arrive at Ècole Polytechnique they have helped me to feel at home. Thank you to the others members of the LLR group and the collaborators: Evelyne, Florian, Stephane, Stephanie, Gérard, Igor, Ivica, Maurice, Nicola, Pascal, Philippe and Ursula. Thanks for your friendship and weekly dinners during my stay at Ècole Polytechnique.
Thanks to everyone else in the CMS collaboration that I didn't mention here by name. This dissertation would not be possible without your years of hard work.
I'm grateful to my referees Abdelhak Djouadi and Ugo Gasparini for their careful reading of the manuscript and very interesting suggestions.
Thank you Elwood, you have been a perfect mate during the last years, you have never protested in spite of I have done violence to your keyboard so many times.
I wish to thank my Asics Blue, you have supported more the 500 kilometers

during the writing of this thesis without any problem.
Last but certainly not least, thanks to who has supported me for a lifetime of unconditional love. Knowing I can always count on it has helped me immeasurably in my life.